On the theory and numerical simulation of cohesive crack propagation with application to fiber-reinforced composites

by

Krishna Siva Shankar Rudraraju

A dissertation submitted in partial fulfillment
of the requirements for the degree of
Doctor of Philosophy
(Mechanical Engineering and Scientific Computing)
in The University of Michigan
2011

Doctoral Committee:

Associate Professor Krishnakumar Garikipati, Co-Chair
Professor Anthony M. Waas, Co-Chair
Associate Professor Divakar Viswanath
Assistant Professor Vikram Gavini
Brett A. Bednarcyk, NASA Glenn Research Center

TABLE OF CONTENTS

LIST OF FIGURES v

LIST OF TABLES vii

ABSTRACT viii

CHAPTER

I. Introduction 1

1.1 Motivation 1
1.2 Analytical Challenges 3
1.3 Numerical Challenges 4
1.4 Adopted Approach and Goals 5
1.5 Outline 7

II. Mechanics of Cohesive Crack Propagation 8

2.1 Crack Propagation in Cohesive Materials 9
    2.1.1 Classical Fracture Mechanics 9
    2.1.2 Small Process Zone and Barenblatt Cohesive Model 15
2.2 Crack Propagation in Bridging Materials 18
    2.2.1 Large Process Zone and Traction-Separation Models 19
    2.2.2 Cohesive Zone Model and Other Numerical Methods 21
2.3 Crack Propagation in Fiber Reinforced Composites 23
    2.3.1 Micromechanics 25
2.4 Closing Remarks 27

III. Multiscale Framework and Variational Formulation 29

3.1 Background and Variational Multiscale Concept 29
    3.1.1 Grid Scale model: Large-scale and Small-scale . . . 30
    3.1.2 Subgrid Scale model: Coarse-scale and Fine-scale . . 33
3.2 Cracks as Subgrid Scales: Motivation and Challenges 36

3.3 Multiscale Formulation of Discontinuous Displacement 38
3.4 Fine-Scale Field and Micromechanics Embedding 41
3.5 Closing Remarks 42

IV. Finite Element Implementation 43

4.1 Mesh Sensitivity of Standard Galerkin Basis 44
  4.1.1 Pathological Mesh Dependence of Strain Localization in Softening Materials 44
  4.1.2 Discretization Sensitivity of Crack Paths 47
4.2 Multiscale Element Construction 48
  4.2.1 Shape Functions 48
  4.2.2 Numerical Quadrature 52
4.3 Finite Dimensional Weak Forms and Discretized Equations . 53
4.4 Incremental Solution Procedure 57
4.5 Closing Remarks 58

V. Numerical Simulations 60

5.1 Mesh Objectivity Demonstration 61
  5.1.1 Straight Crack Propagation 61
  5.1.2 Curved Crack Propagation 62
5.2 Mixed Mode Crack Propagation 65
5.3 Interacting and Multiple Cracks 70
5.4 Closing Remarks 73

VI. Experimental Validation and Analysis 74

6.1 Experimental Setup 74
  6.1.1 Characterization of Cohesive Properties 75
  6.1.2 Crack Propagation Case Studies 77
6.2 Numerical Simulations and Comparison With Experiments . . 78
6.3 Closing Remarks 80

VII. Conclusions and Future work 84

APPENDIX 86
A.1 Introduction 87
A.2 Analytical Formulation 89
  A.2.1 Interface Crack and Frictional Contact 89
  A.2.2 Interface Crack Propagation 91
  A.2.3 Fiber Pullout 94
  A.2.4 Summary 95
A.3 Numerical Framework and Simulations 96

BIBLIOGRAPHY 101

LIST OF FIGURES

Figure

2.1 Crack in an infinite plate of uniform thickness . . . 10
2.2 Crack closure analysis to determine the energy release rate . . . 13
2.3 Crack opening profile due to the influence of cohesive forces in the crack wake . . . 16
2.4 Schematic of a possible cohesive traction function . . . 17
2.5 Schematic of a various toughening mechanisms . . . 18
2.6 Schematics of possible bridging traction-separation and cohesive traction-separation relations . . . 19
2.7 Schematic of possible mixed cohesive-bridging traction-separation relations . . . 20
2.8 Complexity and diffused damage observed in fiber composites . . . 24
2.9 Various modes of micromechanical damage evolution observed during the process of through-the-thickness crack propagation . . . 27
3.1 Schematic of the grid scale model . . . 31
3.2 Schematic of the subgrid scale model . . . 34
3.3 Representation of crack as a displacement discontinuity . . . 37
3.4 Schematic of the microstructural domain and the crack surface . . . 40
4.1 Schematic of displacement field in a domain containing strong and weak discontinuities . . . 44
4.2 Performance of standard Galerkin basis . . . 45
4.3 Comparison of representative crack paths observed using traditional crack propagation schemes . . . 47
4.4 Schematic of the crack path and fine-scale domain . . . 48
4.5 Construction of the discontinuous multiscale shape function in 1D . . . 49
4.6 Construction of the multiscale shape function in 2D . . . 50
4.7 Construction of the multiscale shape function in 2D . . . 51
4.8 Elemenal values of the displacement discontinuity . . . 53
4.9 Quadrature rules for coarse-scale and fine-scale problems in triangle elements . . . 54
4.10 Comparison of multiscale and partition of unity based interpolation schemes . . . 58
5.1 Mesh objectivity demonstration for straight crack propagation . . . 63

5.2 Mesh objectivity demonstration for curved crack propagation 64
5.3 Crack propagation in symmetrically loaded CTS specimen 67
5.4 Crack propagation in an eccentrically loaded SETB specimen 68
5.5 Curved crack propagation in rectangular specimen 69
5.6 Curved crack propagation in rectangular specimen with restricted crack growth directions 69
5.7 Double crack propagation in DENT specimen 71
5.8 Crack propagation in the presence of a hard inclusion 72
6.1 Specimen cross section 75
6.2 Linear traction-separation law 76
6.3 Characterization of cohesive properties 76
6.4 Single edge notch three point bend specimen configurations 78
6.5 Eccentric compact tension specimen configurations 79
6.6 Load-Displacement response of symmetrically loaded SETB specimens 81
6.7 Load-Displacement response of eccentrically loaded SETB specimens 82
6.8 Load-Displacement response of eccentric CTS specimens 82
6.9 Comparison of experimental and numerical crack paths observed in eccentric CTS specimens 83
A.1 Bridging zone evolution 89
A.2 Schematic showing the evolution of debonding crack 92

LIST OF TABLES

Table

6.1 Lamina and laminate properties of carbon fiber/epoxy $[-45/0/+45/90]_{6s}$ laminated fiber reinforced composite. 75
A.1 List of symbols for fiber-pullout micromechanics 90
A.2 Material properties for fiber-pullout micromechanics 95

ABSTRACT

On the theory and numerical simulation of cohesive crack propagation with application to fiber-reinforced composites

by

Krishna Siva Shankar Rudraraju

Co-Chair's: Krishnakumar Garikipati and Anthony M. Waas

The phenomenon of crack propagation is among the predominant modes of failure in many natural and engineering structures, often leading to severe loss of structural integrity and catastrophic failure. Thus, the ability to understand and a priori simulate the evolution of this failure mode has been one of the corner stones of applied mechanics and structural engineering, and is broadly referred to as fracture mechanics. The work presented here focuses on extending this understanding, in the context of through-the-thickness crack propagation in cohesive materials, through the development of a continuum level multiscale numerical framework, which represents cracks as displacement discontinuities across a surface of zero measure. The formal treatment significantly derives from earlier work on numerical simulation of strong discontinuities and the variational multiscale method. The resulting computational framework is demonstrated through benchmark problems and validated by comparison with experimental observations of failure in fiber-reinforced composites.

CHAPTER I

Introduction

This chapter provides an introduction to the phenomenon of cohesive crack propagation and its numerical simulation. Beginning with a motivation for studying crack propagation in materials with complex microstructures in Section 1.1, the relevant analytical and numerical challenges are discussed in Section 1.2 and Section 1.3, respectively. Then the approach adopted and the specific goals are laid out in Section 1.4 and an outline of the remainder of the dissertation is provided in Section 1.5.

1.1 Motivation

On application of external forces, the primary mode of response of a solid is the stretching of inter-atomic bonds, which is "globally" manifested as material deformation. Understanding the resulting continuum scale kinematics and constitutive behavior of this deformation response, within the limit of recoverability (elastic limit), are addressed in detail by the Theory of Elasticity [*Timoshenko* (1934); *Truesdell and Noll* (1965); *Knowles and Sternberg* (1972); *Marsden and Hughes* (1994); *Barber* (2010)]. Exceeding the elastic limit leads to irreversible microstructural changes like movement of atomic dislocations, growth of mircocracks and microvoids, or results in macroscopic configurational changes involving internal surface creation. The phenomenological descriptions of the microstructural changes, as required by the principles of irreversible thermodynamics, introduce new internal variables whose evolution is the subject matter of the Theory of Plasticity [*Hill* (1950); *Kachanov* (1971); *Lubliner* (1990); *Simo and Hughes* (1998)] for metallic solids, and Damage Mechanics [*Kachanov* (1986); *Krajcinovic* (1989)] for materials with microcracking.

The creation of internal surfaces, referred to as cracks, do not necessarily involve changes in the continuum constitutive response of the intact solid, but is rather a problem of unknown or moving boundaries, driven by the external loading and regular constitutive response of the material. Such problems of evolving boundaries are not uncommon in continuum physics, and some other examples are Stefan's problem of freezing in heat conduction, phase boundaries in multi-phase mixtures, and fluid flow past bodies in the presence of shock waves. The challenge here lies in the prediction of the surface formation and tracking its subsequent evolution. In the context of cracks, this results in "global" non-linearity of the load response which, in general, is not analytically tractable. Further, depending on the microstructure of the material, crack formation may also manifest, in addition to the continuum elastic response, new constitutive relations which can span across different length scales. These additional cohesive relations between the crack face opening and its internal tractions, referred to as traction-separation relations, lead to the more challenging class of cohesive cracks and bridging cracks, where the crack surface may be a diffuse zone of damage rather than a sharp boundary.

Consider the case of through-the-thickness crack propagation in fiber-reinforced composites. Because of the different length scales associated with the microstructure of a composite material and the resulting composite structure, a multitude of failure mechanisms can be simultaneously operative, leading to a very complex damage progression in a composite structure. A sharp, through the thickness crack can be present in these composites initially, but, as soon as local damage (possibly in the form of matrix micro-cracking) accumulates, crack blunting and distributed damage occurs across the highly stressed areas around the initial crack tip. As this initial crack starts to grow, a damaged zone of material (bridging zone) evolves in the wake of the instantaneous crack tip. Thus, unlike in monolithic materials, such as metals, there is actually no well defined "crack" that can be identified. Instead, a diffused zone of damage is seen to advance. This distributed damage results in additional resistance to advancing damage growth, largely due to fiber bridging and pullout in the crack wake . This enhanced fracture resistance is desirable and is a major contributor to the increased toughness of laminated composites [*Cooper* (1970), *Aveston et al.* (1971), *Aveston and Kelly* (1973), *Cox* (1991)].

Overall, the problem of determining and evolving crack boundaries and their interaction with the continuum deformation fields represents a highly nonlinear system, with significant analytical and numerical challenges, which are briefly discussed below.

1.2 Analytical Challenges

The study of crack formation and propagation, referred to as Fracture Mechanics, was founded in the seminal work on brittle cracks by *Griffith* (1921), which introduced the energy-based approach to crack propagation. This was followed by major advances in the form of a stress-intensity based approach of *Irwin* (1957) and softening and plastic process zone models introduced by *Barenblatt* (1962); *Dugdale* (1960), which were further extended by *Cherepanov* (1967); *Rice* (1968). These models are discussed in detail in Section 2.1.1. However, these theories are restricted to brittle or ductile materials with structurally insignificant or small zones of non-linearity ahead of the crack tip (process zones), and thus they cannot be applied directly to derive conditions on crack initiation or propagation in materials characterized by large process zones. This latter class of materials is the focus of the research presented in this work.

Several physical mechanisms may contribute to this type of damage. Microcracking, fiber bridging, coalescence of voids and other microstructural mechanisms can give rise to a process zone that is considerably larger than that permitted for the application of linear elastic fracture mechanics (LEFM) models. Furthermore, the material non-linearity that is induced by these mechanisms leads to a relief of the singular fields at the mathematically sharp crack tip, which would otherwise persist in a strict LEFM setting of an elastic material. A new length scale, $\frac{E\gamma}{\sigma_{max}^2}$, emerges that is related to a characteristic elastic modulus E, fracture toughness γ and cohesive strength, σ_{max}. If this length scale is larger than any characteristic length scale in the problem, then cohesive zone models, which embed process zone mechanics through nonlinear traction-separation relationships across the crack faces, become important tools for analysis [*Pietruszczak and Mroz* (1981); *Ungsuwarungsri and Knauss* (1987); *Song and Waas* (1993); *Schellekens and DeBorst* (1993); *Xu and Needleman* (1994); *Camacho and Ortiz* (1996)]. However determining these traction-separation relations is very challenging, and often subject to the material microstructure as will be illustrated in Section 2.2.1 and Appendix A.

1.3 Numerical Challenges

Numerical schemes, like the finite element method (FEM), have become the mainstay for solution of problems involving any of the broad phenomena of material deformation - elasticity, plasticity and damage; so it may be tempting to use traditional finite element based discretization for problems of crack propagation. However, the distinguishing characteristic of crack problems, in general, is the formation and propagation of sharp boundaries, which are not part of the original boundary value problem. This is not an obstacle if the resulting crack path is known a priori and the mesh is ensured to have elemental surfaces align along possible crack surfaces; but in practice, neither conditions are feasible. For most crack propagation problems, the crack path is not known beforehand and has to be determined as part of the solution process, and in structural level problems, adaptive mesh generation/realignment is prohibitively costly. Furthermore, a standard Galerkin implementation will lead to the introduction of spurious numerical length scales proportional to the element volume as discussed in Section 4.1.

These problems with traditional FEM implementations have been well documented for the phenomena of strain localization, which has similar kinematics to that of crack propagation problems. Thus, it exhibits spurious mesh related length scales [*Needleman and Tvergaard* (1984); *Bazant* (1986); *Crisfield and Wills* (1988); *Armero and Garikipati* (1996)] and problems related to mesh alignment relative to the localization band [*Larsson et al.* (1993); *Ramakrishnan et al.* (1994)].

As will be shown in Chapters IV and V, the multiscale formulation presented in this thesis, involving elemental enrichment to capture the discontinuous modes associated with crack propagation, eliminates these mesh related problems. It is also noted that a comparable, but significantly different development, involving nodal enrichment by partition of unity functions, like the extended finite element (XFEM) [*Moes et al.* (1999); *Moes and Belytschko* (2002); *Dolbow et al.* (2001)] and *Wells and Sluys* (2001) also results in mesh objective simulation of crack problems. The differences between the two approaches will be highlighted in Chapter IV.

1.4 Adopted Approach and Goals

The primary task of this thesis is the development of a numerical framework for cohesive crack propagation and demonstrating its effectiveness by simulating failure through crack propagation in materials with complex microstructure like fiber-reinforced composites. Towards this goal the following approach has been adopted:

1 Reviewing existing theories of brittle and cohesive crack propagation to determine their capabilities and limitations.

2 Developing a general approach to cohesive crack propagation involving large process zones and also obtaining (analytically/numerically) the relevant cohesive constitutive behavior of a class of fiber-reinforced composites.

3 Extending the idea of variational multiscale method presented in *Hughes* (1995); *Garikipati and Hughes* (1998) and developing it on the lines of *Garikipati* (2002) for application to cohesive crack propagation involving discontinuous kinematics.

4 Developing a class of finite elements that objectively simulate crack propagation without introducing any spurious numerical length scales. This involves application of non traditional discontinuous shape functions and relevant quadrature schemes.

5 Implementation of a robust crack tracking algorithm that allows the propagation of the discontinuity surface across elements subject to physically consistent crack propagation directions.

6 Sufficiently benchmarking the developed numerical framework by simulating complex crack propagation problems involving curved cracks, multiple cracks, interacting cracks, etc.

7 Experimentally validating the theoretical and numerical approaches by comparing the load-displacement response and crack paths observed in large scale bridged crack propagation in laminated fiber-reinforced composite specimens.

It is expected that achieving these goals would be sufficient to demonstrate and validate a physically consistent and numerically objective cohesive crack propagation framework.

1.5 Outline

An outline of the rest of the dissertation is as follows. Chapter II reviews the classical theories of crack propagation and later developments relevant to cohesive cracks involving large process zones. It then presents a possible description of the micromechanics behind bridging cracks formation in fiber-reinforced composites. In Chapter III, the variational multiscale concept of problems involving gridscale and subgrid scale phenomena is introduced. Then the concept is extended to cracks represented as discontinuous displacement modes and the relevant weak formulation of the problem is derived. This formulation is then cast in a finite element framework in Chapter IV, which begins with a discussion of the limitations of standard finite element approaches to simulate crack propagation. It then proceeds to the multiscale element construction and development of the discretized equations and an incremental solution procedure. The analytical and numerical framework developed until this point is validated through simulation of various crack propagation problems in Chapter V, and by comparison with experimental observations in Chapter VI. The conclusions and possible areas of future work are summarized in Chapter VII, and lastly a framework for deriving traction-separation relations is discussed in Appendix A.

CHAPTER II

Mechanics of Cohesive Crack Propagation

The study of crack propagation, commonly referred to as Fracture Mechanics, has historically focused on predicting crack evolution in homogeneous materials with brittle or quasi-brittle behavior. However, with the advent of advanced materials like composites, which posses high stiffness, superior damage tolerance and improved thermo-mechanical properties, the traditional approaches to simulate crack propagation are not adequate. The work presented here develops an analytical and numerical framework to address crack propagation in one such important class of advanced materials called fiber composites, which often exhibit large process zone sizes. Towards that goal, this chapter begins with a brief discussion of classical fracture mechanics in Section (2.1.1). Then, an enrichment of classical ideas using the cohesive zone approach proposed by *Barenblatt* (1962) is discussed in Section (2.1.2). The presentation is significantly influenced by *Raizer* (1970). With the theoretical framework laid out, the phenomena of toughening in materials involving large process zones is discussed in Section (2.2) and this is extended to fiber composites in Section (2.3). Finally the closing remarks are provided in Section 2.4.

2.1 Crack Propagation in Cohesive Materials

2.1.1 Classical Fracture Mechanics

From the continuum viewpoint, fracture or crack formation is the creation of new surfaces in the domain of the body. This surface creation invariably leads to loss in the global stiffness and load-bearing ability of the material, often leading to failure. Traditionally, either energy-based or stress-intensity based approaches have been employed to predict this mode of failure. The energy-based theory of failure introduced by *Griffith* (1921) was motivated by the inadequacy of the elastic solution that renders singular stresses at the mathematically sharp crack tip. Subsequently, Griffith's work formed the basis for linear elastic fracture mechanics (LEFM). In this section, a concise discussion of the key elements of LEFM and a subsequent development referred to as the stress-intensity based approach will be presented.

2.1.1.1 Griffith's Energy-Based Theory of Crack Propagation

Consider an infinite plate of uniform thickness under homogeneous tensile stress state, σ_{yy}, produced due to the far-field application of uniform load p $(= \sigma_{yy})$ as shown in Figure (2.1). Considering linear elasticity, the strain energy density of the body is given by $U = \sigma_{yy}^2/2E'$, where E' is the modulus[1]. If a crack of length l, with traction free faces, appears in this infinite domain, then the change in strain energy is given by $\Delta U = -\sigma_{yy}^2 a(l)/2E'$, where $a(l)$ is a positive valued function representing the effective area of stress relaxation in the vicinity of the crack. Also, their is an associated increase in the total surface energy, $\Delta\Pi = 4l\gamma$, where γ is the surface energy density[2].

---

[1] plain-stress condition: $E' = E$ and plain-strain condition: $E' = \frac{E}{1-\nu^2}$, where E is the Young's Modulus and ν the Poisson's ratio.

[2] Surface energy density or surface tension is defined as the energy required to create a surface of unit cross sectional area in the continuum volume. From a micromechnical viewpoint, this energy is required to overcome the surface cohesive forces.

REMARK: Elasticity theory involves only volumetric energy and has no concept of a surface energy; thus stand-alone application of classical elasticity can predict the stress state around a preexisting crack, as shown by *Kolosov* (1909); *Inglis* (1913) and *Muskhelishvili* (1919) but cannot yield conditions on either initiation of new cracks or propagation of existing cracks. *Griffith* (1921) introduced this concept to distinguish fracture from elasticity and thereby derive conditions for crack initiation and unstable propagation. Of course, his presentation did not detail the micromechanics of surface formation, and considered γ as a macroscopic material property.

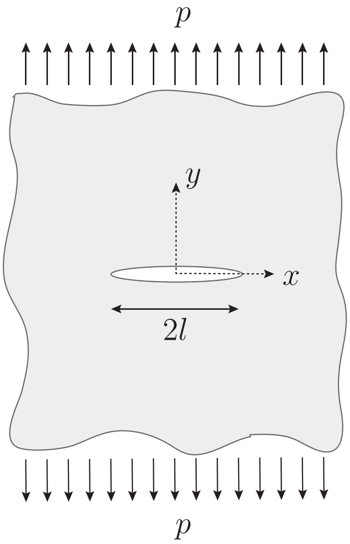

Figure 2.1: *Crack in an infinite plate of uniform thickness.*

Consider now the free energy[3] of the quasi-static system, $\Delta F = \Delta U + \Delta\Pi$, and its derivatives are given by

$$\frac{\delta F}{\delta l} = -\frac{\sigma_{yy}^2 a'(l)}{2E'} + 4\gamma \tag{2.1a}$$

$$\frac{\delta^2 F}{\delta l^2} = -\frac{\sigma_{yy}^2 a''(l)}{2E'} \tag{2.1b}$$

Then, for spontaneous occurrence of a crack of length $2l$, which renders a new equilib-

---

[3] Referred to as potential energy in *Griffith* (1921)

rium state, the free energy has to be stationary. This stationarity condition, $\frac{\delta F}{\delta l} = 0$, shows that the decrease in strain energy is equal to the surface creation energy, and yields a value of critical loading, $p_{crit} = \sqrt{8\gamma E'/a'(l)}$. It is tacitly assumed that, during the occurrence of crack, no external work is done on the system, thus resulting in only internal transformation of energy. Using the exact expression for $a(l)$ for the plane strain condition, *Griffith* (1921)) obtained $p_{crit} = \sqrt{2\gamma E'/\pi l}$. Further, for this geometry and loading conditions, $a''(l) > 0$, which implies that the new equilibrium state is unstable. Thus for $p > p_{crit}$, l increases catastrophically, and for $p < p_{crit}$, l remains unchanged at its original value[4]. So the necessary condition for crack propagation is

$$\frac{\sigma_{yy}^2 a'(l)}{2E'} \geq 4\gamma \qquad \text{(Energy-based crack propagation criterion)} \tag{2.2}$$

The terms $-\frac{\delta U}{\delta l}$ and $\frac{\delta \Pi}{\delta l}$ are usually referred to as the energy release rate and material resistance, and denoted by symbols G and R, respectively. In general, G and R are functions of l, so the corresponding free energy and equilibrium conditions are

$$\Delta F = -G\Delta l + R\Delta l \tag{2.3a}$$

$$\frac{\delta F}{\delta l} = -G + R \leq 0 \tag{2.3b}$$

$$\frac{\delta^2 F}{\delta l^2} = -\frac{\delta G}{\delta l} + \frac{\delta R}{\delta l} > 0 \qquad \text{(Stable propagation)} \tag{2.3c}$$

$$\frac{\delta^2 F}{\delta l^2} = -\frac{\delta G}{\delta l} + \frac{\delta R}{\delta l} < 0 \qquad \text{(Unstable propagation)} \tag{2.3d}$$

Thus, Griffith's theory, based on surface energy and the resultant stationarity of free energy, yields an expression for critical loading for unstable crack extension. However, analytical estimation of ΔU, the change in the strain energy, as a function of

---

[4] The crack length cannot decrease as $t \mapsto l(t)$ is a monotonically increasing mapping. This is a physical requirement as rearrangement and relaxation of surface atoms preclude the possibility of crack closure.

l is only possible for simple problems. This limits the application of the energy-based approach to complex geometries and loading conditions.

2.1.1.2 Irwin's Stress-Intensity Based Theory of Crack Propagation

The key idea behind the stress-intensity based theory is the observation that the near tip crack field in isotropic linear elastic materials is similar for all specimen geometry and loading conditions, to within a constant. For the crack loading shown in Figure (2.1), *Williams* (1952); *Irwin* (1957) obtained the crack tip opening stress and corresponding displacement along the x-axis,

$$\sigma_{yy} = \frac{N}{\sqrt{x}} + O(1) \tag{2.4a}$$

$$u_{yy} = \frac{4N}{E'}\sqrt{|x|} + O(x^{3/2}) \tag{2.4b}$$

where O denotes the higher order terms in the asymptotic expansion of the singular stress field. The constant N, referred to as the *coefficient of stress intensity*, determines the stress and strain field in the vicinity of the crack tip, and is depended on the specimen geometry, crack dimensions and loading conditions. Having derived the stress and strain fields, *Irwin* (1957) proposed the following crack closure analysis to determine the value of the energy release rate, G.

Consider Figure (2.2), where the crack has extended by a distance δl from its original position A to A'. Assume that the boundaries are held fixed, so that no energy exchange takes place between the system and its surroundings due to changes in external forces. Consider a new coordinate system (x', y') positioned at A. Now apply fictitious forces on the section $A - A'$, such that they are just enough to close the crack opening in this section. The magnitude of the displacement of each face required for crack closure along this section is given by $u_{y'y'} = u_{yy}(x' - \delta l)$ for small δl,

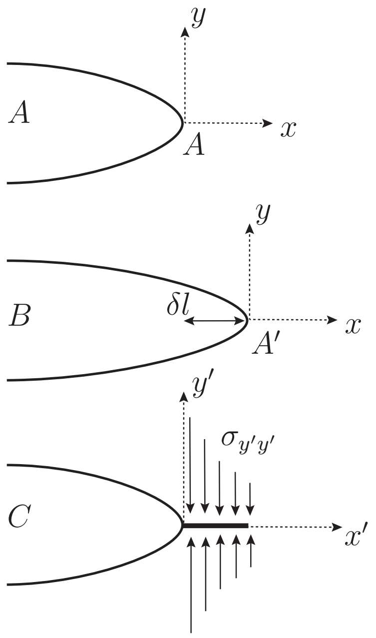

Figure 2.2: *Crack closure analysis to determine the energy release rate: (A) Initial crack profile, (B) Extended crack profile, (C) Crack Closure.*

and the corresponding stress along the closed section is given by $\sigma_{y'y'} = \sigma_{yy}(x')$. Using these, the work done in achieving crack closure, which directly contributes towards increasing the strain energy of the body, is given by

$$\Delta U = 2 \cdot \frac{1}{2} \int_{0}^{\delta l} \sigma_{y'y'}(x') u_{y'y'}(x') \; dx' = \frac{2\pi N^2 \delta l}{E'} \tag{2.5}$$

Now if we assume that the fictitious forces are released, the crack tip rebounds to A', resulting in a $-\Delta U$ change in the strain energy. So the strain energy release rate given by $G = -\frac{\delta U}{\delta l}$ is

$$G = \frac{2\pi N^2}{E'} \tag{2.6}$$

Having obtained the energy release rate from the stress-intensity based approach, one can use Equations (2.3b), (2.3c), (2.3d) to determine the crack propagation and stability conditions. Substituting G and R (=$2\gamma\delta l$) into Equation (2.3b), we obtain the stress-intensity based crack propagation criterion

$$\frac{\pi N^2}{E'} \geq \gamma \qquad \text{(Stress-intensity based crack propagation criterion)} \tag{2.7}$$

Both the energy-based criterion (Equation (2.2)) and stress-intensity based criterion (Equation (2.7)) in many cases can be shown to be equivalent statements, and this equivalence can be seen through the Equation (2.6).

The classical crack propagation approaches presented above use the linear theory of elasticity to deliver necessary conditions for crack initiation and propagation, and in doing so use macroscopic energy (Equation (2.1a)) or asymptotic stress field (Equation (2.4a)) arguments, which contain solutions with infinite stress values at the crack tip. However, in real materials, either non-linear phenomena like plasticity limit the stress to finite values, or atomic-level phenomena like cohesive separation occur, thus rendering the high stress values predicted by the linear theory meaningless. Further, there is an inherent contradiction in the use of a linear theory, which by definition is only applicable to small deformations, to predict infinite stress and strain values. The traditional argument against these contradictions is that the volume of the zone over which these crack tip non-linear phenomena are active (termed the *process zone*) is significantly smaller compared to the volume over which the singular field terms (varying as $\frac{1}{\sqrt{r}}$) are predominant. This assumption of a small process zone, which implies that the "local" crack-tip non-linearities do not significantly effect the "global" energy or stress field solutions, is central to LEFM, which deals with the application of the above energy-based and stress-intensity based approaches.

2.1.2 Small Process Zone and Barenblatt Cohesive Model

To address the inconsistency of infinite stresses at the crack-tip, a theory involving non-linear process zone mechanics was presented in *Barenblatt* (1962); *Dugdale* (1960) for symmetric crack propagation in homogeneous isotropic materials. Consider the physical picture of surface formation from an atomistic viewpoint. As the body is loaded, certain points with material defects or geometric singularities undergo significant stretching of atomic bonds, which eventually leads to loss of inter-atomic cohesion and traction free surface creation. This transition from bond stretching to surface creation is gradual, and thus the physical picture of the crack opening profile should be comparable to Figure (2.3B), rather than the $\sqrt{x}$ opening profile predicted by LEFM theory (Equation (2.4b)). Further, the order of magnitude of the forces involved in this zone of cohesive bond stretching and weakening (termed the *cohesive zone*) can be orders of magnitude higher than the far-field stresses. Therefore the external loading conditions and specimen geometry have little influence on the crack profile in the cohesive zone, which is under the influence of much larger cohesive forces. This implies

- The cohesive forces are concentrated near a small, but finite region of the continuum crack tip and drop to zero within few atomic distances from the crack tip; this is equivalent to the small process zone assumption in LEFM.

- For a given material, the crack profile in the cohesive zone is universal (independent of the loading, geometry and crack dimensions).

This universality condition of the crack profile, termed as the *autonomy of the crack end*, is central to the theory of Cohesive Zone Model (CZM) of fracture, and states that "in the mobile-equilibrium state, the heads of all cracks in a given material are the same".

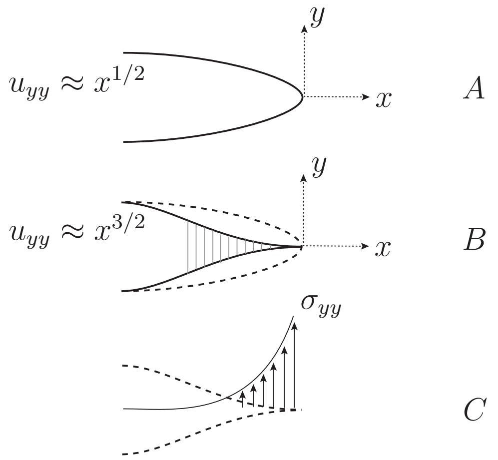

Figure 2.3: *Crack opening profile due to the influence of cohesive forces in the crack wake: (A) Crack profile obtained from classical analysis ($u_{yy} \approx x^{1/2}$); characterized by infinite stresses at the crack-tip, (B) Crack profile obtained in the presence of cohesive forces ($u_{yy} \approx x^{3/2}$); characterized by finite stresses (C) Opening stress profile at the cohesive crack tip.*

The primary argument of *Barenblatt* (1962) to remove the unphysical stress singularity implies $N_t = 0$ (Equation (2.4a)). Here $N_t = N + N_G$, where N and N_G are the coefficients of stress intensity due to the external loading and cohesive forces, respectively. Substituting $N_t = 0$ in Equation (2.4b), we are left with the crack opening profile, $u_{yy} \approx x^{3/2}$, which is depicted in Figure (2.3B). The requirement of $N_t = 0$ leads to the following condition for crack propagation:

$$N \geq \frac{K}{\pi} \qquad \text{(Cohesive-model crack propagation criterion)} \tag{2.8}$$

and,

$$K^2 = \pi E' \gamma\,' \tag{2.9a}$$

$$\gamma\,' = \frac{1}{2} \int_0^\infty T(\delta)\, d\delta \tag{2.9b}$$

where K is the *modulus of cohesion*, $\gamma\ '$ is the *fracture toughness*[5] of the cohesive zone, and $T(\delta)$ is the non-linear cohesive traction in the crack wake and δ is the crack opening displacement which is hereafter referred to as the crack separation. Using Equations (2.6) and (2.8), *Willis* (1967) showed the equivalence of LEFM based on Griffith theory and the Barenblatt CZM model, provided that the cohesive surface energy density is equal to the fracture toughness ($\gamma\ = \gamma\ '$).

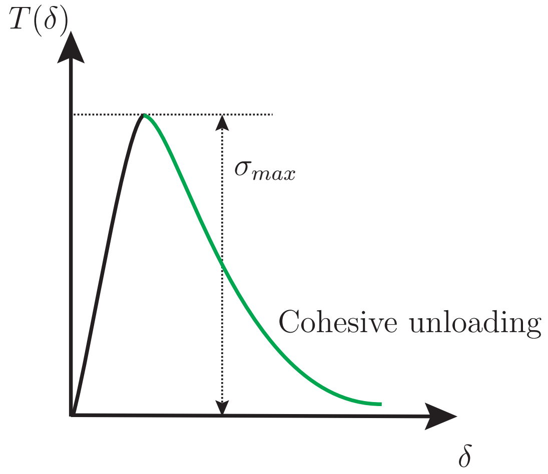

Figure 2.4: *Schematic of a possible cohesive traction function.* σ_{max} *is the maximum opening stress value up to which the linear analysis, shown in black, is valid. Upon achieving this value, the relevant constitutive law switches from linear elasticity to the non-linear cohesive relationship shown in green.*

A representative non-linear cohesive traction function, $T(\delta)$, which is a material property input to CZM is shown in Figure (2.4). In real materials, however, determining $T(\delta)$ is very challenging and often material subjective. Especially, in materials with complex microstructure, determining $T(\delta)$ involves detailed understanding of the crack wake micromechanics. Also, the crack wake processes, involved in modern materials, which demonstrate high fracture resistance, do not satisfy the small process zone assumption of LEFM and CZM.

---

[5] Fracture toughness is defined as the energy required to create a traction free surface of unit cross sectional area by overcoming all crack wake resistances due to cohesive forces, material-nonlinearities, etc.

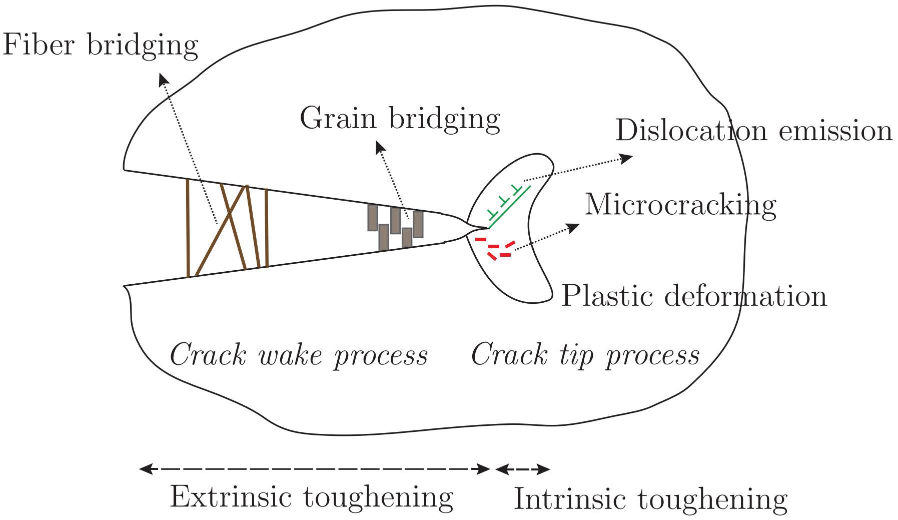

Figure 2.5: *Schematic of a various toughening mechanisms. In a crack propagation scheme, crack wake (extrinsic) toughening contributes to the bridging traction-separation relation and crack tip (intrinsic) toughening is accounted for in the cohesive traction-separation relation.*

2.2 Crack Propagation in Bridging Materials

The resistance to crack growth due to cohesive, non-linear or microstructural phenomena ahead/behind the crack tip is generally referred to as *toughening*, and the region over which these processes are significant is called the *process zone*. Figure (2.5) depicts some of the prominent toughening phenomena observed in materials. In traditional homogeneous materials, like monolithic metals, the toughening is localized at the crack tip and the resulting process zone size is negligible when compared to the crack dimensions. Further the process zone is always *ahead* of the crack. This allows the direct use of LEFM or CZM methods to predict crack initiation and propagation, due to this localized nature of the process zone. On the other hand, modern materials with complex microstructures, like fiber composites, demonstrate exceptionally high fracture toughness due to high crack wake bridging tractions and large process zone sizes which are comparable to the crack dimensions, as shown in Figure 2.8. In a composite, during crack growth, a process zone *ahead* of the crack and a bridging zone *in the wake* of the crack, both provide toughening. This large process zone size implies the classical approaches to fracture cannot be directly applied. Further, the evolutionary nature of the sizes of the cohesive zone and bridging zone limit the application of analytical methods, and almost always requires the use of numerical methods such as the finite element method, to solve the resulting equations.

The remainder of this chapter, and subsequent chapters will focus on developing a numerical framework for the problem of crack propagation involving large process zones, based on the finite element method.

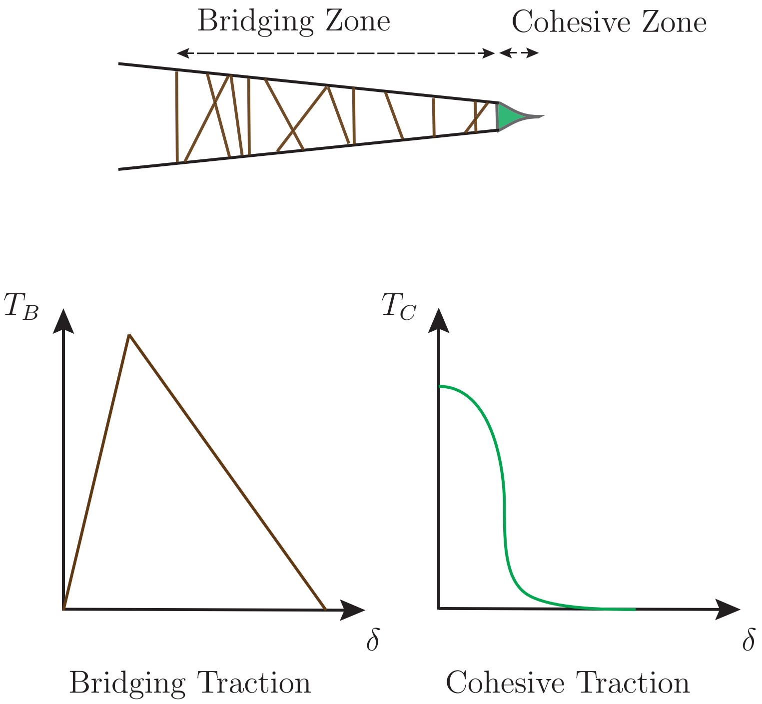

Figure 2.6: *Schematics of possible bridging traction-separation and cohesive traction-separation relations.*

2.2.1 Large Process Zone and Traction-Separation Models

Consider Figure (2.6) which depicts the traction-separation relations for a problem with a large bridging zone during crack growth. Since the extrinsic toughening considered is due to traction in the fibers bridging the crack faces, this particular crack wake toughening process is referred to as bridging toughening, and the corre-

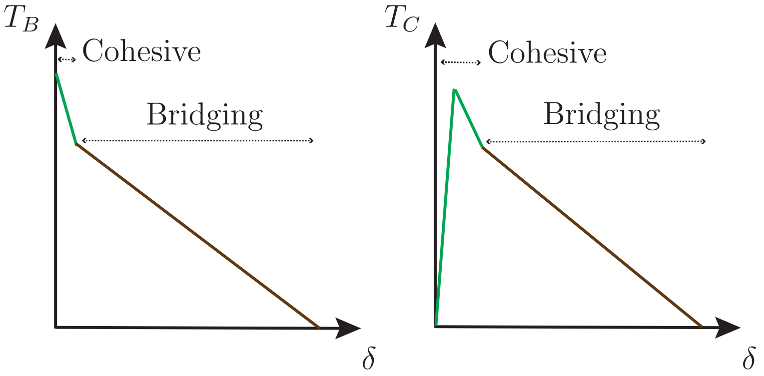

(A) (B)

Figure 2.7: *Schematic of possible mixed cohesive-bridging traction-separation relations (A) Physically consistent as cohesive relation begins at finite traction, (B) Physically inconsistent as cohesive relation begins at zero traction.*

sponding materials are referred to as bridging materials.

As discussed earlier, the cohesive zone process is localized and is characterized by sharply dropping tractions within a short distance of the crack tip. Further, since the cohesive zone mechanisms are always subsequent to a certain amount of linear deformation, the corresponding tractions-separation relationship should begin at a non-zero traction value. On the other hand, the bridging zone process is distributed over distances comparable to the crack dimension, and the tractions will start at zero, build up and drop more gradually [6]. Now the challenge is to embed these two distinct toughening processes into a numerical framework to produce physically consistent crack evolution. There are two possible approaches to this:

- Implement the two processes separately and use the corresponding traction-separation relations. So a point in the crack path begins with a cohesive traction relation and gradually transfers to a bridging traction relation.
- Determine a cumulative traction-separation relation encompassing both these processes, and then treat the resultant non-linear constitutive relation as a

---

[6] It is noted that depending on the specific micromechanics, the starting traction in a bridging traction-separation relationship may or may not be zero

standard CZM $T(\delta)$ relation. However the chosen relation should be physically consistent, as shown in Figure (2.7 A). For instance, Figure (2.7 B) shows an inconsistent mixed traction relation.

The latter approach is numerically more appealing and widely applied. However, such a cumulative traction-separation relation will be problem and geometry subjective as shown in *Li et al.* (2005). A detailed discussion of both the above approaches can be found in *Sun and Jin* (2006).

2.2.2 Cohesive Zone Model and Other Numerical Methods

Subsequent to the pioneering work by Barenblatt, the implementation of a CZM incorporating a finite element framework lay dormant until the work of *Hillerborg et al.* (1976). In parallel, other numerical techniques emerged to implement the LEFM methodology that found favor amongst practicing engineers. Therefore a brief review of LEFM based numerical methods is presented here, before moving to the developments in CZM.

Among fracture parameters, the strain energy release rate has been used increasingly used in conjunction with LEFM. It can be computed by the virtual crack closure technique (VCCT) [*Xie and Biggers* (2006b)], in conjunction with finite element analysis. This method requires a pre-existing mathematically sharp crack for initiation and conditions of small scale yielding to hold. With negligible material non-linearity at the crack tip (small process zone size), LEFM based approaches have been proven to be effective in predicting crack initiation and subsequent growth [*Hertzberg* (1983); *Xie and Biggers* (2006b,a); *Xie et al.* (2004, 2005); *Xie and Waas* (2006); *Salvi et al.* (2008)]. But as discussed earlier, often crack growth in composite materials and structures made of other quasi-brittle materials, the process zone size may be larger than any characteristic length scale in the problem leading to situations where the assumptions of LEFM cease to hold [*Xie et al.* (2006)]. Several mechanisms like micro-cracking, fiber bridging, coalescence of voids, etc can give rise to a process zone that is considerably larger than what is required for assumptions of LEFM to hold. A new length scale, l^*, emerges that is related to a characteristic elastic modulus E, fracture toughness γ and cohesive strength, σ_{max}, defined as, $l^{*2} = \frac{E\gamma}{\sigma_{max}^2}$. If l^* is larger than any characteristic length scale in the problem, then the cohesive zone models, which embed process zone mechanics through nonlinear traction-separation relationships across the crack faces become an important tool for analysis.

Subsequent to the work of *Hillerborg et al.* (1976), the crack band model which incorporates a characteristic length, l^*, was introduced by *Bazant and Oh* (1983). Around the same time, CZM development, in the form of nonlinear spring foundations was adopted by *Ungsuwarungsri and Knauss* (1987) to study crazing in polymers and by *Song and Waas* (1993) to study delamination fracture in laminated composites. Because of its versatility, CZM models became a popular choice for many fracture problems that were studied using a FE framework as detailed in *Pietruszczak and Mroz* (1981); *Xu and Needleman* (1994); *Pandolfi et al.* (1999). In order to implement a CZM in its simplest form, two parameters are required: a fracture toughness and a cohesive strength. The choice of these parameters and how they are measured and/or calibrated depends on the problem that is being addressed. In general, the CZM parameters are "system" parameters and are related to the material system that is being studied. The fracture toughness can be obtained from coupon level tests of the material system under study, for example through Compact Tension Specimen (CTS) test mentioned in Section 6.1. This measured toughness value in conjunction with a CZM simulation of the test can be used to back out the cohesive strength. Alternatively, both the toughness and strength can be measured from coupon level tests for subsequent use in prediction of crack growth in other structural configurations.

In a CZM, an existing crack starts to grow when the stress at the crack tip attains the cohesive strength and when there is sufficient energy supplied from the system to create new cracked area associated with the advancing crack. Thus, unlike LEFM, which requires one parameter, a CZM strategy requires two parameters for predicting crack growth. A cohesive law combines fracture energy and cohesive strength to describe the resistance offered to crack advancement within the cohesive zone. Various postulated forms of cohesive laws (such as triangular, exponential, trapezoidal, multi-section, etc.,) have been attempted in conjunction with CZM [*Espinosa et al.* (1998); *Li et al.* (2005); *Jin and Sun* (2005); *Gustafson and Waas* (2009)]. These studies, however, have shown that the form of the phenomenological cohesive law are less important than the well-posed implementation, when CZM is used with finite element analysis. However, a major drawback of CZM based methods is the fact the intended crack path must be known a priori in order to place the CZM elements appropriately in a finite element mesh. Thus, the CZM strategies are not practical for predicting crack growth in a solid under general loading conditions.

2.3 Crack Propagation in Fiber Reinforced Composites

Fiber reinforced composites are composed of tough fibers distributed in a matrix medium, thereby inheriting some structural characteristics from both the constituents. Often used combinations are metal or ceramic fibers in a matrix of ceramic, glass, polymer or intermetallics. Further, the distribution and layup of the fibers in the matrix lead to various material architectures like short-fiber, continuous-fiber, laminated, textile, etc. Given the huge diversity in the constituent materials and layups, the presentation in this thesis is restricted to the extensively used class of Carbon Fiber Reinforced Polymer (CFRP) laminated composites, hereafter referred to as *fiber composites*. However, the generality of the presentation allows its potential application to many other classes of fiber reinforced composites. The most significant property of this material is the high specific strength (strength per unit weight), even in the presence of holes and notches, which are integral to any practical structure. But high strength is of little use unless it is complimented by significantly high toughness (i.e, resistance to damage and crack propagation).

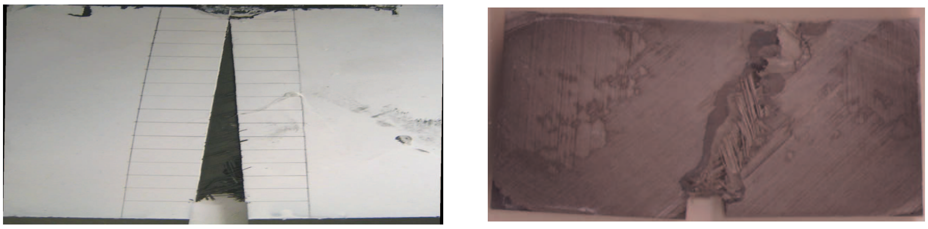

Straight Crack Curved Crack

Figure 2.8: *Complexity and diffused damage observed in fiber composites.*

The inherent complexity of the microstructure of fiber composites, as shown in Figure (2.8), clearly distinguish their toughening mechanisms from those of traditional monolithic matrix materials like metals. While the fibers add to the macroscopic toughness of the material, the fiber-matrix interfaces also present material and geometric discontinuities which are possible sites for crack initiation and growth. Depending on the plane of crack propagation with respect to the material layup, crack propagation can lead to:

- *Delamination*, or the occurrence of inter-lamina cracks which can lead to failure of the laminate. This is a special case, where the cracks are "macroscopically" planar and is usually associated with adhesive or matrix failure. This class of problems has been extensively studied, both analytically and numerically, owing to a priori knowledge of the crack path (Section (4.1) details the numerical issues).
- *Through-Thickness failure*, or the occurrence of cracks through the laminate such that the crack plane is not parallel to that of the lamina, involving ex-

tensive fiber and matrix failure. This is analytically and numerically more challenging, partly due to the complexity of micromechanics leading to failure and comparatively more involved crack path prediction and evolution.

The work presented here seeks to address the complexity involved in through-thickness failure, which can be argued to be more general and challenging in comparison to delamination, in the context of the crack propagation problem. Further, the primary interest in this work is not to understand the physics behind these failure phenomena but rather to develop a numerical framework for predicting through-thickness crack propagation. In the homogeneous continuum setting to be considered in this work, all the relevant mechanics behind crack formation and propagation are characterized by a traction-separation model, which is the sole constitutive input determining crack evolution. However, determining the relevant traction-separation model is major challenge in itself. Depending on the necessary material non-linearity and mechanics complexity, one could either analytically or numerically obtain the traction-separation models. Towards this goal, an overview of a possibly relevant micromechanical processes of fiber pullout are presented in Section (2.3.1), and the corresponding analytical and numerical framework is detailed in Appendix A.

2.3.1 Micromechanics

The basic phenomena which give rise to the non-linear behavior leading to failure by through the thickness crack propagation are shown in Figure (2.9), and can be categorized as:

- *Interface failure*: Initial fiber loading leading to increasing shear stress at the fiber-matrix interface, which eventually leads to Mode-II interface crack formation.
- *Interface crack propagation and frictional dissipation*: Interface crack propaga-

tion leads to relative motion between the free surfaces of the fiber and matrix, leading to static or dynamic coulomb type frictional forces. This leads to frictional dissipation with the opposing contact forces enhancing the load carrying ability of the fibers.

- *Fiber pullout*: The interface crack eventually traverses the entire embedded fiber length or the fiber breaks due to critical loading of some weak zones. This phase is associated with loss in fiber load carrying ability due to pullout with only the associated frictional sliding providing the resistance.
- *Matrix cracking*: Independent of the above fiber driven processes, the matrix can undergo damage through microcracking, resulting in increased elastic compliance and energy dissipation.

These processes together result in a diffused damage zone which microscopically is heterogeneous and stochastic, but macroscopically is seen as a region of localized ‘crack-like’ damage as shown in Figure (2.8), and for all practical purposes will be treated as a continuum level crack that has a traction relation which accounts for the toughening mechanisms. As stated earlier, since the final framework is that of a homogenized continuum, the medium through which the above micromechanical phenomena are embedded into the continuum formulation is the traction-separation model. The detailed presentation of the analytical and numerical framework for obtaining appropriate traction-separation models is given in Appendix A, where it is demonstrated that the above phenomena correspond to different loading and unloading regions of the traction-separation model. However, in this framework matrix microcracking is neglected, as it is usually dealt with via continuum damage models rather than a continuum cracking approach.

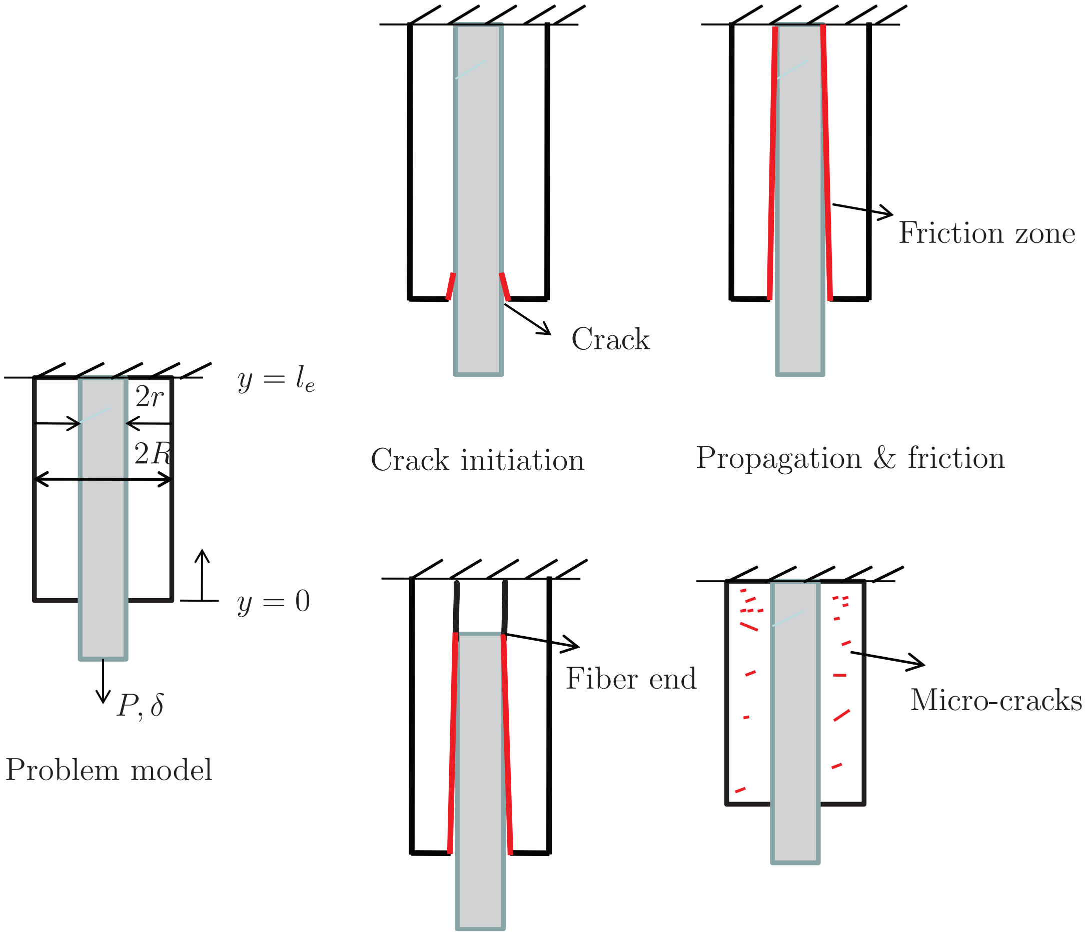

Problem model

Crack initiation

Propagation & friction

Fiber pullout

Matrix cracking

Figure 2.9: *Schematic depicting various modes of micromechanical damage evolution observed during the process of through thickness crack propagation. The red color lines represent cracks.*

2.4 Closing Remarks

A review of the classical theories of LEFM has been presented, along with the subsequent development of the cohesive zone concept. Then the limitations of the classical approaches to advanced cohesive materials are addressed through a discussion of various intrinsic and extrinsic toughening mechanisms. This was followed by a discussion of the numerical developments related to the cohesive zone models. Then the micromechanical phenomena leading to toughening of fiber-reinforced composites have been discussed with the relevant analytical and numerical frameworks presented in Appendix A. With this, the necessary analytical foundation for cohesive crack propagation in this class of materials has been laid out, and we now proceed to the discussion of a multiscale formulation of the crack problem.

CHAPTER III

Multiscale Framework and Variational Formulation

3.1 Background and Variational Multiscale Concept

Physical processes spread across space and time scales are ubiquitous. Often the complexity involved in understanding these phenomena is non-trivial and one has to resort to empirical, phenomenological models to make them more approachable. Further, the fidelity of these models is geared towards conforming to the ultimate framework (analytical or numerical) used to simulate the physical phenomena. Thus, there is a constant drive towards development of better scale-aware analytical and numerical formulations. Focusing our attention on the related numerical developments, it is common knowledge that straightforward application of the widely used Galerkin's method employing standard basis functions (fourier series, finite elements, etc.) is not a robust approach in the presence of multiscale phenomenon as certain far-scale or sub-scale processes are not sufficiently/objectively resolved (demonstrated in Section 4.1), which can give rise to fictitious length and time scales in the solution. To address this issue of disparate scales in numerical schemes, a new computational paradigm called the Variational Multiscale Method (hereafter referred to as VMM) was introduced by *Hughes* (1995). Initially developed to address the question of 'intrinsic time scale' in stabilized methods like Galerkin/least-squares (GLS), Streamline upwind/Petrov-Galerkin (SUPG) (*Hughes et al.* (1998)), the VMM approach resulted in giving a unifying perspective of many previous numerical frameworks that address various sub-scale phenomena. One such effort from which this thesis draws inspiration is by *Garikipati and Hughes* (1998, 2000), in which the process of strain localization as a multiscale problem was presented, and a unifying picture of various scale regularization based formulations like the composite damage model, crack band model and non-local strain model were discussed. The point of departure in the current work is the characterization of displacement discontinuity due to cracks as a 'fine-scale', and its subsequent coupling to the continuum fields via micromechanical surface laws. As a background to the presentation in this work, we briefly discuss the physical picture of the broad classification of multiscale problems introduced in *Hughes* (1995); *Hughes et al.* (1998).

3.1.1 Grid Scale model: Large-scale and Small-scale

Consider the exterior problem of the Helmholtz operator which models wave propagation in free space due to a localized source, stated as follows: For $\Omega \subset \mathbb{R}^3$, find $u : \Omega \to \mathbb{C}$ such that for given $f : \Omega \to \mathbb{C}, \quad g : \Gamma_g \to \mathbb{C}$ and $h : \Gamma_h \to \mathbb{C}$,

$$\mathbb{L}u = f \qquad in \quad \Omega \tag{3.1a}$$

$$u = g \qquad on \quad \Gamma_g \tag{3.1b}$$

$$u_{,n} = ikh \qquad on \quad \Gamma_h \tag{3.1c}$$

$$\lim_{r\to\infty} r\ (u_{,r} - iku) = 0 \quad \text{(Sommerfeld radiation condition)} \tag{3.1d}$$

where $-\mathbb{L} = \Delta + k^2$ is the Helmholtz operator, $k \in \mathbb{C}$ is the wave number, i is $\sqrt{-1}$ and r denotes the radial coordinate. Also let the following decomposition of the

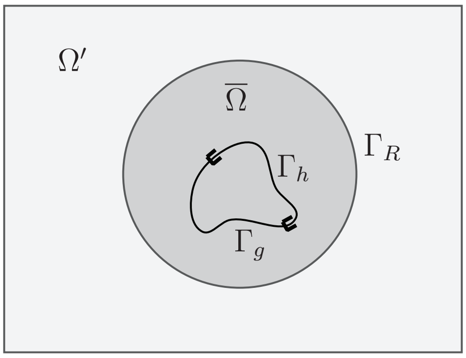

Figure 3.1: *Decomposition of* Ω *into* $\overline{\Omega}$ *and* Ω' *and their boundary* Γ_R*.* Γ_h *and* Γ_g *are the neumann and dirichlet boundary sections of* Γ*.*

boundary be admitted,

$$\Gamma = \overline{\Gamma_g \cup \Gamma_h} \tag{3.2a}$$

$$\emptyset = \overline{\Gamma_g \cap \Gamma_h} \tag{3.2b}$$

From a numerical standpoint, Equation (3.1d) presents a problem, as we cannot handle this infinite-domain boundary condition in conventional bounded-domain discretization methods like finite elements. So a unique domain and field decomposition is introduced to solve this problem. The decomposition is as follows

$$\Omega = \overline{\overline{\Omega} \cup \Omega'} \tag{3.3a}$$

$$\emptyset = \overline{\Omega} \cap \Omega' \tag{3.3b}$$

$$u = \overline{u} + u' \tag{3.3c}$$

$$\overline{u}|_{\Omega'} = 0,\ u'|_{\overline{\Omega}} = 0 \quad \text{(disjoint additive decomposition)} \tag{3.3d}$$

where Γ_R is the boundary between $\overline{\Omega}$ and Ω' as shown in Figure 3.1. Equation (3.3d) results in the solution field u being decomposed into a far-field u' and a near-field $\overline{u}$. The far-field u' is numerically 'unresolvable' due to the boundary-condition at infinity as in Equation (3.1d). So the approach suggested in *Hughes* (1995) is to analytically determine u' on the following exterior dirichlet problem,

$$\mathbb{L}u' = f \qquad in \quad \Omega' \tag{3.4a}$$

$$u' = \overline{u} \qquad on \quad \Gamma_R \quad \text{(continuity condition)} \tag{3.4b}$$

$$\lim_{r\to\infty} r\ (u,'_r - iku') = 0 \tag{3.4c}$$

and then use this solution to embed its effect into the following bounded domain problem for $\overline{u}$, through the continuity condition Equation (3.4b) which manifests as Equation (3.5d),

$$\mathbb{L}\overline{u} = f \qquad \text{in} \quad \overline{\Omega} \tag{3.5a}$$

$$\overline{u} = g \qquad \text{on} \quad \Gamma_g \tag{3.5b}$$

$$\overline{u},_n = ikh \qquad \text{on} \quad \Gamma_h \tag{3.5c}$$

$$\overline{u},_n = -M\overline{u} \qquad \text{on} \quad \Gamma_R \tag{3.5d}$$

Equation (3.5d) is what is called a Dirichlet-to-Neumann condition [*Hughes* (1995)] on the boundary Γ_R which separates $\overline{\Omega}$ from Ω'. M is an integral operator obtained by solving Problem (3.4) using a Green's function approach; it embeds the far-field phenomena into the near-field problem. The boundary-value problem in Equations (3.5) is now solvable using a finite-domain numerical formulation like finite elements. The field decomposition in Equation (3.3c) can be interpreted as a multiscale problem, with u' representing the far field large scales and $\overline{u}$ representing the near field small scales.

REMARK: Since herein the decomposition was primarily at the domain level (or in numerical parlance, at the grid level) into $\overline{\Omega}$ and Ω', one may refer to this as a 'grid' scale model. This will help distinguish this model from the more useful and physically motivated ‘subgrid’ scale model presented in the following subsection.

3.1.2 Subgrid Scale model: Coarse-scale and Fine-scale

Now consider an abstract Dirichlet problem: For $\Omega \subset \mathbb{R}^3$, find $u : \Omega \to \mathbb{R}$ such that for given $f : \Omega \to \mathbb{R}, \quad g : \Gamma \to \mathbb{R}$,

$$\mathbb{L}u = f \qquad in \quad \Omega \tag{3.6a}$$

$$u = g \qquad on \quad \Gamma \tag{3.6b}$$

where $\mathbb{L}$ is a general non-symmetric operator. Also, keeping in mind the numerical scheme we are leading up to, we explicitly consider a variational treatment for this problem:

For $\mathcal{S} \subset H^1(\Omega)$ and $\mathcal{V} \subset H^1(\Omega)$, where $H^1(\Omega)$ is the Sobolov space of square integrable functions with square integrable derivatives, find $u \in \mathcal{S} = \{v| \ v = g \text{ on } \Gamma\}$, such that $\forall \ w \in \mathcal{V} = \{v| \ v = 0 \text{ on } \Gamma\}$,

$$\int\limits_{\Omega} w\mathbb{L}u \ dV = \int\limits_{\Omega} wf \ dV \tag{3.7a}$$

$$\text{or} \qquad a(w, u) = (w, f) \tag{3.7b}$$

The physical picture of the field u being addressed here is shown in Figure (3.2). Now from a numerical standpoint, fields with such ‘fine’ variations pose a difficulty, as the resolution of these fields becomes subjective with respect to the numerical discretization. This is because these variations occur on physical length scales that are usually smaller than the size of the numerical grid, and it is for this reason that the numerical treatment of problems under this class requires a subgrid scale model. Often in physical phenomena like turbulent flow, strain localization, phase

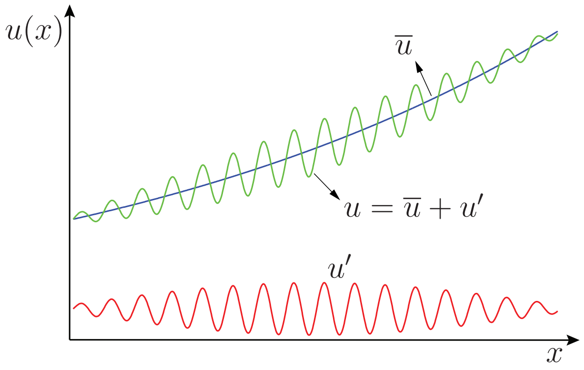

Figure 3.2: *Decomposition of u into coarse-scale field, $\overline{u}$, and fine-scale field, u'.*

separation and crack formation, these fluctuations [1] are at such small length scales that the optimal discretization required in a standard Galerkin implementation is prohibitively expensive, or even impossible. For such cases, consider the following decomposition of u and w into coarse and fine scales,

$$u = \underbrace{\overline{u}}_{\text{coarse scale}} + \underbrace{u'}_{\text{fine scale}} \quad \text{(overlapping additive decomposition)} \tag{3.8a}$$

$$\overline{u} = g, \;\; u' = 0 \quad \text{on} \quad \Gamma \tag{3.8b}$$

$$w = \underbrace{\overline{w}}_{\text{coarse scale}} + \underbrace{w'}_{\text{fine scale}} \quad \text{(overlapping additive decomposition)} \tag{3.9a}$$

$$\overline{w} = 0, \;\; w' = 0 \quad \text{on} \quad \Gamma \tag{3.9b}$$

and their respective vector spaces are,

$$\overline{u} \in \overline{\mathcal{S}}, \;\; u' \in \mathcal{S}' \quad \text{where } \mathcal{S} = \overline{\mathcal{S}} \oplus \mathcal{S}' \tag{3.10a}$$

$$\overline{w} \in \overline{\mathcal{V}}, \;\; w' \in \mathcal{V}' \quad \text{where } \mathcal{V} = \overline{\mathcal{V}} \oplus \mathcal{V}' \tag{3.10b}$$

where $Z = X \oplus Y$ means Z is a function space whose elements are ordered pairs (x, y).

---

[1] In crack propagation, which is the problem of interest in this work, the fine-scale field, u', is not oscillatory, but rather a discontinuity. But for the abstract presentation in this section, the more general oscillatory picture of fine-scale variations is considered.

Further, for the stability of the formulation $\overline{\mathcal{S}}$ and $\mathcal{S}'$ need to be linearly independent and so must $\overline{\mathcal{V}}$ and $\mathcal{V}'$. The uniqueness of the function space decomposition should be explicitly enforced in the numerical procedure adopted, as will be done in Section (3.3), through the selection of appropriate trial function space and weighting function space. Our aim is to derive an expression for u', the 'unresolved' scale, and use this expression to eliminate u' from the weak formulation (3.7), and then solve for $\overline{u}$ using traditional numerical schemes. This procedure is shown below in the abstract notation:

$$a(\overline{w}+w',\overline{u}+u') = (\overline{w}+w',f) \tag{3.11}$$

Using standard arguments for linearly independent $\overline{w}$ and w', Equation (3.11) can be decoupled as,

$$a(\overline{w},\overline{u}) + a(\overline{w},u') = (\overline{w},f) \tag{3.12a}$$

$$a(w',\overline{u}) + a(w',u') = (w',f) \tag{3.12b}$$

One may solve Equation (3.12b) exactly to obtain an analytical relation between u' and $\overline{u}$ as demonstrated in *Hughes et al.* (1998) using a Green's function approach, but this is only possible for very simple boundary-value problems. For more general problems of practical interest, as shown in Section 3.4, we will have to solve it numerically and obtain an approximate representation of u' in terms of $\overline{u}$. However, once this is accomplished, it should be clear that we can use this relation to eliminate u' from Equation (3.12a), solve this equation with the numerical scheme of choice to obtain the coarse-scale, $\overline{u}$, and use this field to recover the 'unresolved' fine-scale, u', and thus obtain the complete solution field u.

The presentation of the variational multiscale framework in this section is intentionally abstract to preserve the generality; the arguments and details of some steps above will be significantly problem dependent. Now a detailed presentation of this framework for the crack propagation problem follows, starting with the physical motivation.

3.2 Cracks as Subgrid Scales: Motivation and Challenges

Physically, crack propagation is a process of configurational change by which new surfaces are created. The creation of new surfaces is governed by surface laws, different from the constitutive laws of the continuum. Classically, this process of surface creation is handled by affecting changes in the numerical discretization, involving incremental grid refinement and remeshing. However, changing the grid to reflect the evolving domain boundaries is computationally very expensive. Instead, an alternative view of cracks as displacement discontinuities in the continuum domain is considered here. The concept of discontinuous displacement fields and the resulting singular strains finds its mathematical treatment in the work of *Temam and Strang* (1980) on BD(Ω), the space of bounded deformations for which all components of the strain are bounded measures. This idea was used to develop a numerical framework for the problem of strong discontinuities due to strain localization by *Simo et al.* (1993), *Simo and Oliver* (1994) and *Armero and Garikipati* (1996). The physical process of strain localization involves localized changes in the continuum constitutive response and no new boundaries and surface laws appear, but its numerical treatment introduced the use of the distributional framework and discontinuous basis functions, which was adopted in *Garikipati* (2002) for embedding micromechanical surface laws into a macroscopic continuum formulation, albeit in a multiscale setting. The presentation in this work follows and extends these multiscale arguments specifically for numerical representation and evolution of cohesive cracks.

As shown in Figure (3.3), a crack opening can be mathematically represented by a discontinuous displacement field over an uncracked body. It is not difficult to see

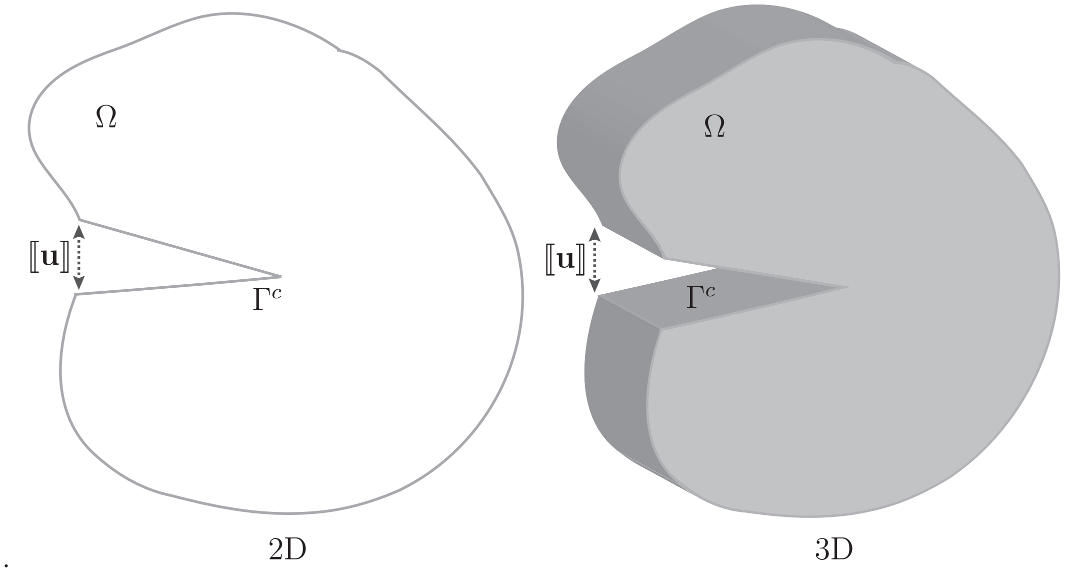

Figure 3.3: *Representation of crack as a displacement discontinuity.* $[\![\mathbf{u}]\!]$ *is the magnitude of the displacement discontinuity which physically represents the magnitude of the crack opening and* Γ^c *is the crack surface.*

that this is rigorous and general enough to represent all possible crack geometries in both two and three dimensional solids. However, the following numerical challenges persist:

- Numerical representation of displacement discontinuities using smooth basis approximations introduce an artificial numerical length scale, as shown in Section (4.1.1), and thus lead to a mesh subjective scheme. On the other hand, usage of discontinuous basis leads to singular strains.
- Topologically, crack surfaces are zero measure sets in the domain volume. Thus stand alone representations of them would require zero volume mesh elements, i.e. interface elements.

In this work, a discontinuous basis is adopted and the necessary distributional arguments will follow. The use of zero volume elements (interface elements, standard cohesive zone elements, etc.) renders the scheme subjective to the numerical discretization, hence is not considered. Instead a variational multiscale setting is introduced where the crack, represented by a displacement discontinuity, is seen as a subgrid fine scale discontinuous field superposed on a coarse scale field.

3.3 Multiscale Formulation of Discontinuous Displacement

The weak formulation of the quasi-static elasticity is the point of departure for the multiscale development. Also, the scope of the presentation is limited to the infinitesimal strain theory of elasticity. Starting with the weak form: For $\mathcal{S} \subset BD(\Omega)$ and $\mathcal{V} \subset H^1(\Omega)$, find $\mathbf{u} \in \mathcal{S} = \{\mathbf{v}|\mathbf{v} = \mathbf{g} \text{ on } \Gamma_g\}$, such that $\forall\ \mathbf{w} \in \mathcal{V} = \{\mathbf{v}|\mathbf{v} = 0 \text{ on } \Gamma_g\}$,

$$\int\limits_{\Omega} \nabla\mathbf{w} : \boldsymbol{\sigma}\ dV = \int\limits_{\Omega} \mathbf{w}\ \mathbf{f}\ dV + \int\limits_{\Gamma_h} \mathbf{w}\ \mathbf{T}\ dS \tag{3.13}$$

where $\mathbf{f}$ is the body force, $\mathbf{g}$ and $\mathbf{T}$ are the prescribed boundary displacement and surface traction, respectively. $\boldsymbol{\sigma}$ is the (Cauchy) stress tensor given by $\boldsymbol{\sigma} = \mathbf{C} : \mathrm{sym}(\nabla\mathbf{u})$, where $\mathbf{C}$ is the fourth-order elasticity tensor.

REMARK 1: As stated in the motivation above, we choose to represent cracks as displacement discontinuities, which means $\mathbf{u} \notin C^0$. This results in the strain being a singular distribution which has a bounded measure, since $\mathbf{u} \in BD(\Omega)$. However the stress should not be a singular distribution as required by the classical jump condition on the traction ($[\![\boldsymbol{\sigma} \cdot \mathbf{n}]\!] = 0$) [2]. This requirement on the stress field is enforced by the material constitutive response which 'mollifies' the singular strains to yield regular stresses.

REMARK 2: In $\mathbb{R}^1$, it is much simpler to present the strain field argument, as $\mathbf{u}$ is

---

[2] If both $\boldsymbol{\varepsilon}$ and $\boldsymbol{\sigma}$ are singular distributions, then the work expression ($\int \boldsymbol{\sigma} : \boldsymbol{\varepsilon}\ dV$) would be a product of distributions, and thus mathematically and physically undefined.

at most a discontinuity and sym($\nabla \mathbf{u}$) is a Dirac-delta function (a bounded measure), $\int_{-\infty}^{\infty} \delta(x)\ dx = 1$. It is interesting to note that in $\mathbb{R}^1$, $\mathbf{u} \in BV(\Omega)$ (space of bounded variations), and $BD(\Omega)$ coincides with $BV(\Omega)$. A discussion of $BD(\Omega)$ space is beyond the scope of this work and interested readers are referred to *Temam and Strang* (1980) for the mathematical development, and to *Suquet* (1981) for the treatment of discontinuities in plasticity which have similar kinematics to that in crack propagation.

Now, following the subgrid scale model presented in Section 3.1.2, scale decompositions of $\mathbf{u}$ and $\mathbf{w}$ are introduced. The decompositions are qualified by requiring that the fine scales, $\mathbf{u}'$ and $\mathbf{w}'$, vanish outside the neighborhood of the crack path, which is contained in Ω' (Figure 3.4), referred to as the microstructural or fine-scale subdomain

$$\mathbf{u} = \underbrace{\overline{\mathbf{u}}}_{\text{coarse scale}} + \underbrace{\mathbf{u}'}_{\text{fine scale}} \tag{3.14a}$$

$$\mathbf{w} = \underbrace{\overline{\mathbf{w}}}_{\text{coarse scale}} + \underbrace{\mathbf{w}'}_{\text{fine scale}} \tag{3.14b}$$

$$\overline{\mathbf{u}} \in \overline{\mathcal{S}} = \{\mathbf{v} |\ \mathbf{v} = \mathbf{g} \text{ on } \Gamma_g\} \tag{3.14c}$$

$$\overline{\mathbf{w}} \in \overline{\mathcal{V}} = \{\mathbf{v} |\ \mathbf{v} = 0 \text{ on } \Gamma_g\} \tag{3.14d}$$

$$\mathbf{u}' \in \mathcal{S}' = \{\mathbf{v} |\ \mathbf{v} = 0 \text{ on } \Omega \backslash \text{int}(\Omega')\} \tag{3.14e}$$

$$\mathbf{w}' \in \mathcal{V}' = \{\mathbf{v} |\ \mathbf{v} = 0 \text{ on } \Omega \backslash \text{int}(\Omega')\} \tag{3.14f}$$

where $\mathcal{S} = \overline{\mathcal{S}} \oplus \mathcal{S}'$ and $\mathcal{V} = \overline{\mathcal{V}} \oplus \mathcal{V}'$. Further, $\overline{\mathcal{V}}$ and $\mathcal{V}'$ are chosen to be linearly independent.

Given the scale decomposition of $\mathbf{u}$ and $\mathbf{w}$, we can be split Equation (3.13) into two

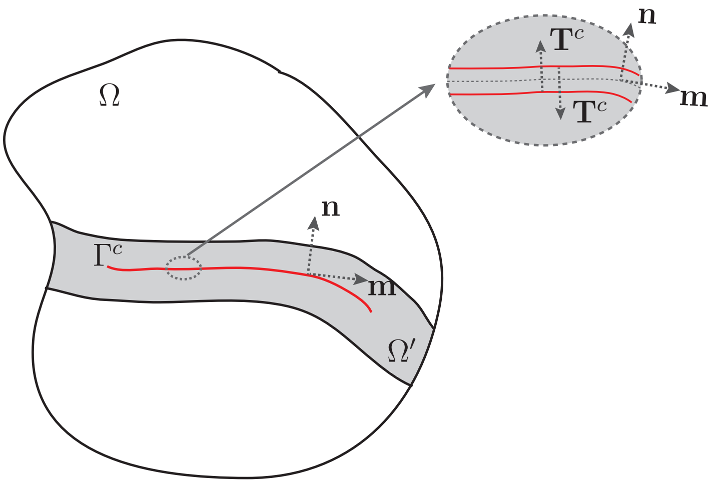

Figure 3.4: *The microstructural domain, Ω', and the crack surface, Γ^c. Shown in the inset are the crack orientation vectors and the crack surface traction.*

separate weak forms,

$$\int_{\Omega} \nabla \overline{\mathbf{w}} : \boldsymbol{\sigma} \; dV = \int_{\Omega} \overline{\mathbf{w}} \; \mathbf{f} \; dV + \int_{\Gamma_h} \overline{\mathbf{w}} \; \mathbf{T} \; dS \qquad (\overline{\mathrm{W}}) \tag{3.15a}$$

$$\int_{\Omega'} \nabla \mathbf{w}' : \boldsymbol{\sigma} \; dV = \int_{\Omega'} \mathbf{w}' \; \mathbf{f} \; dV + \int_{\Gamma'_h} \mathbf{w}' \; \mathbf{T} \; dS \tag{3.15b}$$

Now consider a crack surface, Γ^c, in the fine-scale subdomain (Figure 3.4). Assuming no body force in the fine-scale subdomain, using integration by parts and standard variational arguments, Equation (3.15b) can be reduced to,

$$\int_{\Gamma^c} \mathbf{w}' \; \boldsymbol{\sigma} \cdot \mathbf{n} \; dS = \int_{\Gamma^c} \mathbf{w}' \; \mathbf{T}^c \; dS \qquad (\mathrm{W}') \tag{3.16}$$

where $\mathbf{T}^c$ is the external traction on the crack faces. In the subsequent sections, $(\overline{\mathrm{W}})$ and (W') are referred to as the coarse scale and fine scale weak forms, respectively.

3.4 Fine-Scale Field and Micromechanics Embedding

(W$'$) allows us to embed any traction based cohesive surface-law, $\mathbf{T}^c$, into the continuum formulation. Writing the traction on Γ^c in terms of the components T_n^c and T_m^c along $\mathbf{n}$ and $\mathbf{m}$ respectively,

$$\mathbf{T}^c = T_n^c \mathbf{n} + T_m^c \mathbf{m} \tag{3.17}$$

The fine scale field, $\mathbf{u}'$, for crack problems is composed of a displacement discontinuity , $[\![\mathbf{u}]\!]$, which can be expressed in terms of the components $[\![u_n]\!]$ and $[\![u_m]\!]$ along $\mathbf{n}$ and $\mathbf{m}$ respectively,

$$[\![\mathbf{u}]\!] = \underbrace{[\![u_n]\!]}_{\text{opening}} \mathbf{n} + \underbrace{[\![u_m]\!]}_{\text{shear}} \mathbf{m} \tag{3.18}$$

$[\![u_n]\!]$ and $[\![u_m]\!]$ are referred to as the *crack face opening displacement* and *crack face shear displacement*, respectively. Similarly, the crack face opening mode is referred to as Mode-I and crack face shear mode is referred to as Mode-II.

In this presentation, we consider simple micromechanical surface traction laws given by:

$$T_n^c = T_{n_0}^c - \mathcal{H}_n [\![u_n]\!] \tag{3.19a}$$

$$T_m^c = T_{m_0}^c - \mathcal{H}_m [\![u_m]\!] \tag{3.19b}$$

where $T_{n_0}^c$ and $\mathcal{H}_n$ are the Mode-I critical opening traction and Mode-I softening modulus, and $T_{m_0}^c$ and $\mathcal{H}_m$ are the Mode-II critical shear traction and Mode-II softening modulus. Using Equations (3.17) and (3.19), $\mathbf{u}'$ (characterized by $[\![\mathbf{u}]\!]$) can be eliminated from $(\overline{\mathrm{W}})$, which can then be solved for $\overline{\mathbf{u}}$. Once $\overline{\mathbf{u}}$ is obtained it can be used to recover $\mathbf{u}'$, thereby determining the complete displacement field. Developing this procedure in a finite element setting is the focus of the next chapter.

3.5 Closing Remarks

In this chapter, the necessary multiscale background was introduced, and its application to crack problems was discussed. The approach consists of treating the discontinuous displacement field in crack problems in a distributional sense, and identifying the singular character of the strains. This treatment was then developed to obtain the weak formulation of the coarse-scale and fine-scale problems. Then it was shown that the fine-scale problem can be used as a vehicle to embed the cohesive surface laws into the continuum formulation. Using this as a point of departure, the necessary numerical framework is developed in the subsequent chapter.

CHAPTER IV

Finite Element Implementation

With the multiscale concepts laid out, and explicit weak form expression derived, we now turn our attention to the numerical implementation. In this Chapter, the multiscale methodology is cast into a finite element formulation and the necessary numerical framework, referred to as the Variational Multiscale Cohesive Method (VMCM), is developed. First, a brief discussion of the limitations of standard finite element basis functions is presented in Section (4.1). Then the necessary discontinuous shape functions are presented in Section (4.2). These enhanced basis functions were first introduced in the works of *Simo et al.* (1993), *Armero and Garikipati* (1996) and *Garikipati* (1996). Comparable, but significantly different, discontinuous basis functions are used in the Extended Finite Element (XFEM) method introduced in *Moes et al.* (1999) and applied to cohesive crack propagation in *Moes and Belytschko* (2002), and in the related partition of unity method based basis functions employed in *Wells and Sluys* (2001). After the multiscale shape function discussion, the finite dimensional weak formulation is presented in Section (4.3) and followed by the iterative solution procedure in Section (4.4). Lastly, in Section (4.5), the closing remarks and a brief comparison of the present multiscale framework with the Partition of Unity Methods (PUM) is presented.

Figure 4.1: *Schematic of displacement field in a domain containing strong and weak discontinuities. w is the width of the diffused band.*

4.1 Mesh Sensitivity of Standard Galerkin Basis

Classical Galerkin formulations for elasticity require that the basis/shape functions have sufficient smoothness (at least C^0) as the weak form involves gradients of the displacement. C^0 functions are sufficient to resolve the displacement field in the elastic or hardening-plastic regime. However, in the presence of softening behavior, deformation fields tend to localize, leading to high displacement gradients in localized regions of the domain. Broadly, this phenomenon is referred to as either a weak discontinuity for diffused localization or a strong discontinuity for singular localization as shown in Figure (4.1). In both cases, using standard basis functions invariably lead to mesh subjective schemes. This lack of mesh objectivity is widely documented in the literature, often in the context of strain localization phenomena that involve softening. Cracks, which are the focus of this work, have identical kinematics to the strong discontinuity phenomenon. However, unlike strain localization problems, the constitutive response is based on traction-separation (force-displacement) relations rather than stress-strain relations. Considering this difference, a brief discussion of mesh sensitivity in the context of crack propagation simulations is now presented.

4.1.1 Pathological Mesh Dependence of Strain Localization in Softening Materials

Consider a 1D problem of an elastic bar under tensile loading, with an elastic modulus, E, a critical cohesive traction, T^c_{crit}, and a cohesive softening modulus, $\mathcal{H}$.

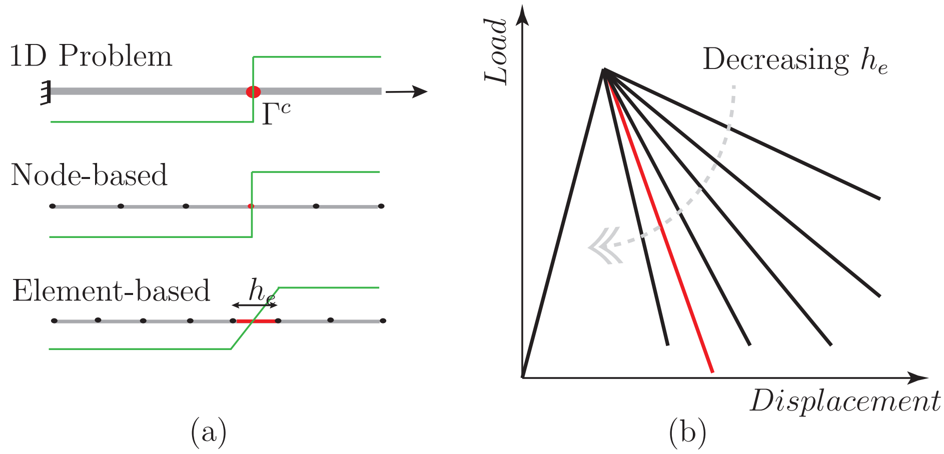

Figure 4.2: *Performance of standard Galerkin basis. (a) Comparison of the physically expected displacement field with the displacement field obtained by node-based and element-based numerical schemes. In each case, the crack location is marked red and the green lines are the displacement fields. (b) Comparison of the expected and numerically obtained load displacement responses. The red line represents the softening path of the node-based scheme, which for a simple 1D problem is equal to the analytically expected path. The other softening paths correspond to the element-based scheme for different values of the element length.*

As the bar is loaded, the traction at some point, say Γ^c, reaches T^c_{crit} and cohesive softening occurs at that point. Clearly, there are at least two traditional methods to handle this problem in the classical Galerkin finite element framework:

- *Node-Based*: If the point Γ^c is known a priori, then one can ensure a node pair placement at that point, and when T^c equals T^c_{crit}, have the local nodal forces evolve according to the given cohesive softening modulus. This is the idea behind the widely used cohesive zone methods [*Pietruszczak and Mroz* (1981); *Ungsuwarungsri and Knauss* (1987); *Song and Waas* (1993); *Schellekens and DeBorst* (1993); *Xu and Needleman* (1994); *Camacho and Ortiz* (1996)]. An extension of this idea, when Γ^c is not known beforehand, is to identify it as part of the solution process and then employ re-meshing to create node pairs on Γ^c.

- *Element-Based*: The requirement of Γ^c being a nodal point is relaxed, and instead the elemental volume, say Ω^c_e, which contains this point is considered. Upon reaching $T^c = T^c_{crit}$, the constitutive response of this element is modified to produce a diffused softening response which produces the expected global load displacement response. This is the gist of the crack band model by *Bazant and Oh* (1983).

These schemes and the 1D problem are depicted in Figure (4.2a) and the corresponding global load displacement responses are shown in Figure (4.2b). However, both the above methods have several limitations. The node based approach is not viable, as in problems of practical interest, Γ^c is not known beforehand and re-meshing is prohibitively expensive. The element based schemes suffer from pathological mesh dependence which is demonstrated below in the context of the 1D problem.

Let the elastic bar be discretized into linear elements, each of length h_e. Considering only the post-cracking load steps, let the crack surface, Γ^c, be contained within an element Ω_e^c. Now the modified constitutive modulus is given by

$$E_m(x) = \begin{cases} E : x \in \Omega \backslash \Omega_e^c \\ f(E, \mathcal{H}) : x \in \Omega_e^c \end{cases} \tag{4.1}$$

where $f(E, \mathcal{H}) < 0$ and hence there is energy dissipation in Ω_e^c, given by $D = \int_{\Omega_e^c} \boldsymbol{\sigma} : \dot{\boldsymbol{\varepsilon}}^p \, dV$, and is graphically given by the area under the curves shown in Figure (4.2b). Assuming the bar to be of uniform cross-section, dissipated energy is linearly proportional to the element length. This implies, as $h_e \to 0$, there is no dissipation and the bar unloads elastically. Thus the energy dissipation and global load displacement response have a pathological mesh dependence. This dependence can be fixed, at least in 1D, by introducing a regularization or localization limiter, such as a characteristic length [*Bazant and Cedolin* (2003)]. For 2D and 3D problems with unstructured meshes and non-straight crack paths these schemes are more complex. Further the basic constitutive behavior of cracks is not fully represented, as the surface-based

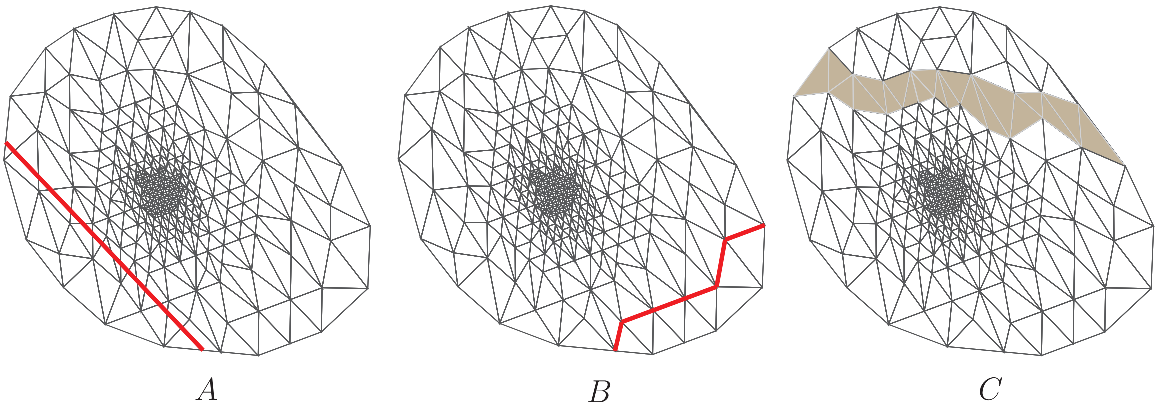

Figure 4.3: *Comparison of representative crack paths observed using traditional crack propagation schemes. (A) Physically observed crack paths which are well resolved surfaces not particularly associated with any mesh features, (B) Crack paths restricted to element edges for node-based schemes, (C) Crack paths smeared over a finite volume for element-based schemes.*

traction-separation constitutive model associated with cracks is now replaced by a volume-based stress-strain model, with modulus given by Equation (4.1).

4.1.2 Discretization Sensitivity of Crack Paths

Apart from the pathological mesh dependence of the global load-displacement and energy-dissipation response, the numerical discretization also limits the crack path and its resolvability in the traditional schemes discussed above. Consider Figure (4.3) which compares the physically expected crack path with that obtained by using a node-based or element-based scheme. Since cracks are driven by the local stress state and/or non-local energetics, ideally the propagation path should be nearly independent of the domain discretization. However, the very construction of these methods limits unbiased crack propagation. In case of node-based schemes the crack path coincides with the element edges, so the crack path is locally limited by discrete edge directions. In unstructured 2D/3D meshes this may lead to deviation from the physically expected path, rendering the boundary value problem to be solved, erroneous. For element-based schemes, though there is no mesh restriction on the crack path, the numerical resolution of the crack path is poor.

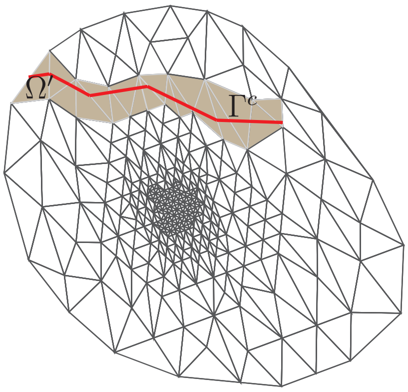

Figure 4.4: *Schematic of the crack path and fine-scale domain, Ω', representation in the VMCM implementation.*

With this review of the limitations of traditional numerical crack propagation schemes, attention is now focused on the development of a numerical framework for the multiscale formulation presented in Chapter III. The discussion in the following sections of this Chapter and the simulation results presented in Chapter V will demonstrate that the multiscale scheme circumvents the above limitations and results in mesh objective formulation for crack propagation, which schematically is represented in Figure (4.4).

4.2 Multiscale Element Construction

The reparametrization of the fine scale discontinuous displacement field, $\mathbf{u}'$, and the development of discontinuous shape functions follows the presentation in *Armero and Garikipati* (1996) and *Garikipati* (1996).

4.2.1 Shape Functions

We begin with the expression for the fine scale displacement field,

$$\mathbf{u}' = M_{\Gamma^c} \, [\![\mathbf{u}]\!] \, , \qquad \text{where } M_{\Gamma^c} = N - H_{\Gamma^c} \tag{4.2}$$

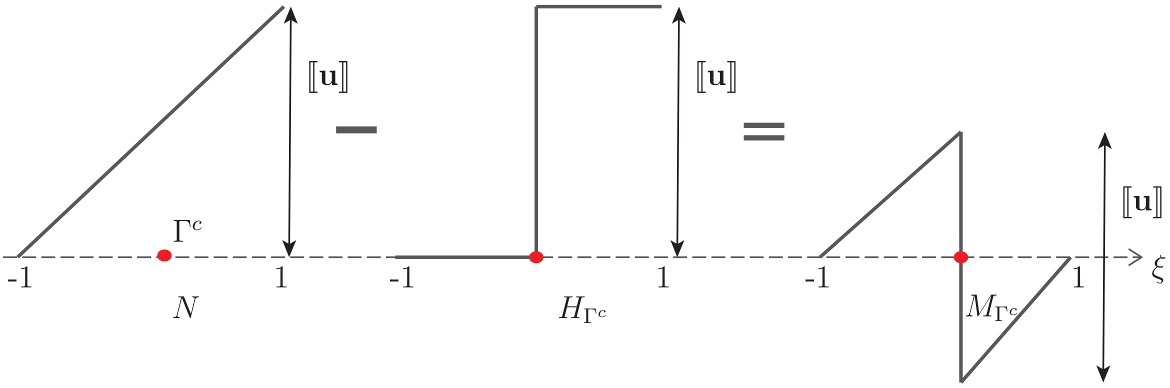

Figure 4.5: *Construction of the discontinuous multiscale shape function in 1D.*

where N is a continuous basis function defined on Ω' and H_{Γ^c} is a Heaviside function which has its discontinuity on Γ^c. Thus, M_{Γ^c} is a composite shape function constructed by superposing a Heaviside function on a linear shape function, ensuring that $M_{\Gamma^c} = 0$ on $\Omega \backslash \text{int}(\Omega')$. This construction is depicted in Figure (4.5) for 1D and Figure (4.6) for 2D. A detailed construction is now presented for the constant strain triangle element.

As shown in Figure (4.6), there are two possible constructions for triangle elements depending on the relative orientation of the normal to the crack path, $\mathbf{n}$, with respect to the outward normal of the edge not intersected by the crack, $\mathbf{n}^i$ (shown in Figure (4.7)). For each of these cases, N, H_{Γ^c} and ∇M_{Γ^c} are given by

Case-I: $\mathbf{n}.\mathbf{n}^i < 0$ (Figure (4.6a))

$$N(x) = 1 - \frac{x - x^i}{h^i}.\mathbf{n}^i \tag{4.3}$$

$$H_{\Gamma^c}(x) = \begin{cases} 0 : |(x - x^\Gamma).\mathbf{n}| \leq 0 \\ 1 : |(x - x^\Gamma).\mathbf{n}| > 0 \end{cases} \tag{4.4}$$

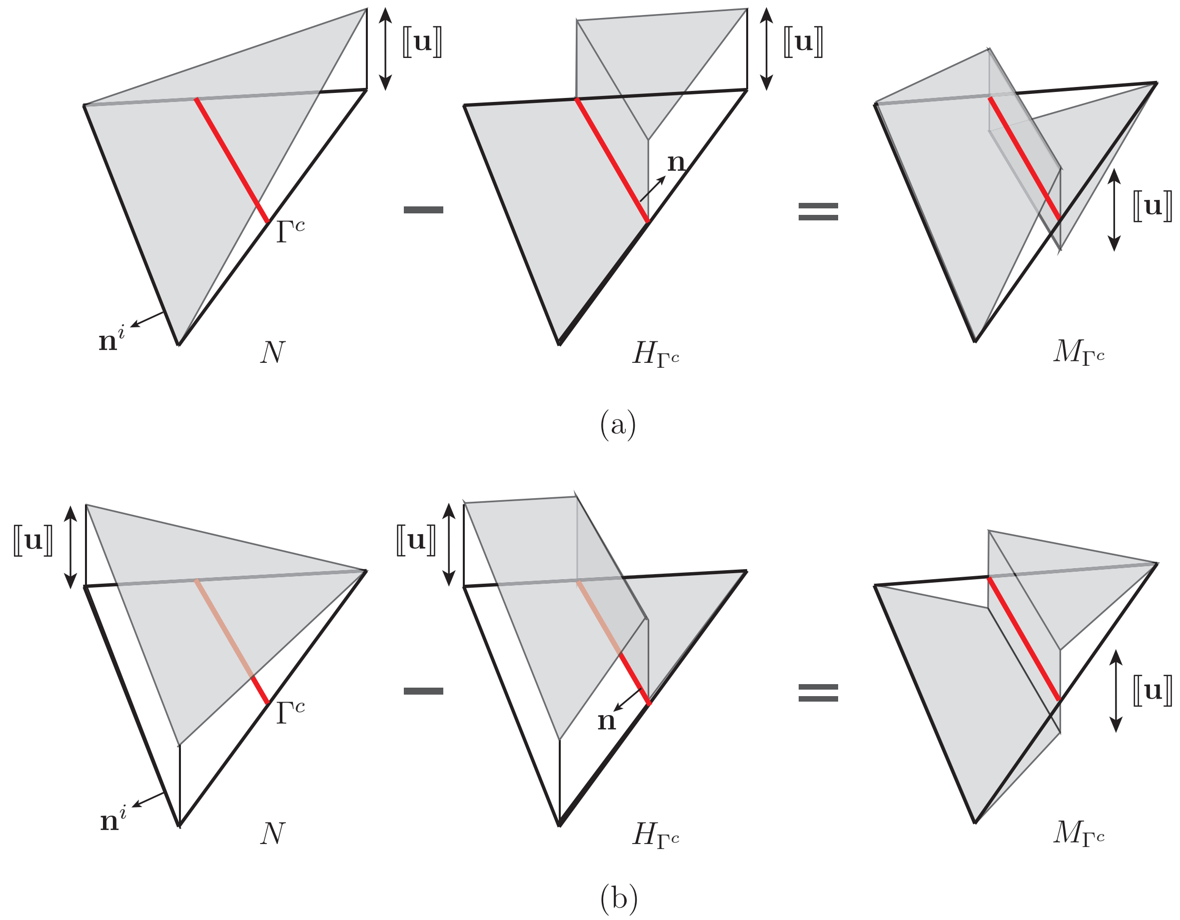

Figure 4.6: *Possible constructions of the discontinuous multiscale shape function in 2D.* $\mathbf{n}$ *is the normal to the crack path, in the direction of the desired jump in displacement.*

$$\nabla M_{\Gamma^c}(x) = -\frac{\mathbf{n}^i}{h^i} - \delta_{\Gamma^c}\ \mathbf{n} \tag{4.5}$$

Case-II: $\mathbf{n}.\mathbf{n}^i \geq 0$ (Figure (4.6b))

$$N(x) = \frac{x - x^i}{h^i}.\mathbf{n}^i \tag{4.6}$$

$$H_{\Gamma^c}(x) = \begin{cases} 0 : |(x - x^\Gamma).\mathbf{n}| \leq 0 \\ 1 : |(x - x^\Gamma).\mathbf{n}| > 0 \end{cases} \tag{4.7}$$

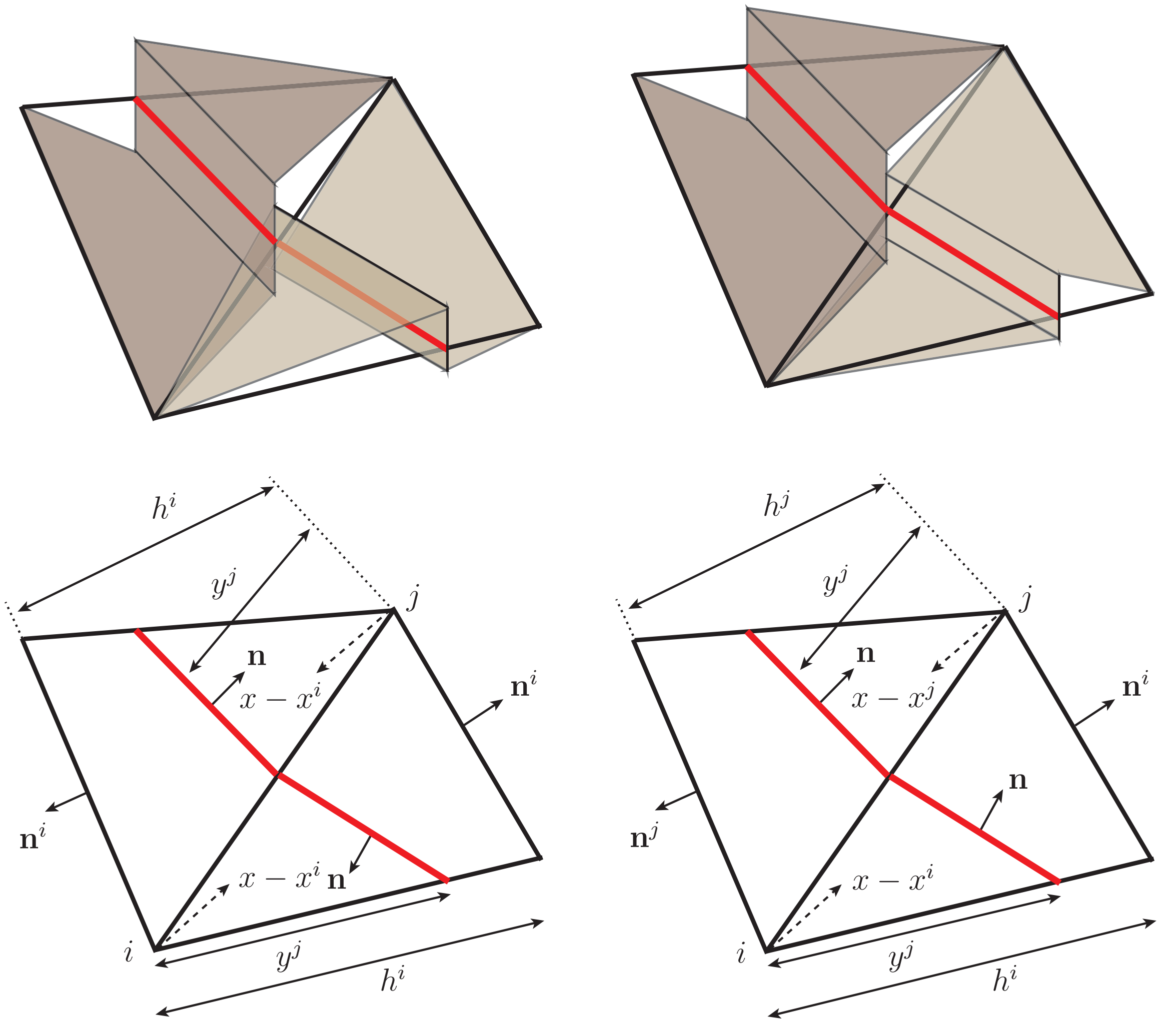

(a) (b)

Figure 4.7: *Orientation of the normal to crack path,* $\mathbf{n}$, *with respect to the orientation of the element.*

$$\nabla M_{\Gamma^c}(x) = \frac{\mathbf{n}^i}{h^i} - \delta_{\Gamma^c}\ \mathbf{n} \tag{4.8}$$

As can be seen from the above description, the multiscale shape function construction is more involved than traditional shape functions. In a numerical implementation, only ∇M_{Γ^c} enters the system of equations through the expression for $\nabla \mathbf{u}'$, which in matrix form is given by

$$\nabla \mathbf{u}' = \nabla M_{\Gamma^c}\ [\![\mathbf{u}]\!] \tag{4.9}$$

where,

$$[\![\mathbf{u}]\!] = \begin{bmatrix} [\![\mathbf{u}]\!]_x \\ [\![\mathbf{u}]\!]_y \end{bmatrix}$$

$$\nabla M_{\Gamma^c} = \underbrace{\frac{1}{h^i} \begin{bmatrix} \mathbf{n}_x^i & 0 \\ 0 & \mathbf{n}_y^i \\ \mathbf{n}_y^i & \mathbf{n}_x^i \end{bmatrix}}_{G} - \delta_{\Gamma^c} \underbrace{\begin{bmatrix} \mathbf{n}_x & 0 \\ 0 & \mathbf{n}_y \\ \mathbf{n}_y & \mathbf{n}_x \end{bmatrix}}_{H}$$

G and H are the matrix representation of $\mathbf{n}^i$ and $\mathbf{n}$, respectively.

4.2.2 Numerical Quadrature

The weak form of the coarse scale and fine scale problems, given by Equations (3.15a) and (3.16), respectively, involve different domains of integration. The coarse scale weak form, taken element wise, is a volume integral over the elemental volume and thus the quadrature rules used to evaluate the integral is the conventional triangle quadrature scheme. However, the fine scale weak form, taken element wise, is a surface integral over the crack path, and needs special attention.

Consider Figure (4.8), which depicts a constant $[\![\mathbf{u}]\!]$ in linear triangles and linear variation of $[\![\mathbf{u}]\!]$ in higher order triangles. Depending on the order of the variation of $[\![\mathbf{u}]\!]$, which affects the order of variation of stress, the appropriate order of quadrature should be chosen. In 2D, since the crack path is a line, gauss quadrature schemes are optimal, and therefore an n point scheme can be chosen to capture stress variations upto order 2n. The possible 1-point and 2-point crack path integration points along with the regular coarse scale field integration points are shown in Figure (4.9).

REMARK: Higher order variations of $[\![\mathbf{u}]\!]$ along Γ are possible, but may not be necessary to capture the physical crack opening unless the meshes are very coarse. The numerical simulation results presented in the following chapters considered only constant distribution and the crack opening was well represented. For this case, since the stress is also constant over linear triangle elements, a one point quadrature rule is sufficient. This reduces Equation (3.16) to $\boldsymbol{\sigma} \cdot \mathbf{n} = T^c$ which can be evaluated at any point along the crack path within the element.

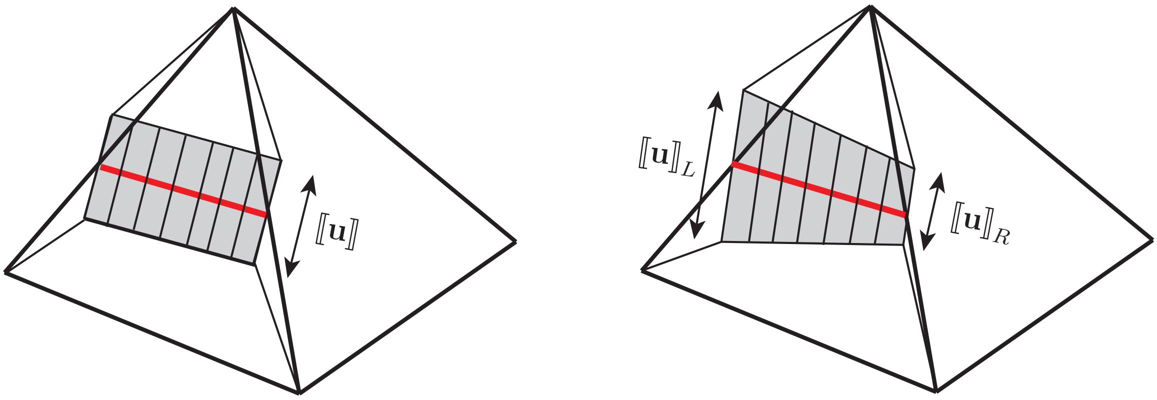

Figure 4.8: *Elemenal values of the displacement discontinuity, $[\![\mathbf{u}]\!]$, which physically represents the crack opening. (a) Constant $[\![\mathbf{u}]\!]$ in each element, (b) Linearly varying $[\![\mathbf{u}]\!]$ with $[\![\mathbf{u}]\!]_L$ on the left edge and $[\![\mathbf{u}]\!]_R$ on the right edge, leading to inter-element continuity along Γ.*

4.3 Finite Dimensional Weak Forms and Discretized Equations

In the finite dimensional setting, the problem domain is divided into non overlapping elements such that $\Omega = \bigcup_1^{nel} \Omega_e^h$, where nel is the number of elements. In this presentation linear triangle elements are considered, and thus the integration scheme depicted in Figure (4.9a) will be sufficient. Introducing the approximate interpola-

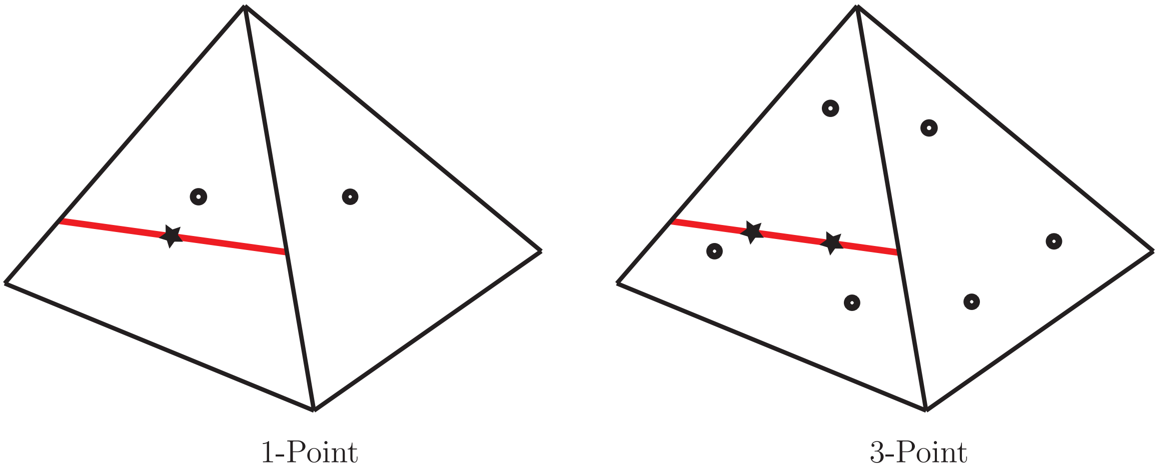

Figure 4.9: *Some of the possible quadrature rules for coarse-scale and fine-scale problems over triangle elements. (a) Linear Triangle: 1-point scheme for coarse-scale field and 1-point for the fine-scale field. (a) Higher Order Triangle: 3-point scheme for coarse-scale field and 2-point for the fine-scale field.*

tions to the coarse-scale displacement and variation,

$$\overline{\mathbf{u}}_e^h(\xi,\eta) = \sum_{A=1}^{3} N^A(\xi,\eta) d^A \tag{4.10a}$$

$$\overline{\mathbf{w}}_e^h(\xi,\eta) = \sum_{A=1}^{3} N^A(\xi,\eta) c_e^A \tag{4.10b}$$

where $(\xi,\, \eta)$ are the iso-parametric coordinates, d^A and c_e^A are the nodal values of the finite dimensional coarse-scale displacement, $\overline{\mathbf{u}}^h$, and finite dimensional coarse-scale variation, $\overline{\mathbf{w}}^h$, respectively. $N^A(\xi,\eta)$ is the Lagrangian shape function at node A with the usual compact support, $N^A(\xi_B,\eta_B) = \delta_B^A$. Adopting matrix notation,

$$\overline{\mathbf{u}} = N\mathbf{d} \qquad \text{and} \qquad \overline{\mathbf{w}} = N\mathbf{c} \tag{4.11}$$

$$\nabla\overline{\mathbf{u}} = \mathbf{Bd} \qquad \text{and} \qquad \nabla\overline{\mathbf{w}} = \mathbf{Bc} \tag{4.12}$$

where $\mathbf{B}$ is the standard matrix form of the shape function gradients. Similarly, the expressions for strain and stress are

$$\boldsymbol{\varepsilon} = \mathbf{Bd} + (\mathbf{G} - \delta_{\Gamma^c}\mathbf{H})\, [\![\mathbf{u}]\!] \tag{4.13a}$$

$$\boldsymbol{\sigma} = \mathbb{C} : (\mathbf{Bd} + \mathbf{G}\, [\![\mathbf{u}]\!]) \tag{4.13b}$$

Substituting the above expressions into Equations (3.15a) and (3.16), the respective finite dimensional equations are given by

$$\int\limits_{\Omega} \mathbf{B}^T\mathbb{C} : (\mathbf{Bd} + \mathbf{G}\, [\![\mathbf{u}]\!])\; dV = \int\limits_{\Omega} Nf\; dV + \int\limits_{\Gamma_h} N\; T\; dS \tag{4.14a}$$

$$\mathbf{H}^T\mathbb{C} : (\mathbf{Bd} + \mathbf{G}\, [\![\mathbf{u}]\!]) = \mathbf{T^c} \tag{4.14b}$$

where the fine-scale weak form is reduced to $\boldsymbol{\sigma} \cdot \mathbf{n} = T^c$, as for linear triangles both $\boldsymbol{\sigma}$ and $[\![\mathbf{u}]\!]$ (and hence $\mathbf{T^c}$) are constant over the element. To suit an iterative solution procedure, the above equations are expressed as coarse-scale and fine-scale residuals,

$$\bar{\mathbf{r}} = \int\limits_{\Omega} \mathbf{B}^T\mathbb{C} : (\mathbf{Bd} + \mathbf{G}\, [\![\mathbf{u}]\!])\; dV - \int\limits_{\Omega} Nf\; dV - \int\limits_{\Gamma_h} N\; T\; dS \tag{4.15a}$$

$$\mathbf{r}' = \mathbf{H}^T\mathbb{C} : (\mathbf{Bd} + \mathbf{G}\, [\![\mathbf{u}]\!]) - \mathbf{T^c} \tag{4.15b}$$

Linearizing the above residuals about $\mathbf{d}$ and $[\![\mathbf{u}]\!]$ and rearranging terms, we obtain the following system of equations in $(\delta\mathbf{d},\ \delta[\![\mathbf{u}]\!])$,

$$\begin{bmatrix} \mathbf{K_{\bar{u}\bar{u}}} & \mathbf{K_{\bar{u}u'}} \\ \mathbf{K_{u'\bar{u}}} & \mathbf{K_{u'u'}} \end{bmatrix} \begin{bmatrix} \delta\mathbf{d} \\ \delta[\![\mathbf{u}]\!] \end{bmatrix} = \begin{bmatrix} -\bar{\mathbf{r}} \\ -\mathbf{r}' \end{bmatrix} \tag{4.16}$$

where,

$$\mathbf{K}_{\bar{\mathbf{u}}\bar{\mathbf{u}}} = \int\limits_{\Omega} \mathbf{B}^T \mathbb{C} \mathbf{B} \; dV \tag{4.17a}$$

$$\mathbf{K}_{\bar{\mathbf{u}}\mathbf{u}'} = \int\limits_{\Omega} \mathbf{B}^T \mathbb{C} \mathbf{G} \; dV \tag{4.17b}$$

$$\mathbf{K}_{\mathbf{u}'\bar{\mathbf{u}}} = \mathbf{H}^T \mathbb{C} \mathbf{B} \tag{4.17c}$$

$$\mathbf{K}_{\mathbf{u}'\mathbf{u}'} = \mathbf{H}^T \mathbb{C} \mathbf{G} + \mathcal{H}_n \mathbf{n} \otimes \mathbf{n} + \mathcal{H}_m \mathbf{m} \otimes \mathbf{m} \tag{4.17d}$$

4.4 Incremental Solution Procedure

Solution steps of a VMCM implementation are listed below. In addition one would have a crack tracking algorithm to advance the crack tip after each load increment.

```
initial state: $\mathbf{d}_0$, $[\![\mathbf{u}]\!]_0$, $\boldsymbol{\varepsilon}_0$ and $\boldsymbol{\sigma}_0$
loop over load increments:
    current converged state: $\mathbf{d}_{n-1}$, $[\![\mathbf{u}]\!]_{n-1}$, $\boldsymbol{\varepsilon}_{n-1}$ and $\boldsymbol{\sigma}_{n-1}$
    loop over iterations until $\|\mathbf{r}\|_2 <$ tolerance
        current iteration state: $\mathbf{d}^k_{n-1}$, $[\![\mathbf{u}]\!]^k_{n-1}$, $\boldsymbol{\varepsilon}^k_{n-1}$ and $\boldsymbol{\sigma}^k_{n-1}$
        $\delta\mathbf{d}^k_{n-1} = \mathbf{K}^{-1}\mathbf{r}$
        $\mathbf{d}^{k+1}_{n-1} = \mathbf{d}^k_{n-1} + \delta\mathbf{d}^k_{n-1}$
        for each cracked element:
            $\delta[\![\mathbf{u}]\!]^k_{n-1} = \mathbf{K}^{\mathbf{-1}}_{\mathbf{u'u'}}(\mathbf{r'} - \mathbf{K}_{\mathbf{u'\bar{u}}}\delta\mathbf{d}^k_{n-1})$
            $[\![\mathbf{u}]\!]^{k+1}_{n-1} = [\![\mathbf{u}]\!]^k_{n-1} + \delta[\![\mathbf{u}]\!]^k_{n-1}$
            $\delta\boldsymbol{\varepsilon}^{reg}{}^{k}_{n-1} = \mathbf{B}\delta\mathbf{d}^k_{n-1} + \mathbf{G}\ \delta[\![\mathbf{u}]\!]^k_{n-1}$
            $\delta\boldsymbol{\sigma}^k_{n-1} = \mathbb{C} : \delta\boldsymbol{\varepsilon}^{reg}{}^{k}_{n-1}$
            $\boldsymbol{\varepsilon}^{k+1}_{n-1} = \boldsymbol{\varepsilon}^k_{n-1} + \delta\boldsymbol{\varepsilon}^k_{n-1}$
            $\boldsymbol{\sigma}^{k+1}_{n-1} = \boldsymbol{\sigma}^k_{n-1} + \delta\boldsymbol{\sigma}^k_{n-1}$
            $\mathbf{T^c} = \mathbf{T^c_0} - \mathcal{H}_n\mathbf{n}\otimes\mathbf{n} - \mathcal{H}_m\mathbf{m}\otimes\mathbf{m}$
            $\bar{\mathbf{r}} = \int_{\Omega_{el}} \mathbf{B}^T\boldsymbol{\sigma}^{k+1}_{n-1}\ dV - \int_{\Omega_{el}} N\ \mathbf{f}\ dV - \int_{\Gamma_{h_{el}}} N\ \mathbf{T}\ dS$
            $\mathbf{r'} = \mathbf{H}^T\boldsymbol{\sigma}^{k+1}_{n-1} - \mathbf{T^c}$
            static condensation:
                $\mathbf{K}_{el} = \mathbf{K_{\bar{u}\bar{u}}} - \mathbf{K_{\bar{u}u'}}\mathbf{K}^{\mathbf{-1}}_{\mathbf{u'u'}}\mathbf{K_{u'\bar{u}}}$
                $\mathbf{r}_{el} = \bar{\mathbf{r}} - \mathbf{K_{\bar{u}u'}}\mathbf{K}^{\mathbf{-1}}_{\mathbf{u'u'}}\mathbf{r'}$
            Assembly: $\mathbf{K}_{el} \longrightarrow \mathbf{K}$ and $\mathbf{r}_{el} \longrightarrow \mathbf{r}$
    for elements ahead of current crack tip, check for crack growth (Crack Tracking):
        if $\mathbf{n}.\boldsymbol{\sigma}\mathbf{n} \geq T^c_{n_0}$: Mode-I active
        if $\mathbf{m}.\boldsymbol{\sigma}\mathbf{n} \geq T^c_{m_0}$: Mode-II active
        if Mode-I active or Mode-II active: Form elemental $\mathbf{G}$, $\mathbf{H}$ and $\mathbf{Q}$
```

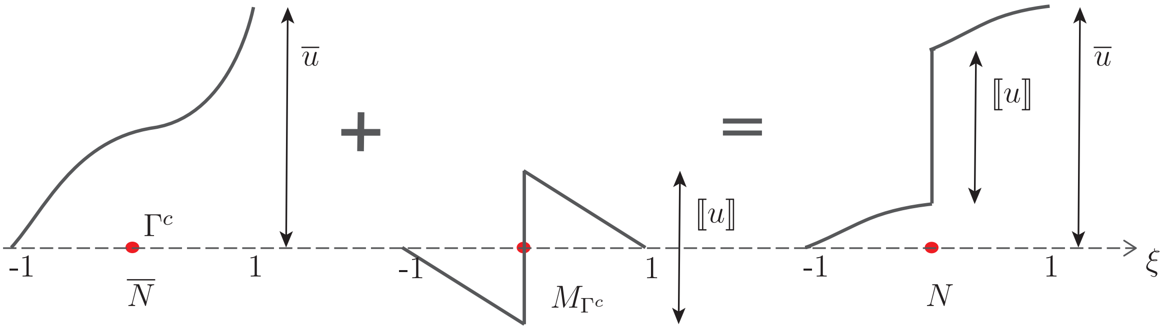

Multiscale

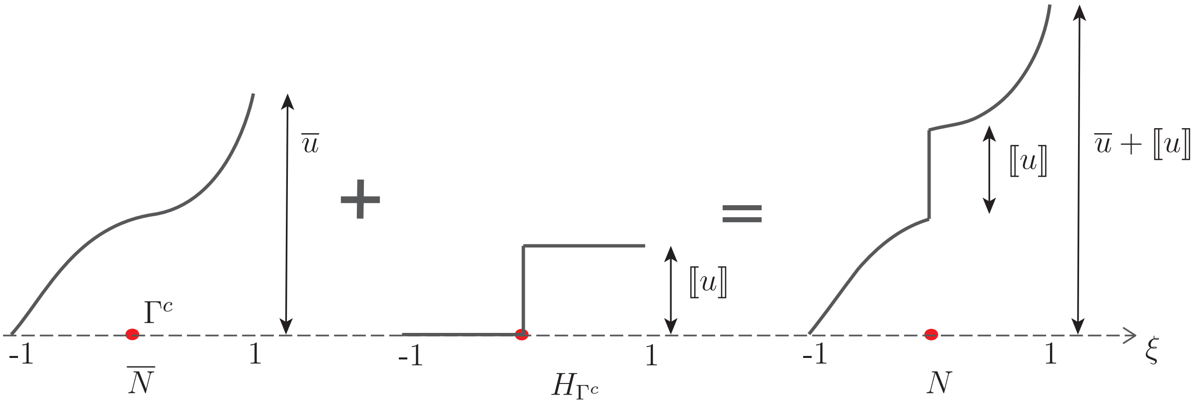

PUM

Figure 4.10: *Comparison of the interpolation schemes used to represent the crack surface in the multiscale approach presented here and the various partition of unity based approaches.*

4.5 Closing Remarks

A finite element framework for the two scale representation of cracks has been presented. This implementation can sharply resolve the discontinuity surface instead of smearing the discontinuity across the element volume, thus avoiding any spurious numerical length scales. Also there is no mesh bias on the crack path, which leads to mesh objective crack propagation and global load-displacement response, both of which will be demonstrated in the simulations in Chapter (V). Further the seamless embedding of cohesive micromechanics within a continuum formulation leads to a physically consistent implementation which is validated by comparison with experimental results in Chapter (VI). The element construction presentation in this chapter has been limited to triangle elements, and can be extended to other 2D and 3D elements. However, for non-simplex elements the construction of the multiscale shape function will be more involved.

For completeness, the distinction between the multiscale interpolation and partition of unity (PUM) interpolation schemes have been depicted in Figure (4.10). As shown here, though both methods represent the displacement discontinuity as a Heaviside function, the advantage of the multiscale approach is the *local-to-element* nature of the fine scale field. From a numerical standpoint this implies that the additional degree of freedom needed to represent $[\![u]\!]$ do not contribute to the global solution vector, due to condensation at elemental level, thus leaving the sparsity pattern of the global problem untouched. In contrast, PUM methods add extra nodal degrees of freedom to represent the enhanced displacement discontinuity modes and thereby increasing the global solution vector size with crack propagation. While a more detailed comparative study of the computational complexity, numerical stability and consistency are a topic for future work, interested readers are pointed to a related study between the strong discontinuity method, from which the multiscale method inherits its interpolation characteristics, and the PUM based extended finite element (X-FEM) method reported by *Oliver et al.* (2006).

CHAPTER V

Numerical Simulations

With the multiscale formulation and the finite element implementation developed, this chapter presents numerical simulations of some benchmark problems and physically relevant examples to demonstrate the effectiveness and applicability of the multiscale framework for cohesive crack propagation. Initially mesh objectivity, which is of primary importance in finite element based crack propagation simulations, is presented in Section (5.1). Then, mixed mode crack propagation in some benchmark problems is discussed in Section (5.2). Later, more complex scenarios of multiple and interacting crack are addressed in Section (5.3) and finally, closing remarks are provided in Section (5.4).

All simulations are in 2D and assume plane stress conditions. Also, in all simulations the crack evolves from a preexisting 'starter crack'. Further, as indicated in Section (4.4), a crack tracking algorithm is required as part of the iterative process to evolve the crack from one element to another. Such an algorithm should be based on a physically relevant crack direction criterion, and may be material and microstructure subjective. In this work, it is assumed that the crack propagates along a path that renders the shear stress to be zero. This amounts to assuming that the crack is locally governed by a Mode-I criterion. However, the direction criterion places no limitation on the multiscale formulation and depending on the material micromechanics, any relevant direction criterion can be chosen.

It is also pointed out that apparent distortion of the elements may be seen as contradicting the infinitesimal strain assumption of linear elasticity and also potentially result in singular jacobians for those elements. This is not the case as:

- Only the regular component of the strain needs to satisfy the infinitesimal strain assumption, as the singular component which lead to this observed element distortion does not contribute to the stress-strain constitutive relation (Section (3.3)).
- Since the implementation is in the reference configuration, the element distortion has no effect on the parametric space to real space mapping.

To remove this potential confusion, the crack path elements are removed from the simulation plots during post processing, except in Section (5.1) where the discussion is primarily based on the mesh.

All the simulations were carried out using an in-house, C++ based, variational multiscale cohesive method (VMCM) finite element code developed by the author. A standard Newton-Raphson scheme was used for solving the system of non-linear equations, based on a direct solution procedure using the SuperLU library *Demmel et al.* (1999).

5.1 Mesh Objectivity Demonstration

The discussion in Section (4.1) highlights the mesh sensitivity of the standard finite element implementation for simulating crack propagation. As stated previously, eliminating pathological mesh dependence of crack propagation simulations is one of the primary motivations for the development of the multiscale framework, and this section seeks to demonstrate the mesh objectivity of this implementation. The results presented in this section focus on the dependence of the global load-displacement response and the crack path, the two most important metrics from a structural viewpoint, on the mesh density.

5.1.1 Straight Crack Propagation

Consider the problem of a cohesive tension block under uniaxial tension, as shown in Figure (5.1). Shown are the problem schematic, resulting crack paths for meshes whose density varies over two orders of magnitude, and the corresponding global load-displacement response. It should be sufficiently clear from this result that the traditional pathological mesh dependence is completely absent for the case of a straight crack path. However, this physical problem involves no crack turning, so the sensitivity of the crack path discussed in Section (4.1.2) is not manifested here. A more complex problem involving curved crack propagation is presented in the following subsection.

The load-displacement response in Figure (5.1 C) is physically relevant, as it indicates that the strain energy release rate, G, and the surface energy density, γ' (Section (2.1.1.1)) are mesh independent, because the area under the curve is equal to the energy dissipated due to surface creation.

5.1.2 Curved Crack Propagation

Figure (5.2) shows the response of a standard Single Edge Notch Three-Point Bend (SETB) specimen under eccentric loading conditions. Due to the unsymmetrical loading, the crack deviates from its straight path and approaches the loading point as this is the contour of the maximum normal tractions, and the load-displacement and crack path is objectively simulated across all the mesh densities considered.

However, at first glance, the small variation in the load-displacement response and crack path may suggest mesh sensitivity. This is expected, as even in the absence of cracks, the resolution of the high stress gradients does depend to a small degree on the element dimension, and this naturally affects the crack direction determination and consequently the load-displacement response. Thus, these small variations are not pathological, as can be seen from Figure (5.2 C), but an artifact associated with numerical discretization used in the finite element method.

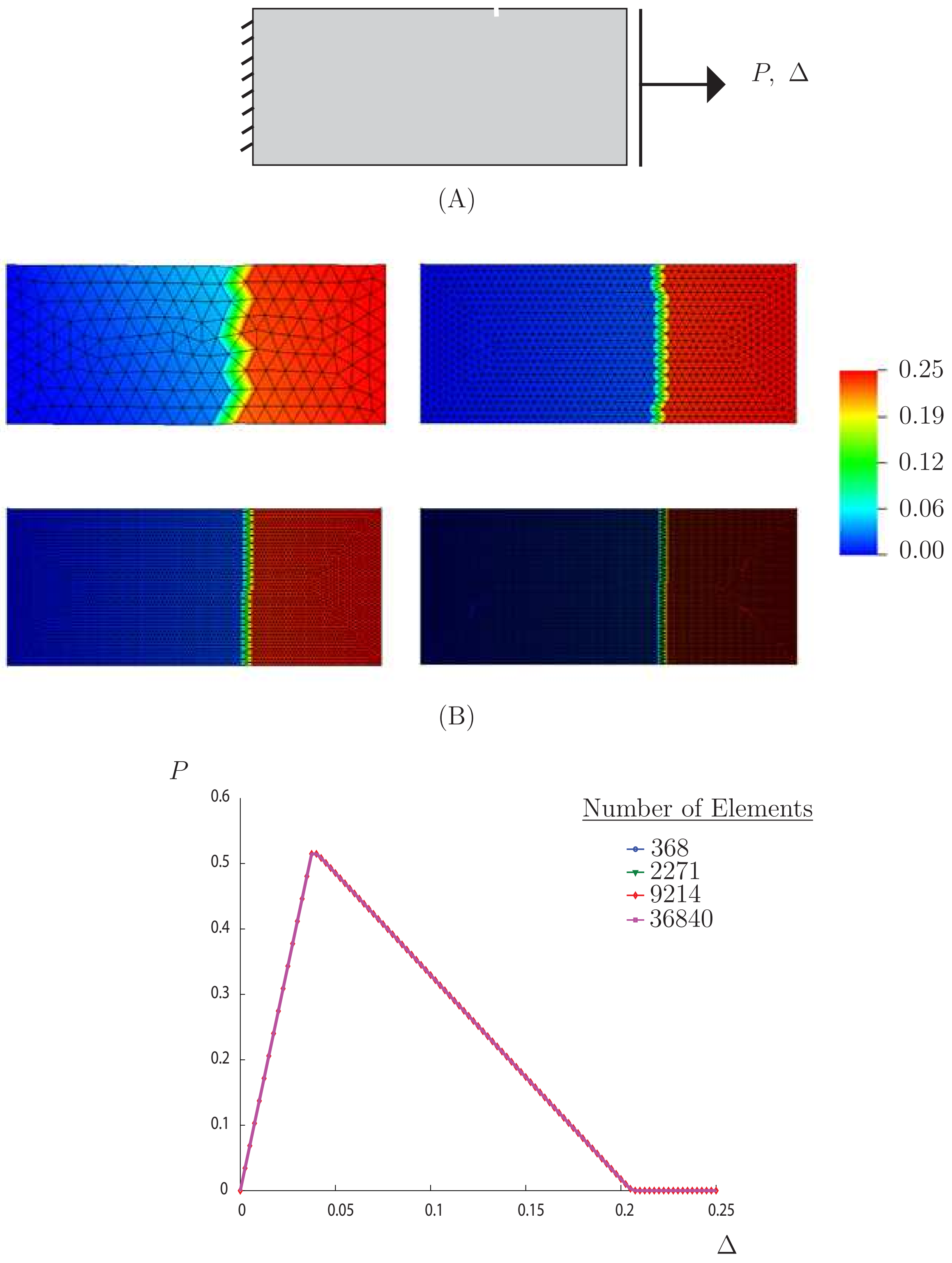

(A)

(B)

(C)

Figure 5.1: *Mesh objectivity demonstration for straight crack propagation. (A) Rectangular cohesive material under uniaxial tension, (B) Displacement magnitude contours for different mesh densities, (C) Corresponding load-displacement response. The P and Δ values have been normalized with fixed reference values.*

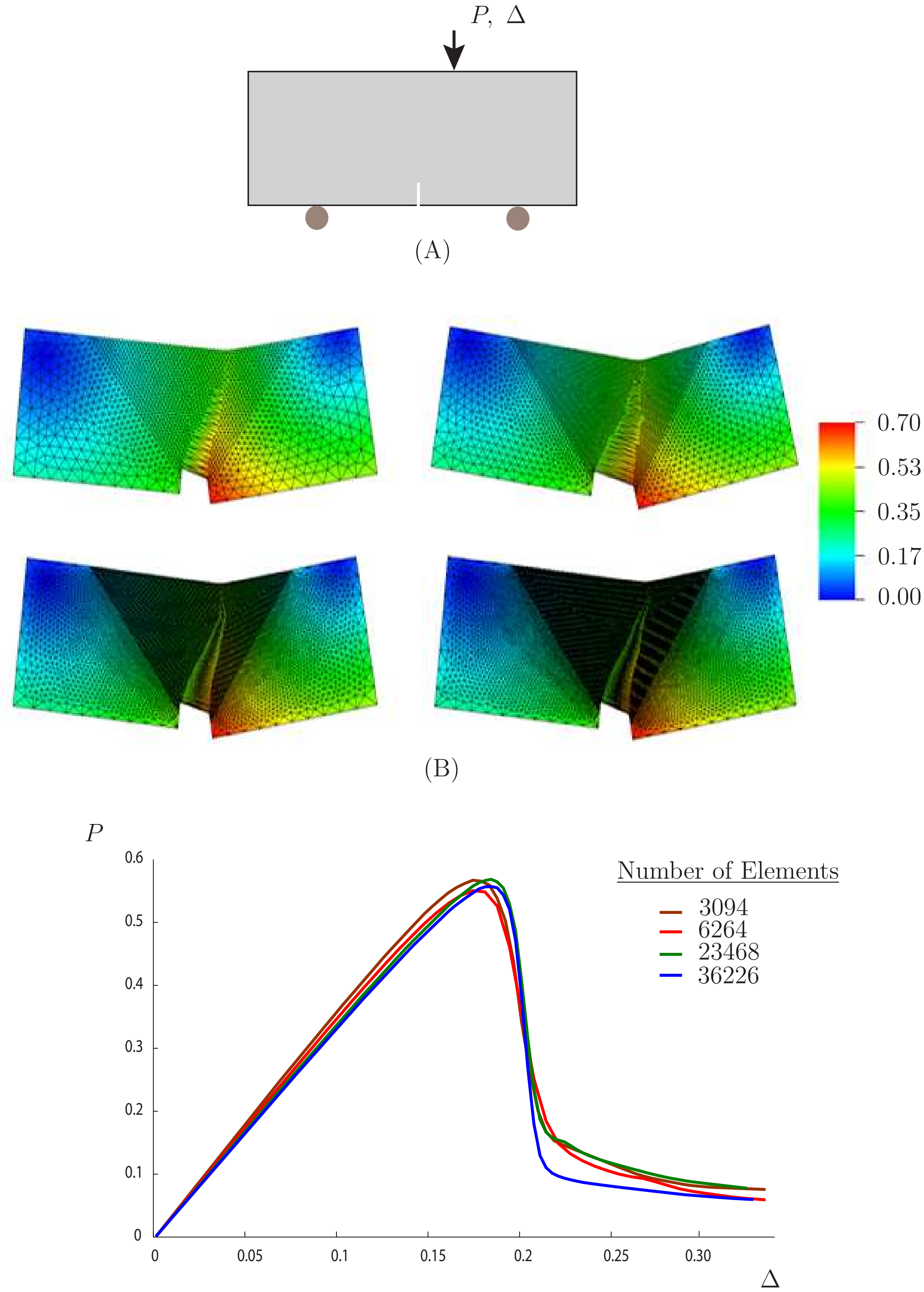

(A)

(B)

(C)

Figure 5.2: *Mesh objectivity demonstration for curved crack propagation. (A) Eccentrically loaded SETB specimen, (B) Displacement magnitude contours for different mesh densities, (C) Corresponding load-displacement response. The P and Δ values have been normalized with fixed reference values.*

5.2 Mixed Mode Crack Propagation

Mixed-mode refers to the condition where the crack face is subjected to both in plane and out of plane tractions. In 2D, this means that the crack face is under the influence of both Mode-I opening tractions and Mode-II shear tractions. Crack propagation involving non-straight paths is often mixed-mode and so their will be two cohesive traction-separation relations corresponding to normal-opening and shear-slipping modes. This section demonstrates the mixed-mode fracture simulation capability of the multiscale implementation. As stated earlier, the crack path elements are removed and for better visualization only the field contours are shown, without the underlying mesh.

Figure (5.3) shows snapshots of crack propagation in a symmetrically loaded Compact Tension (CTS) specimen. Although the mixed-mode scheme is active, the symmetry in the specimen and loading result in near straight crack propagation with very little crack face shear. However, the opening stress contours provide insights into the load bearing ability of materials with large process zone sizes. As seen in the evolving contour plots, the majority of the stress concentration is in the crack wake and this provides resistance to crack growth. This increased resistance to crack growth can also be implied from the corresponding load-displacement response which is flat indicating the increased fracture toughness of this material. The crack face bridging, as evident from the stress contours, gradually increases in size, then approaches a steady state value before shortening as the crack approaches the specimen boundary where the compressive stress is significant due to bending.

Figure (5.4) shows mixed-mode curved crack propagation in an eccentrically loaded SETB specimen where the crack approaches the loading point along the contour of the maximum normal tractions. Similarly, Figure (5.5) shows crack propagation in a rectangular specimen with a fully constrained left end and a displacement loading at the lower right corner. Also, it is experimentally observed that the crack propagation in laminated fiber reinforced composite materials is predominantly along the fiber layup direction, so the effect of restricting the crack propagation direction in the simulations is shown in Figure (5.6), where the crack path is restricted to the -45/0/+45/+90 fiber layup directions.

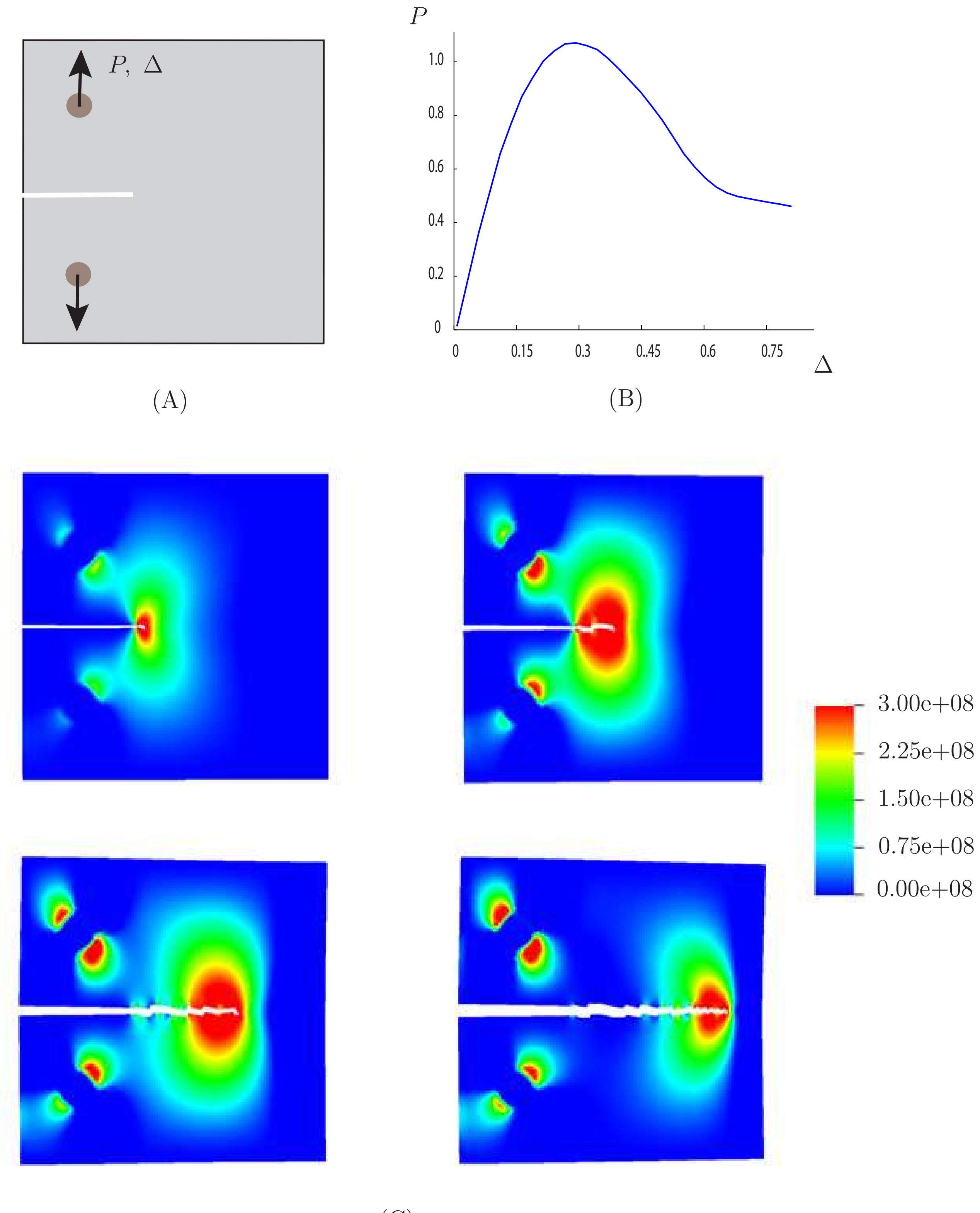

(A)

(B)

(C)

Figure 5.3: *Mixed-mode crack propagation in an symmetrically loaded CTS specimen(A) CTS specimen, (B) Corresponding load-displacement response., (C) Evolving opening stress* σ_{yy} *magnitude with crack growth. The* P *and* Δ *values have been normalized with fixed reference values.*

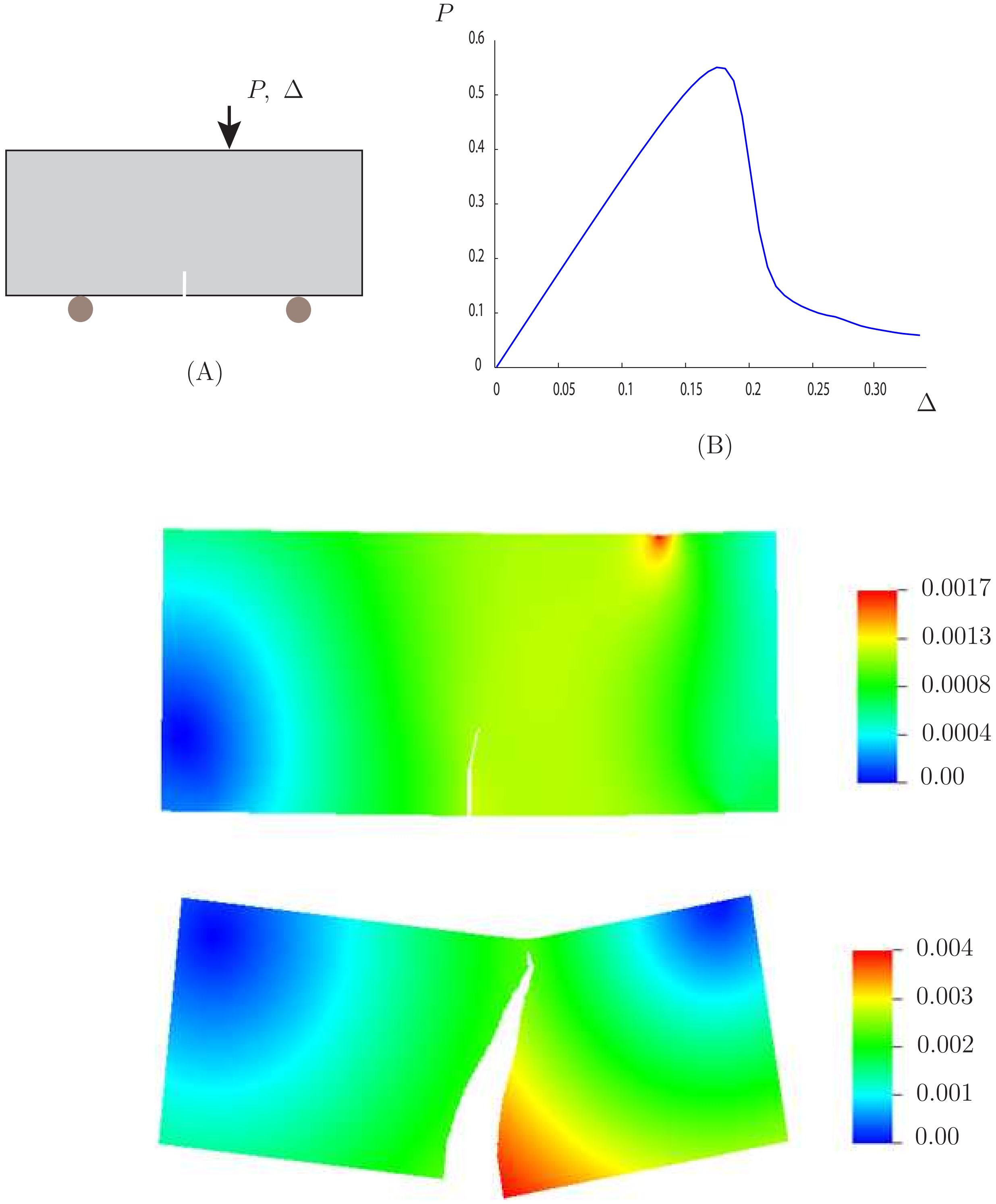

(A)

(B)

(C)

Figure 5.4: *Mixed-mode crack propagation in an eccentrically loaded SETB specimen. (A) Eccentrically loaded SETB specimen, (B) Corresponding load-displacement response, (C) Evolving displacement magnitude with crack growth. The P and Δ values have been normalized with fixed reference values.*

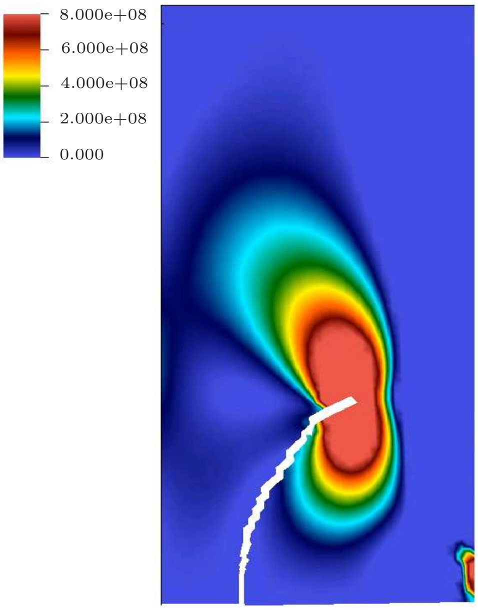

Figure 5.5: *Mixed-mode crack propagation in a rectangular specimen with the left end fully constrained and a displacement loading at the lower right corner. Shown are the crack path and the opening stress contours.*

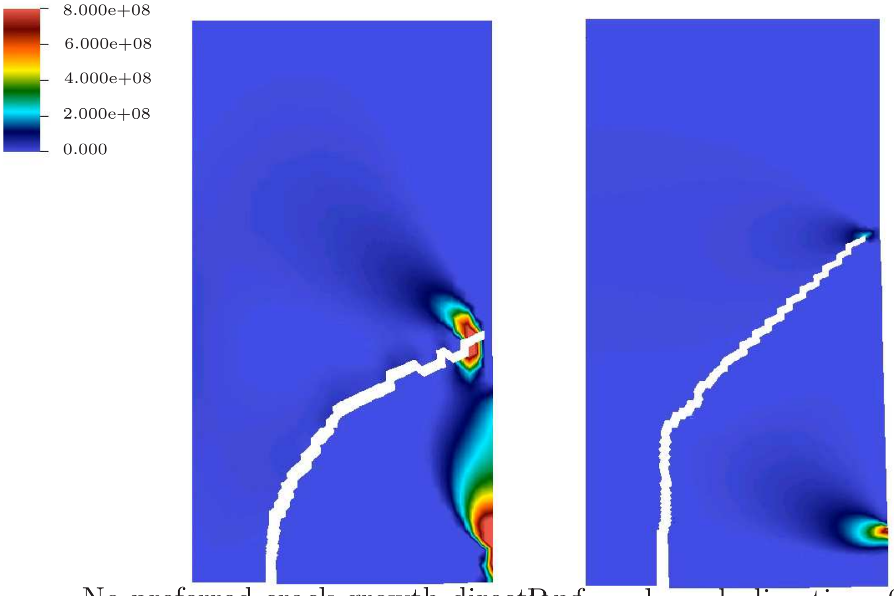

No preferred crack growth directions

Preferred crack directions 0/45/90 deg

Figure 5.6: *Mixed-mode crack propagation with restricted crack growth directions in a rectangular specimen with the left end fully constrained and a displacement loading at the lower right corner. Shown are the crack path and the opening stress contours.*

5.3 Interacting and Multiple Cracks

In this subsection, complexity due to multiple cracks, interactions between cracks and interaction with structural inclusions are addressed. It is stressed that the multiscale formulation has no restriction on the number of possible cracks in a domain or on their interaction.

Consider the standard Double Edge Notch Tension (DENT) specimen crack propagation simulation in Figure (5.7). As expected, two cracks start from notches on either side and approach each other, and the opening stress contours show their interactions. Initially, either crack grows independently, but as they get closer, they interact through the long range terms of the asymptotic expansion of the crack tip stress. However, due to the small offset in their crack paths, induced due to the numerical discretization, they pass each other. But eventually the crack paths intersect and one branch of the combined crack becomes predominant while the other branch relaxes. This problem also serves as an example of how an otherwise complex crack interaction, can be clearly understood through the numerical implementation.

Of interest in practical structures is the interaction of a crack with hard and soft inclusions. Shown in Figure (5.8) is one such scenario, where a crack encounters a hard inclusion along its path. The inclusion material has the same elastic modulus as the surrounding material, but its cohesive strength is three orders of magnitude higher. Thus the crack cannot propagate through the inclusion, instead bypasses the inclusion by traversing along its boundary. Another scenario of practical interest is crack arresting. Depending on the inclusion geometry and specimen loading, crack propagation will either be delayed or at times completely arrested. Such analysis can potentially aid in developing materials with artificial toughening by dispersed inclusions.

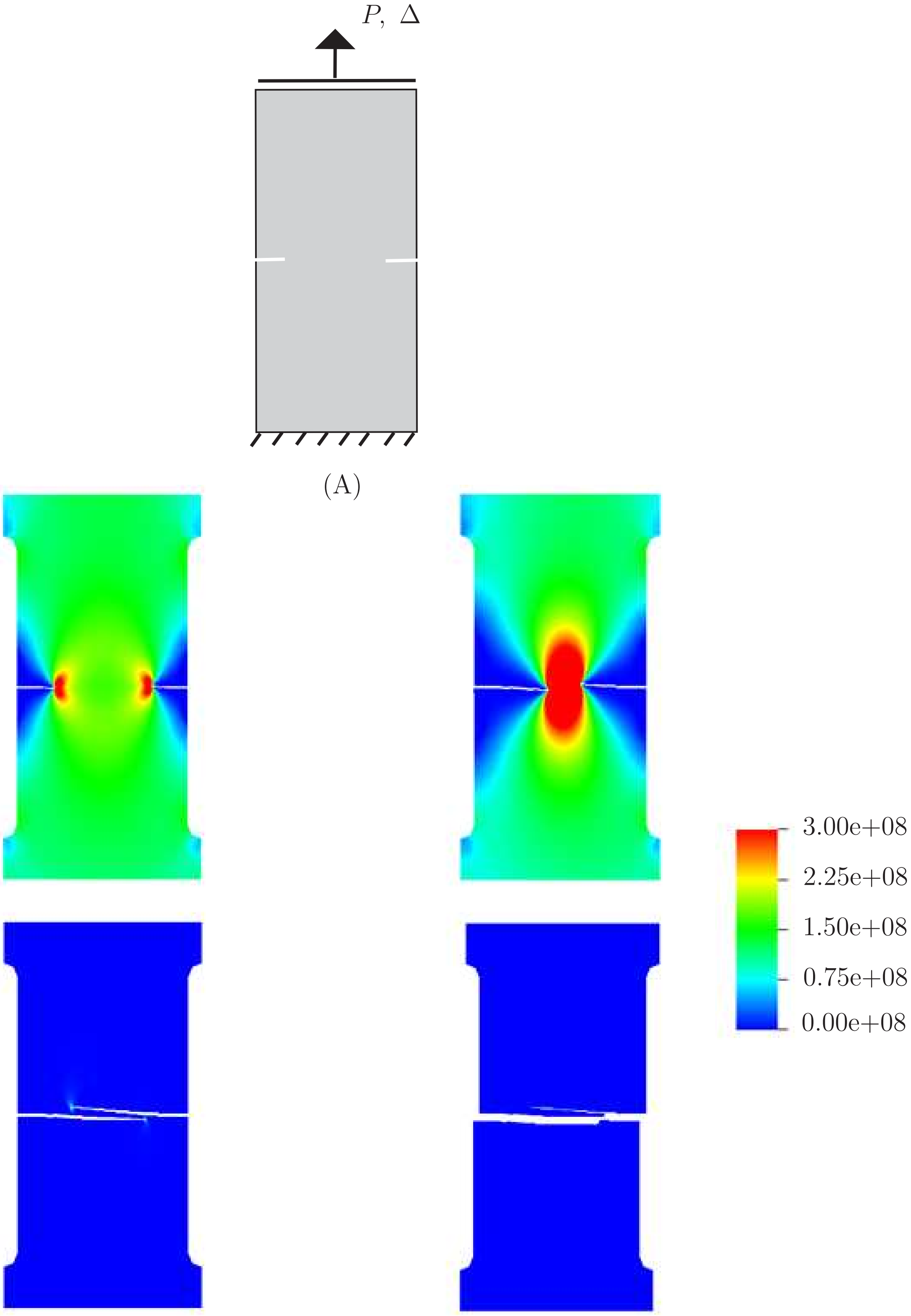

(A)

(B)

Figure 5.7: *Cohesive crack propagation in DENT specimen. (A) DENT specimen, (B) Evolving opening stress σ_{yy} magnitude with crack growth*

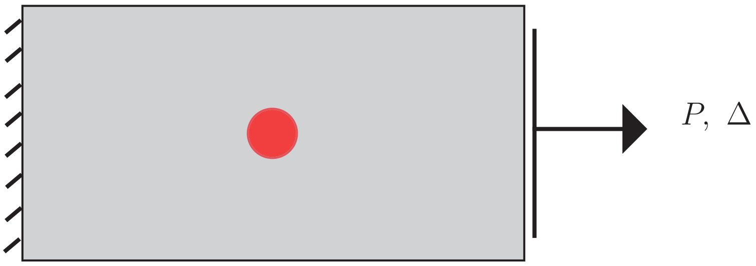

(A)

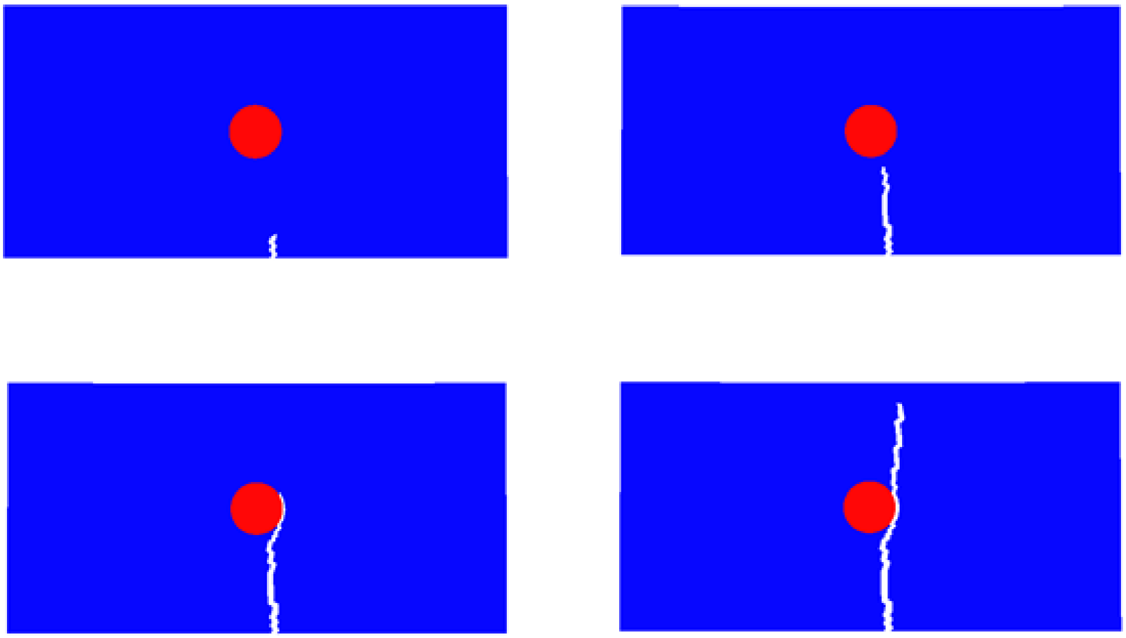

(B)

Figure 5.8: *Cohesive crack propagation in the presence of a hard inclusion. (A) Tension block with hard inclusion shown in red, (B) Evolving crack path.*

5.4 Closing Remarks

In conclusion, the numerical examples in this chapter demonstrate the ability of the multiscale formulation in simulating cohesive crack propagation. The crack paths and the global load-displacement responses obtained are numerically objective and physically consistent. The specimens and loading scenarios considered are sufficiently complex and relevant to practical applications, as will be further demonstrated in the next chapter on experimental validation.

CHAPTER VI

Experimental Validation and Analysis

While the previous chapter focused on illustrating the capabilities of the multiscale framework, this chapter seeks to demonstrate its practical applicability by validating the simulation results with experimental observations of crack propagation in laminated fiber reinforced composite panels. Section (6.1) provides details of the material used and the experimental setup. This is followed by comparison with corresponding numerical results in Section (6.2). It is to be noted that all the experiments described here were conducted by other collaborators, and their experimental results were used by the author to validate the multiscale framework. Also, due to proprietary requirements, the reported cohesive material properties and load-displacement curves were normalized.

6.1 Experimental Setup

The material used in all the experiments herein is a carbon fiber/epoxy $[-45/0/+45/90]_{6s}$ laminated fiber reinforced composite with a fiber volume fraction of 0.55, and whose lamina and laminate properties are given in Table 6.1. The nominal thickness of all the panels tested is 6.35 mm and their layup cross section is shown in Figure 6.1. The tests were conducted with a loading rate of 0.01 mm/sec (0.0004 in/sec). Two types of experiments were conducted with the following goals:

- Characterization of the laminate cohesive properties for through-the-thickness crack

Table 6.1: *Lamina and laminate properties of carbon fiber/epoxy* $[-45/0/+45/90]_{6s}$ *laminated fiber reinforced composite.*

Laminate	Lamina
E_{xx}: 51.5 GPa	E_{11}: 141 GPa
E_{yy}: 51.5 GPa	E_{22}: 6.7 GPa
G_{xy}: 19.4 GPa	G_{12}: 3.2 GPa
ν_{xy}: 0.32	ν_{12}: 0.33

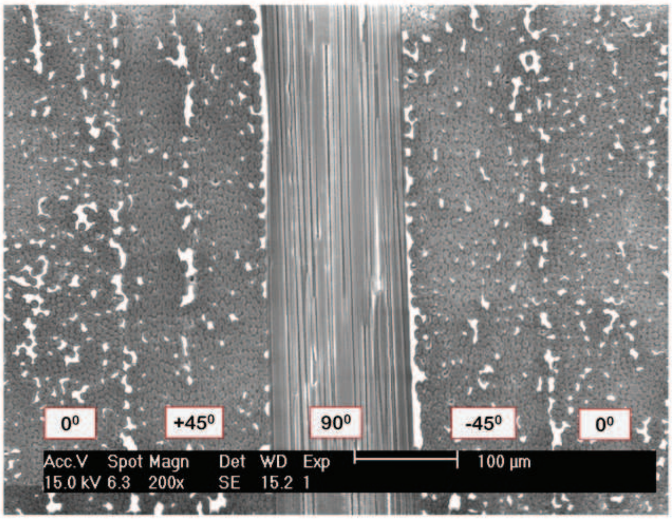

Figure 6.1: *Cross section of the* $[0/45/90/-45]_{6s}$ *specimen layup*

propagation.

- Crack propagation case studies for validation of the multiscale framework.

Details about the various specimen geometries and their experimental setup are given in the following two subsections.

6.1.1 Characterization of Cohesive Properties

The numerical modeling of crack propagation in this class of materials require a cohesive constitutive relationship, referred to as a traction-separation law. Here we assume a linear traction-separation law [Equation (3.19)], shown in Figure 6.2, which can be characterized by an appropriate fracture toughness (G_{Ic}/G_{IIc}) value and a corresponding cohesive strength T_0^c. However, in this class of materials, since the crack initiates in Mode-I, which is also the predominant load bearing mode in the crack wake, experimental characterization was focused primarily on obtaining the Mode-I traction-separation relationship.

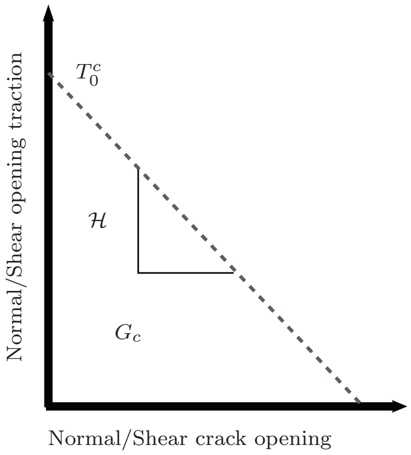

Figure 6.2: *A representative linear traction-separation law. For each of the fracture modes, T_0^c is the corresponding cohesive strength, G_c the fracture toughness and $\mathcal{H}$ the softening moduli.*

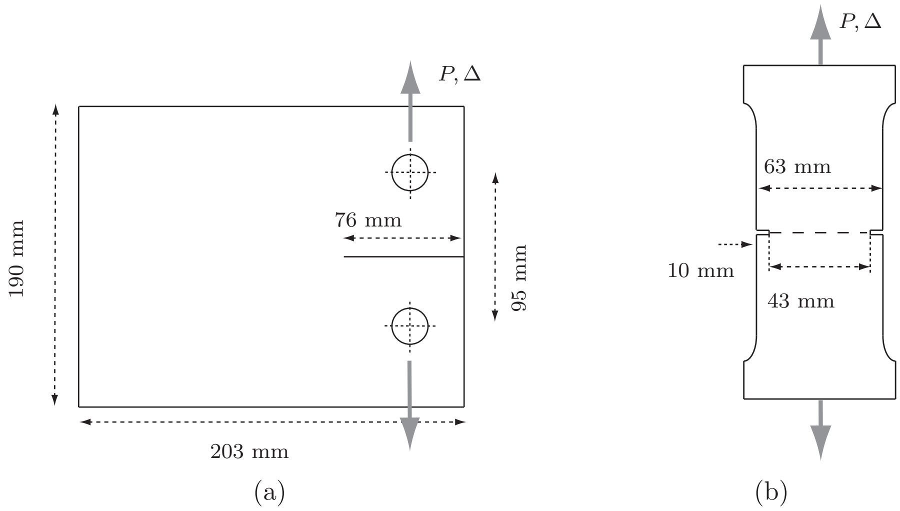

(a) (b)

Figure 6.3: *(a) Compact tension specimen (CTS) configuration, (b) Double edge notch tension (DENT) specimen configuration.*

For this purpose, compact tension specimen (CTS) fracture tests were carried out to measure the Mode-I fracture toughness. Figure 6.3(a) shows the dimensions of the specimen used in these studies. The fracture toughness value was calculated by normalizing the area under the experimental load-displacement curves by the total crack area. This method of computing the fracture toughness has been addressed in detail in *Rudraraju et al.* (2010). Load was measured using a load cell mounted on the MTS test frame, and the load point displacement was measured using an LVDT which was mounted between the loading rollers.

Double edge notched tension (DENT) tests were carried out to measure the critical Mode-I cohesive strength. Figure 6.3(b) shows the dimensions of the specimen. This configuration was selected because the stress state across the entire crack face is almost uniform and specimen failure is instantaneous. Thus, the critical load divided by the total crack cross section area gives a fairly accurate estimate of the critical traction across the crack faces. It was observed that this value was independent of the specimen width.

6.1.2 Crack Propagation Case Studies

Three types of specimen geometry and loading conditions were considered to serve as case studies for validating the simulation results:

- *Symmetric Single Edge Notch Three Point Bend Tests*: The SETB configuration used in this study is shown in Figure 6.4. A notch was introduced and a knife edge was used to introduce a sharp starter crack. The specimens were supported on rubber rollers both at the loading and support points to minimize any local inelastic deformation. The specimens were loaded on a specially designed loading frame with anti buckling guide rods that prevents out of plane movement of the specimens. The specimens were loaded using a hydraulically operated MTS testing machine and were loaded until failure. Load was measured by a load cell and the load point displacement was measured in between the top and bottom loading rollers using an LVDT. Five specimen sizes with geometrically scaled planar geometry and fixed thickness were considered. Multiple specimens of each size were tested to significantly capture the failure response envelope.

- *Eccentric Single Edge Notch Three Point Bend Tests*: To induce curved crack prop-

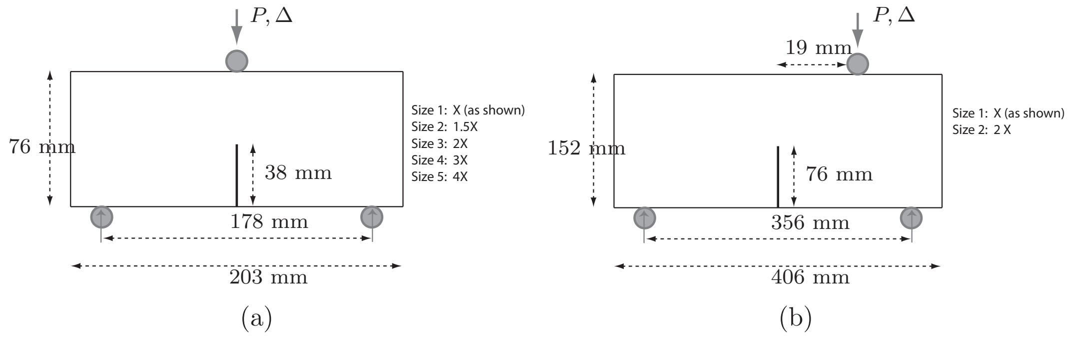

Figure 6.4: *Single edge notch three point bend (SETB) specimen configurations used in the crack propagation experiments. (a) Symmetric loading, (b) Eccentric loading.*

agation, an eccentricity was introduced in the loading point location. The eccentric SETB configuration is shown in Figure 6.4. The loading setup was similar to that of the symmetric SETB specimens.

- *Eccentric Compact Tension Tests*: Unlike the eccentric SETB tests, the eccentricity here was in the geometry, as shown in Figure 6.5. The notches in the center of the CTS specimens were moved by 10 mm for first set of tests and 20 mm for the second set of tests.

In each case, the global load-displacement response was recorded. These experimental load-displacement curves and the observed crack paths are compared with the simulation results in the next section.

6.2 Numerical Simulations and Comparison With Experiments

All simulations here are assumed to be under 'locally' Mode-I conditions. The Mode-I cohesive strength was obtained by DENT specimens as described in Section 6.1.1, and this value was fixed for all specimen sizes and geometries simulated in this section. The Mode-I fracture toughness in this class of materials is both size and geometry dependent, so the fracture toughness obtained from CTS experiments in Section 6.1.1 could be used directly

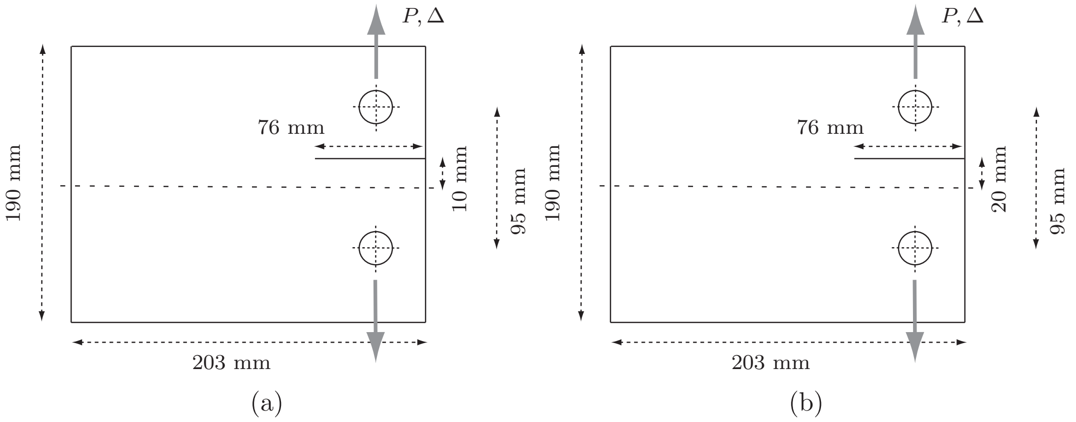

Figure 6.5: *Eccentric compact tension specimen configurations used in the crack propagation experiments. (a) Eccentricity: 10mm, (b) Eccentricity: 20mm.*

in the eccentric CTS simulations, but for the symmetric and eccentric SETB simulations, the fracture toughness was computed by normalizing the area under their respective experimental load-displacement curves by the total crack area. For a detailed discussion on this choice of Mode-I fracture toughness, readers are referred to *Rudraraju et al.* (2010). In each of the simulations below, the meshes contain about ten to twenty thousand elements. Again, the crack path elements were removed during post processing for better visualization.

Consider the first case-study of the symmetrically loaded SETB specimens whose experimental observed and numerically obtained load-displacement responses are shown in Figure 6.6. Across the five sizes, the numerical simulations faithfully reproduce the experimental load-displacement response. Usually, the crack initiates before the peak load, and at the peak load the full bridging zone will be formed. Further crack growth leads to a drop in the load bearing ability of the panels due to the failure of the fibers in the crack wake leading to movement of the active bridging zone. The details of the effect of bridging zone formation and movement on the load bearing ability of the specimens has been explained in detail in *Rudraraju et al.* (2010).

Similarly, for the more complex case of eccentric SETB specimens, the numerically obtained load-displacement response and its comparison with experimental results is given by

Figure 6.7. For this class of materials, experimental load-displacement responses show sharp drops in the post-peak load regime, which can be attributed to the cohesive heterogeneity of this material. Since numerically the material is modeled as a homogeneous medium (with the effective elastic and cohesive properties), the numerical model has no spatial or angular distribution of the non-homogeneous material properties. Also, since in a cohesive material the crack wake also possess significant load bearing ability, the numerical model only predicts a smooth load displacement response in the post-peak regime. However, as seen from the comparison, the multiscale method captures the post-peak response fairly well, albeit without the sharp drops.

Lastly, for the case of eccentrically loaded CTS specimens, Figure 6.8 shows the comparison of the global load-displacement response. Again, the global response is very similar. The difference in the slope of the experimental and numerical curves in the linear regime of the curve is due to some amount of crushing under the loading rollers in the experiments. Further, Figure 6.9 shows a comparison of the experimental and numerical crack paths, which match significantly.

6.3 Closing Remarks

From a structural viewpoint, the crack path and the effective load bearing ability of a failed panel are of primary importance. Thus the close correlation between the experimental and simulation results presented in the chapter provide significant validation of the practical applicability of the multiscale methodology for simulating cohesive crack propagation.

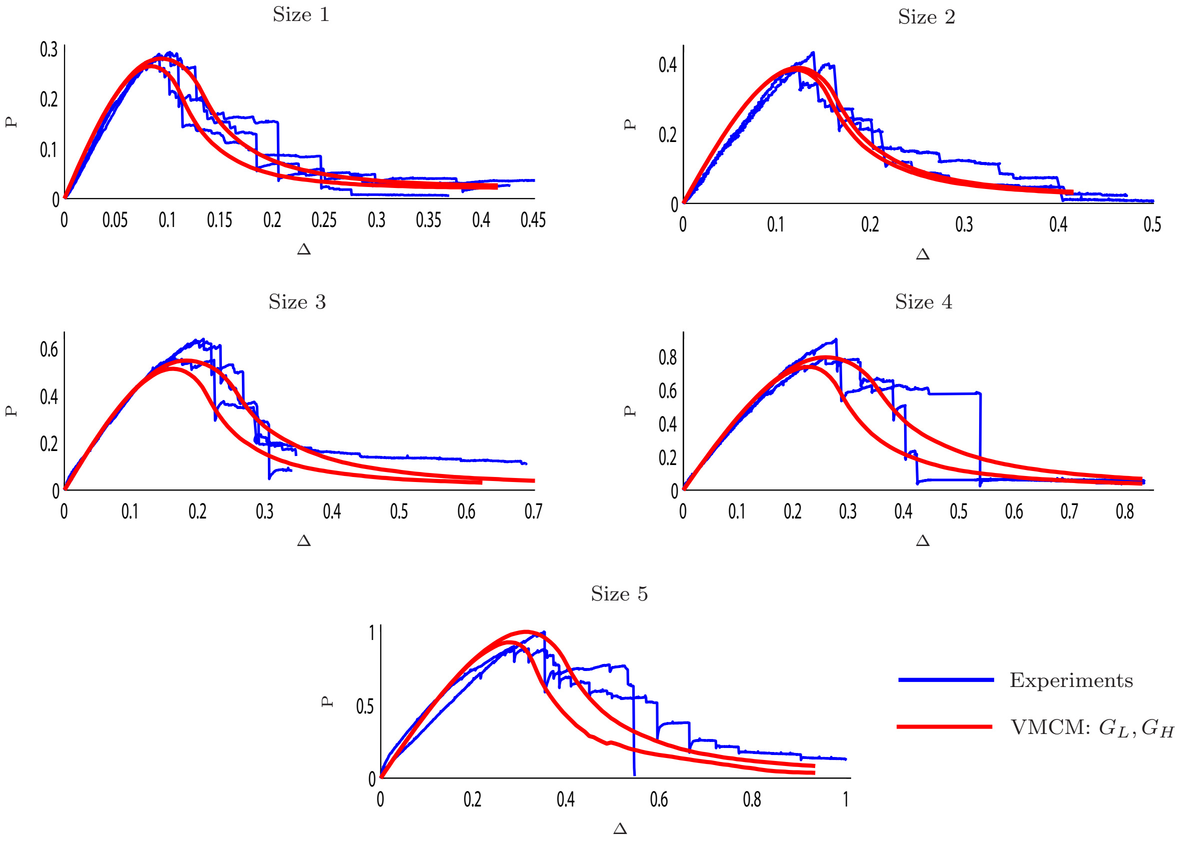

Figure 6.6: *Load-Displacement response obtained from simulations of symmetrically loaded Size 1-5 SETB specimens. For a particular specimen size,* G_L *and* G_H *represent the simulations with the least and highest values of the fracture toughness obtained from the experiments. The* P *and* Δ *values have been normalized with fixed reference values.*

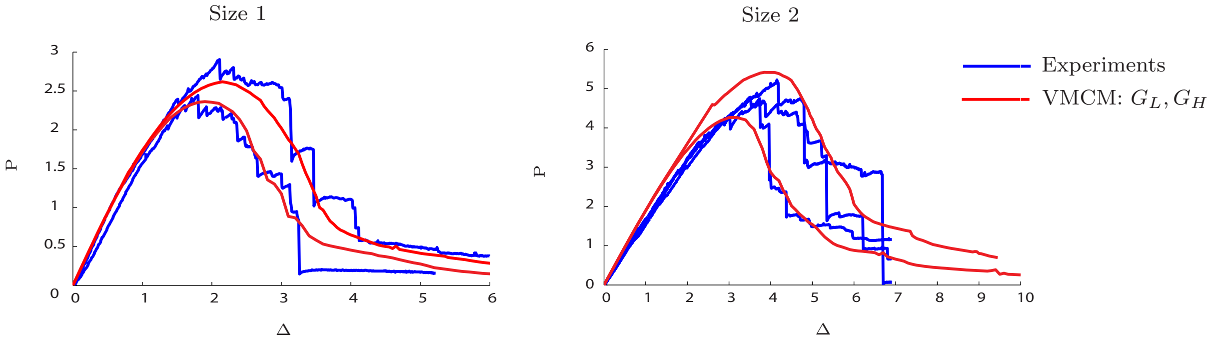

Figure 6.7: *Load-Displacement response obtained from simulations of Size 1 and Size 2 eccentric SETB specimens. For a particular specimen size,* G_L *and* G_H *represent the simulations with the least and highest values of the fracture toughness obtained from the experiments. The* P *and* Δ *values have been normalized with fixed reference values.*

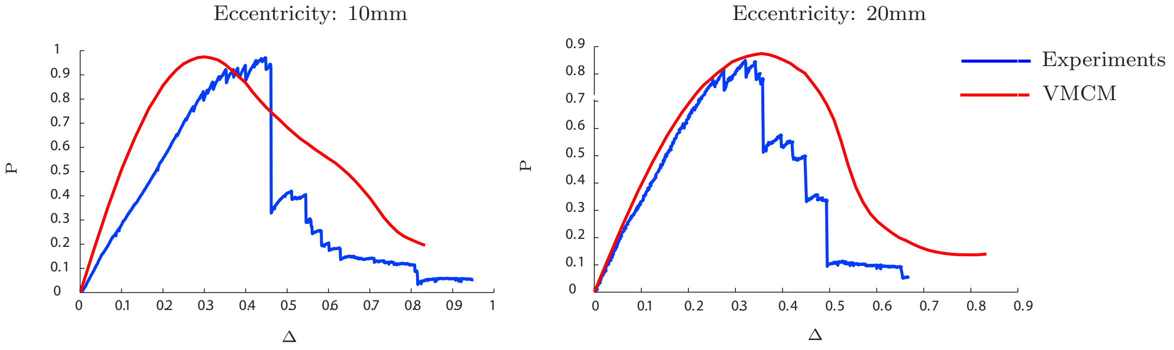

Figure 6.8: *Load-Displacement response obtained from simulations of eccentrically loaded CTS specimens. The* P *and* Δ *values have been normalized with fixed reference values.*

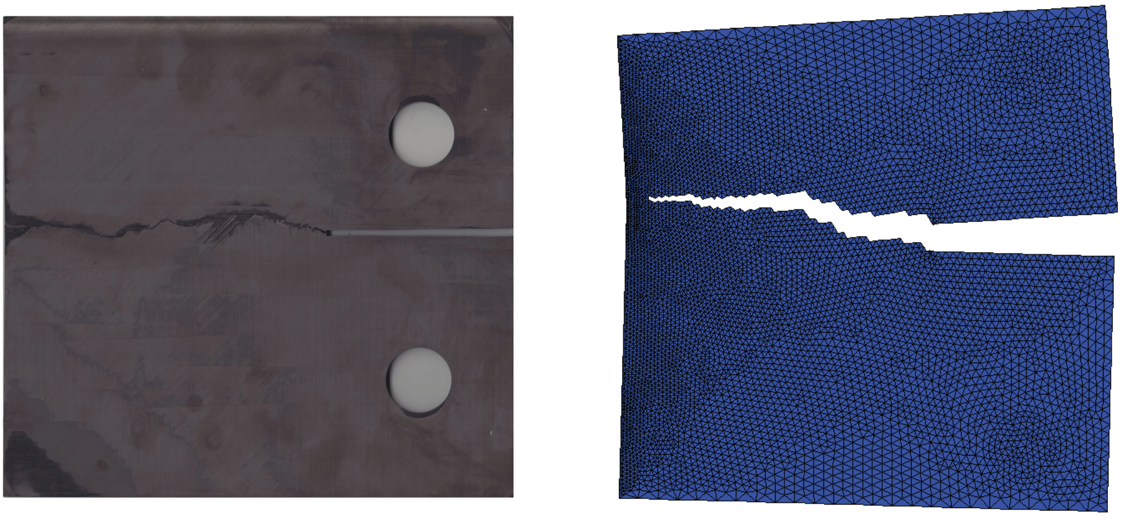

Eccentricity: 10mm

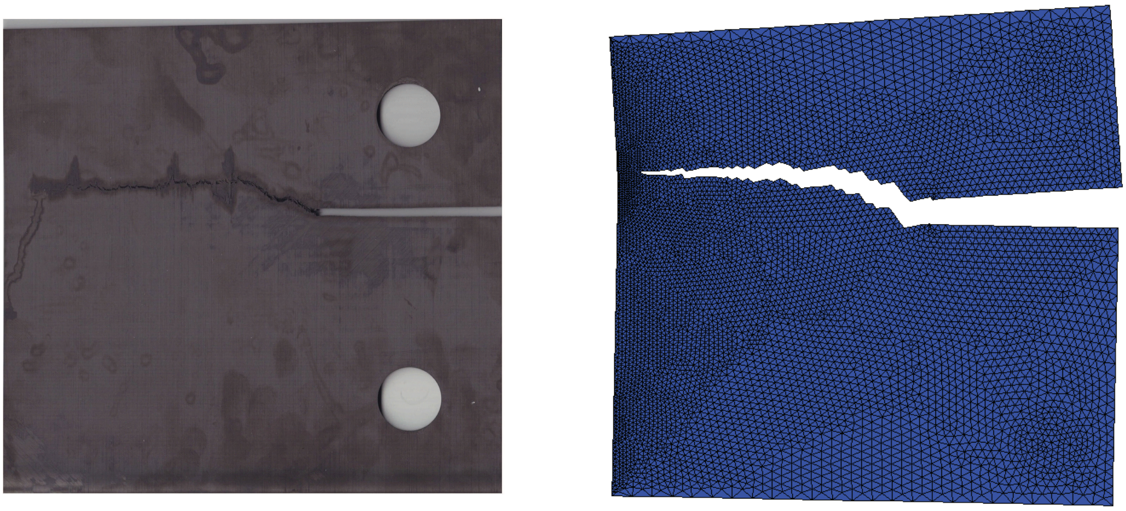

Eccentricity: 20mm

Figure 6.9: *Comparison of experimental and numerical crack paths for eccentrically loaded CTS specimens.*

CHAPTER VII

Conclusions and Future work

This dissertation has presented a complete framework for simulation and analysis of cohesive crack propagation, especially for materials involving large process zones. The broader aspects of this framework can be summarized as follows:

- *Theoretical aspects*: The necessary arguments for using analytically/numerically determined traction-separation relations have been discussed and a possible micromechanical framework for fiber-reinforced composites has been presented.
- *Computational aspects*: A variational multiscale formulation of crack propagation as a subgrid scale problem has been established and developed in the context of the finite element method. All the necessary numerical machinery (weak formulations, multiscale elements and iterative solution procedure) have been developed in complete detail. The resulting computational approach has been demonstrated through benchmark simulations and more importantly, experimentally validated.

Further, it is pointed out that this numerical framework, involving discontinuous basis functions, is generic enough to be extended to a wider class of problems involving not just crack propagation, but possible other phenomena involving micromechanical surface laws, like frictional contact.

Several possibilities for future work suggest themselves:

1. The work presented here is within the context of small deformations. An extension to finite deformation is naturally of interest. It is suggested that such a development would involve only minimal changes in the numerical framework and a possible source of inspiration are the related elemental enrichment methods involved in simulation of strong discontinuities which are essentially in a finite-deformation setting.

2. Another possibility is the extension to three dimensions. While the theory of crack propagation and the multiscale formulation will essentially remain unchanged, the multiscale element construction and crack tracking algorithms will be more challenging. Also, an extension to non-simplex elements would be helpful in broadening the applicability.

3. An important contribution would be the study of stability and convergence of the solution procedure involved in this class of problems with discontinuous enrichments. Also, given the high non-linearity inherent in these problems, a comparative study of various solver schemes will also be highly beneficial not just for crack propagation problems but to the broader field of discontinuous enrichment.

4. Although application specific, an extension to dynamic problems would be interesting for certain classes of problems involving high loading rates. Likewise, one may think of a possible application to shell elements, but this would be significantly complicated due to the introduction of rotations and possible rotational discontinuities, over the existing displacement discontinuities.

APPENDIX

APPENDIX A

Analytical and numerical modeling of the micromechanics of fiber-pullout

A.1 Introduction

The structural response of fiber-reinforced composites - a heterogeneous and discreet material medium, are significantly different from the monolithic materials, like metals, due to the various length scales and discreet directions of load transmission. In this study we focus on understanding the micromechanics related to the primary load bearing constituent of this material, the fiber. The aim is to describe the response of a fiber and its neighboring matrix material, from initial load bearing to eventual pullout, and analytically determine the single-fiber traction-separation relation. This understanding will then be cast into the finite element numerical framework to demonstrate the micromechanics and to extend it to determine continuum level traction-separation relations. It is also noted that given the enormity of variations possible in the wider class of fiber-composites, the study presented herein may only be directly relevant to the following material behavior:

- Linear elastic matrix (no micro cracking or damage evolution).
- Strong brittle fibers with finite embedding length (no fiber breakage).

- Adhesive interface characterized only by the Mode-II fracture toughness. However, numerical models extend this by considering a more general complete traction-separation relation.

With these assumptions, we develop an analytical formulation for the single-fiber pullout problem. This formulation is based on the analytical framework presented by *Gao et al.* (1988), and many results are directly used. For the material under consideration, experimental observations have shown the formation of a fiber-bridging zone, whose evolution is schematically represented in Figure A.1. The corresponding micromechanical process are depicted in Figure 2.9. Assuming a displacement control loading at the free fiber end, the evolution of fiber pullout is decomposed into the following regimes:

A. *Interface crack formation*: Initial fiber loading, leading to enhanced shear stress in the fiber-matrix interface, which beyond a certain threshold value of energy availability leads to Mode-II interface crack formation.

B. *Interface crack propagation and frictional contact*: Mode-II crack facilitates tangential slip at the interface during subsequent fiber loading. The slipping or tendency of slipping leads to coulomb type frictional forces on the interface, leading to enhanced resistance to the fiber slipping, thus increasing the fiber load carrying ability.

C. *Fiber pullout*: The interface crack either reaches the end of the embedded fiber length or the fiber breaks at some weak point upon reaching the failure stress. This leads to significant loss of fiber load bearing ability, as now only the frictional forces are resisting the fiber movement. Further displacement increments at the free fiber end now lead to fiber pullout.

Section A.2 describes each of these regimes and develops an analytical formulation. Then the numerical framework and simulations are presented in A.3.

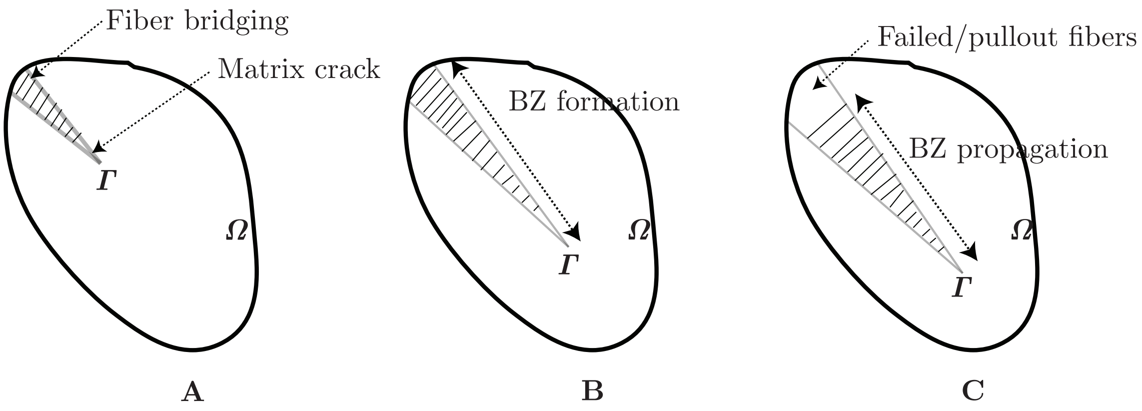

Figure A.1: *Stages involved the evolution of the bridging zone (BZ). A: Matrix cracking - Fiber bridging, B: Bridging zone formation, C: Bridging zone propagation.*

A.2 Analytical Formulation

A.2.1 Interface Crack and Frictional Contact

In order to study the fiber-matrix debonding and pullout problem, we consider a shear lag model like geometry of a fiber-embedded in a cylindrical matrix jacket as shown in Figure 2.9. Table (A.1) lists all parameters used in this model.

Assume that there is an initial debonded length, l formed due to formation of a mode-II shear crack in the interface. For the debonded zone, $y < l$, we have the following equilibrium conditions:

$$\frac{dT_f}{dy} = -\frac{dT_m}{dy} = 2\pi r \tau_s \tag{A.1}$$

and stress-strain relationships:

$$\begin{aligned} \epsilon_f &= \frac{du_f}{dy} = \frac{T_f}{\pi r^2 E_f} - \frac{2\nu_f}{E_f} q* \\ \epsilon_m &= \frac{du_m}{dy} = \chi \frac{T_m}{\pi r^2 E_m} - \frac{2\nu_m}{E_m} \chi q* \end{aligned} \tag{A.2}$$

where $\chi = r^2/(R^2 - r^2) = c_f/c_m$, and from *Gao et al.* (1988) we have $q* = \frac{1}{\pi r^2}\left(\frac{\alpha \nu_f T_f - \chi \nu_m T_m}{\alpha(1-\nu_f)+1+\nu_m+2\chi}\right)$

Table A.1: *List of symbols for fiber-pullout micromechanics*

Symbol	Representation
r	Fiber cylinder radius
R	Matrix cylinder outer radius
c_f, c_m	Fiber and matrix volume fraction
E_f, ν_f	Fiber elastic modulus and poisson's ratio
E_m, ν_m	Matrix elastic modulus and poisson's ratio
α	E_f/E_m
l	Instantaneous crack length
l_e	Fiber embedded length
P	Fiber free end load
Δ	Fiber free end displacement
q_0	Resin shrinkage pressure
$q*$	Additional pressure at interface due to poisson contraction
$T_f(y), u_f(y)$	Fiber tensile force and displacement
$T_m(y), u_m(y)$	Matrix tensile force and displacement
$\tau_s(y)$	Interfacial shear stress
μ	Coefficient of interface friction

Now, we assume that the zero thickness interface exhibits coulomb type friction. This lets us obtain a relationship for the interface shear stress τ_s, in terms of the the resin shrinkage pressure q_0, poisson contraction pressure $q*$, and the friction coefficient μ.

$$\tau_s = \mu(q_0 - q*) \tag{A.3}$$

Using the boundary conditions:

$$\begin{aligned} T_f(0) &= P \\ T_m(0) &= 0 \end{aligned} \tag{A.4}$$

and Equations (A.1) and (A.3) we obtain the fiber and matrix forces in the debonded zone, $y < l$:

$$T_m = (\frac{\alpha\nu_f}{\alpha\nu_f + \chi\nu_m})(\tilde{P} - P)(e^{\lambda y} - 1) \tag{A.5}$$

$$T_f = P - T_m$$

where the constants $\tilde{P}$ and λ are given by:

$$\begin{aligned}\tilde{P} &= \frac{\pi r^2 q_0}{\alpha \nu_f}\big[\alpha(1-\nu_f)+1+\nu_m+2\chi\big] \\ \lambda &= \frac{2\mu}{r}\Big(\frac{\alpha\nu_f+\chi\nu_m}{\alpha(1-\nu_f)+1+\nu_m+2\chi}\Big)\end{aligned} \tag{A.6}$$

Solving (A.2), we obtain the relative slipping between the fiber and matrix given by:

$$\upsilon(y) =\mid u_f(y) - u_m(y) \mid \tag{A.7}$$

$$\Rightarrow \upsilon(y) = \frac{P(l-y)}{\pi r^2 E_f}(1-2k\nu_f) - \frac{\alpha+\chi-2k(\alpha\nu_f+\chi\mu_m)}{\pi r^2 E_f(\alpha\nu_f+\chi\mu_m)}\nu_f(\tilde{P}-P)\big[\frac{1}{\lambda}(e^{\lambda l}-e^{\lambda y})-l+y\big] \tag{A.8}$$

where $k = \frac{(\alpha\nu_f+\chi\mu_m)}{\alpha(1-nu_f)+1+nu_m+2\chi}$. Equation (A.7), gives a relation between $\Delta = \upsilon(0)$ and P. This lets us obtain the load-displacement (P-Δ) response in the pre-cracking regime. Now lets shift our attention to the evolution of the interface crack length l, by considering the energetics of Mode-II crack propagation, along the fiber-matrix interface.

A.2.2 Interface Crack Propagation

Following the crack propagation treatment in *Gao et al.* (1988), consider a cracked body of volume V loaded by tractions T and τ_s on the surfaces S_T and S_F with corresponding displacements du and dv as shown in Figure A.2. For a crack growth dA along the friction surface S_F we can obtain from energy balance considerations:

$$\int_{S_T} T du ds = g dA + \int_{S_F} \tau_s d\upsilon ds + dU \tag{A.9}$$

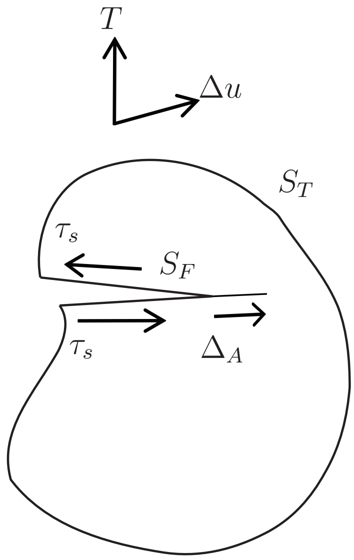

Figure A.**2:** *Schematic showing the evolution of debonding crack. S_T and S_F are the traction and friction surfaces.*

where g is the specific work of fracture, $\int \tau_s dv ds$ represents the work of friction and U is the stored energy of the body. For an elastic system, we have

$$dU = \int\limits_{S_T} T du ds - \frac{1}{2}\int\limits_{S_F} \tau_s dv ds \tag{A.10}$$

If the traction T consists of n concentrated forces $P_1....P_n$ and the displacements $\lambda_1...\lambda_n$ then (A.10) becomes:

$$g = \frac{1}{2}[\Sigma_{i=1}^{n} P_i \frac{\partial \Delta_i}{\partial A} - \int\limits_{S_F} \tau_s \frac{\partial v}{\partial A} ds] \tag{A.11}$$

Let $g = \zeta, A = 2\pi rl, ds = 2\pi r dy$ and $P_i (= P)$ is the force applied at the fiber end. Also, from (A.7) we can obtain $v(y)$ and $\Delta_i = -u_f(0)$. The debonding criterion is now given by:

$$\zeta = \frac{-P}{4\pi r}(\frac{\partial u_f(0)}{\partial l}) - \frac{1}{2}\int\limits_0^1 \tau_s \frac{\partial v(y)}{\partial l} dy \tag{A.12}$$

Solving Equation (A.12) by substituting u_f and $v(y)$ we obtain,

$$4\pi^2 r^3 E_f(1+\beta)\zeta = (1-2k\nu_f)[P-(1+\beta)Q]^2 \tag{A.13}$$

in which,

$$Q = T_m(l) = \frac{\alpha\nu_f(\tilde{P}-P)}{\alpha\nu_f+\gamma\nu_m}(e^{\lambda l}-1) \tag{A.14}$$

and

$$\beta = \frac{\gamma(1-2k\nu_m)}{\alpha(1-2k\nu_f)} \tag{A.15}$$

Equation (A.13) is the final fiber debonding criterion showing that the debonded load depends on debonded depth l. To obtain the debonding (Mode-II crack) initiation load P_0, we substitute $l=0$, giving:

$$P_0 = 2\pi r^{3/2}\left[\frac{E_f(1+\beta)\zeta}{1-2k\nu_f)}\right]^{1/2} \tag{A.16}$$

Further, Equation (A.13) can be simplified to obtain an expression for the instantaneous load P:

$$P(l) = \tilde{P}(1-e^{\lambda l}) + P_0 e^{-\lambda l} \tag{A.17}$$

and Equation (A.7) is used to obtain the value of $\Delta = v(0)$ in the crack propagation regime:

$$\Delta(P) = v(0) = \frac{1-2k\nu_f}{\pi r^2 E_f \lambda}\Big([P+(\tilde{P}-P)/K]ln(1+\frac{K(P-P_0)}{\tilde{P}-P}) - P + P_0\Big) \tag{A.18}$$

Equation (A.17) and (A.18), give the required relations to obtain the P-Δ response in the post- crack initiation regime until the point of pullout initiation.

A.2.3 Fiber Pullout

Equation (A.17) shows that the load increases monotonically with increase in the debonding (crack) length, l. This ultimately culminates in one of the following two scenarios:

- $l = l_e$: That is the crack propagates over the total embedded fiber length.
- $l < l_e$ but $P = P_c$: That is, the applied load produces a fiber tensile stress that exceeds the fiber strength and the fiber breaks at a weak point $y = l_b < l_e$.

In either case, we now make a slight change in what we mean by l. Earlier l was the length of the crack, and in the pullout regime by l we mean the length of the fiber inside the matrix. So, now l monotonically decreases from its pullout initiation length and ultimately approaches zero, which means total pullout of the fiber from the matrix.

In this regime, we have the following relation for the load, P:

$$P(l) = \tilde{P}(1 - e^{\lambda l}) \tag{A.19}$$

Thus Equation (A.19) shows that the load suddenly drops from the value in Equation (A.17) for the same l, as soon as the pullout has initiated. This elucidates the existence of a physical instability as soon as the mechanics change from crack propagation to pullout initiation. This is due to sudden loss of the load bearing ability of the friction zone at the crack tip which now sees a different material domain. Thus for any given fiber length in the matrix l, we can use Equation (A.19) to obtain the load value, and Equation (A.18) still holds for the current load value P.

Thus using Equation (A.19) and Equation (A.17), we can obtain the P-Δ response in the pullout regime until the point of complete pullout.

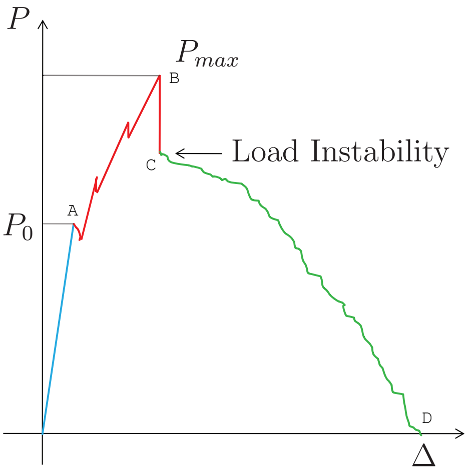

Figure A.3: *Schematic of fiber-pullout load displacement response. A:Crack initiation, A-B:Crack propagation and contact friction, B-C:Load instability, C-D:Fiber pullout.*

Table A.2: *Material properties for fiber-pullout micromechanics*

Property	Value
E_f	173 GPa
E_m	3.72 GPa
ν_f	.35
ν_m	.39
c_f	.06
μ	.3

A.2.4 Summary

Shown in Figure A.3 is the schematic of a typical load-displacement(P-Δ) response of a single fiber pullout. For given material properties, this load-displacement response can be obtained using the respective P-Δ relations listed at the end of each section of the above three regimes (Interface crack initiation and Frictional contact, Interface Crack Propagation and Fiber Pullout). For the material characteristics listed in Table A.2, the complete P-Δ response is shown in Figure A.4.

This completes the analytical formulation. We now divert our attention to the numerical framework developed to validate and extend the applicability of the analytical understanding and formulation.

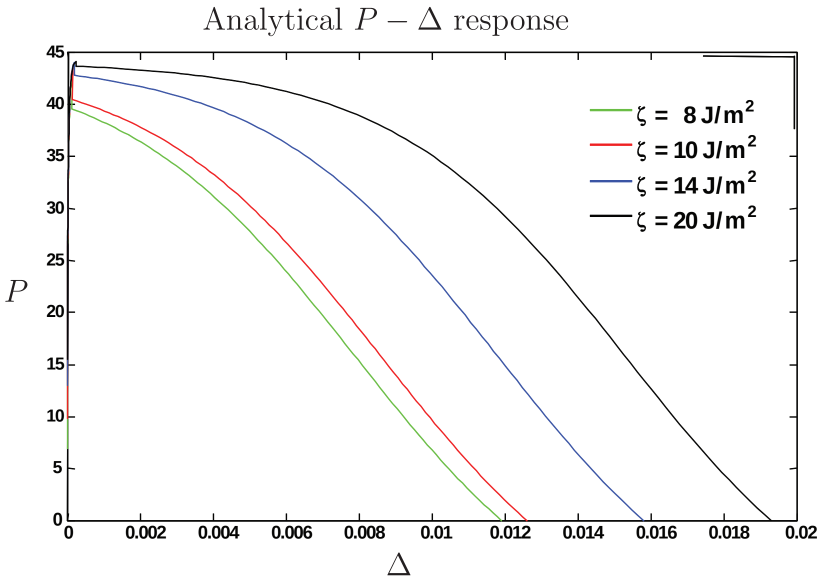

Figure A.4: *$P - \Delta$ response obtained from the analytical formulation presented for various values of interface fracture toughness ζ.*

A.3 Numerical Framework and Simulations

The fiber-pullout simulations were done in the Abaqus FEA package using user elements for fiber-matrix interface cohesive zones. To simulation the various non-linear mechanisms (deformation, fracture, contact, friction) which are active simultaneously, the following numerical scheme was used:

1. Fiber, Matrix (Deformation): Plane strain elements.
2. Interface (Crack Propagation): Discrete Cohesive Zone Methods (DCZM) interface elements [*Gustafson and Waas* (2009)].
3. Interface (Contact and Friction): Contact elements.

With this framework, various single fiber pullout, lamina level and unidirectional coupon level simulations were conducted, some of which are listed below:

1. Single fiber pullout model mesh (Figure A.5)
2. Single fiber pullout model fiber and matrix level shear stress contours (Figure A.6)
3. Single fiber pullout model fiber various stress contours (Figure A.7)

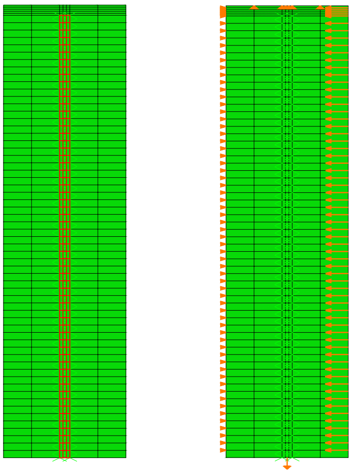

Mesh Boundary Conditions

Figure A.5: *Quadrilateral elements mesh and the applied boundary conditions.*

4. Lamina level stress contours: Regular and Random fiber distributions (Figure A.8)

These preliminary results demonstrate the potential applicability of this numerical framework for simulating micromechanics of fiber-pullout, and thereby obtaining the cohesive traction-separation relations.

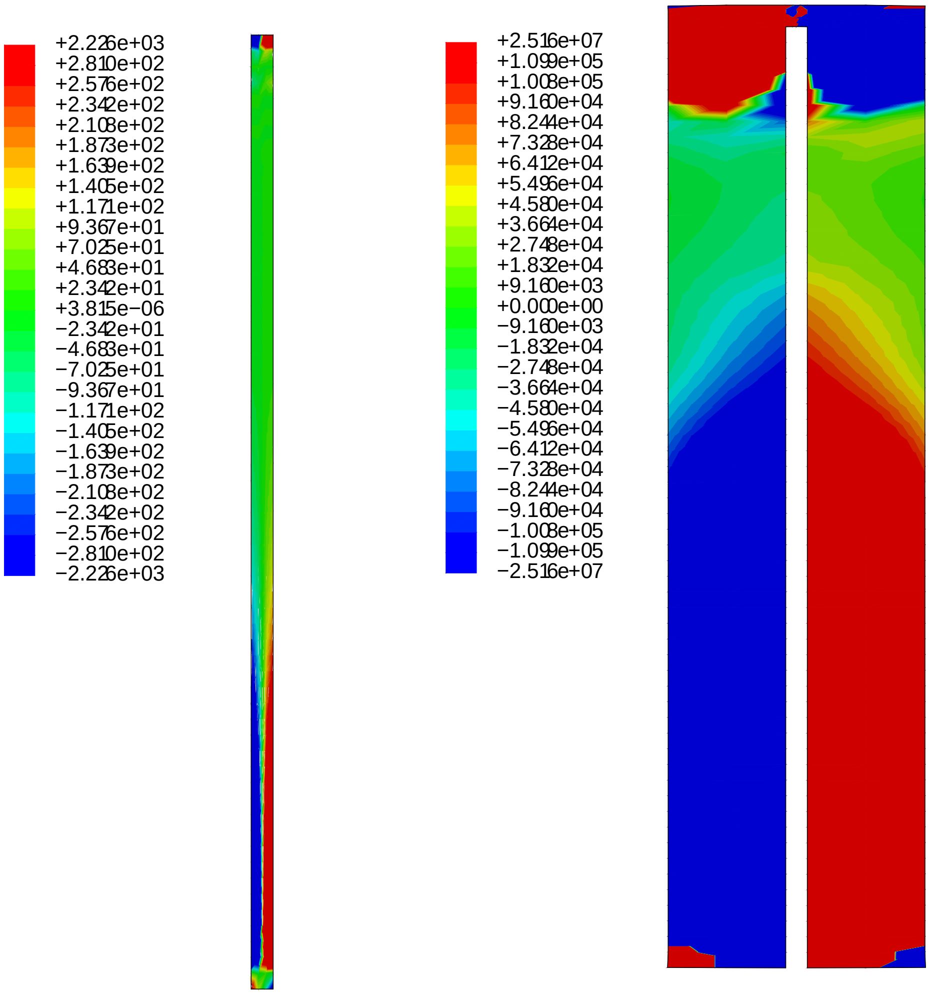

Fiber

Matrix

Figure A.6: *Shear stress in the fiber and the matrix during pullout shown as separate contour plots.*

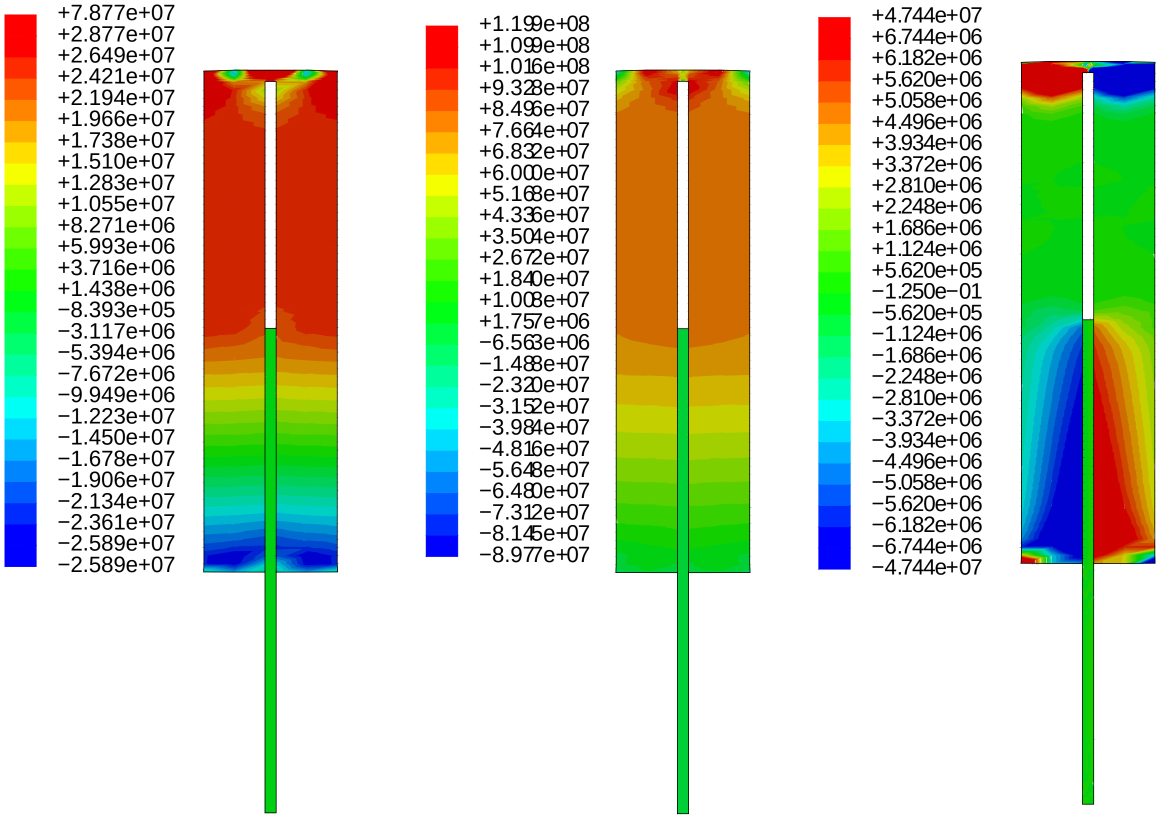

σ_{11} σ_{22} σ_{12}

Figure A.7: *Contour plots of the tensile and shear stresses in the single fiber pullout problem.*

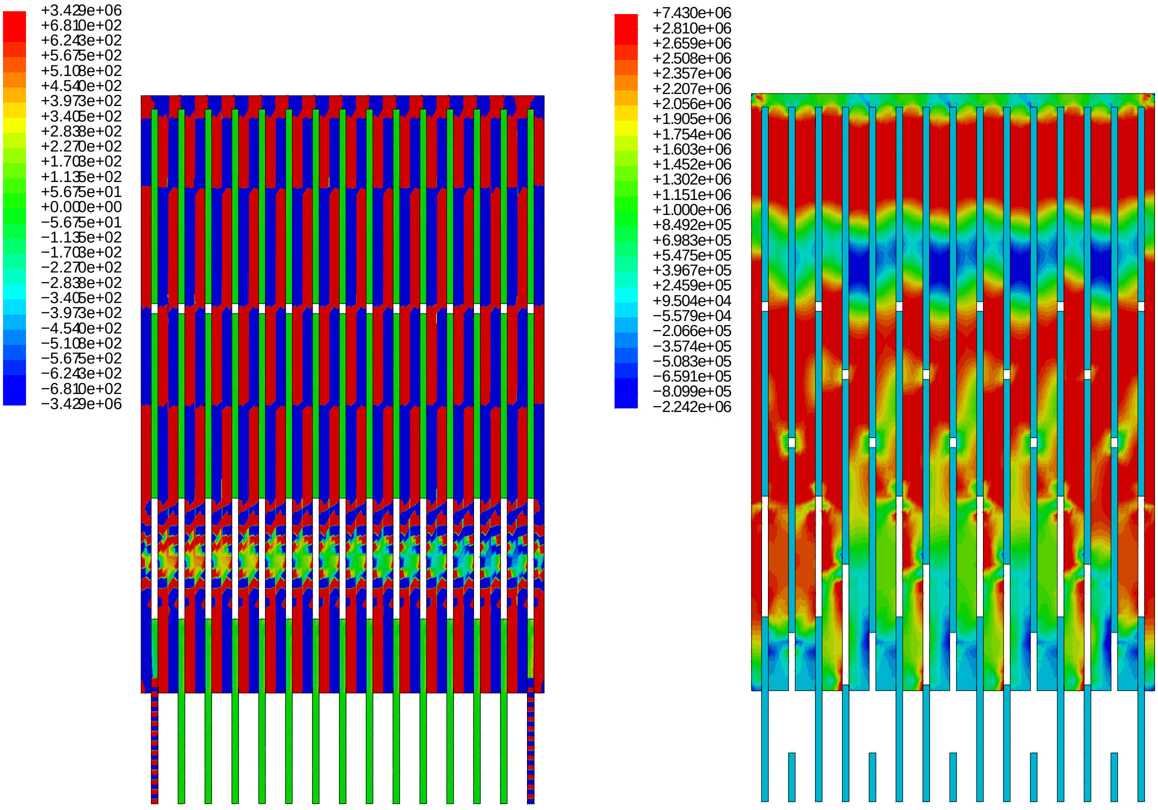

σ_{12} σ_{22}

Figure A.8: *Comparison of the stress fields of regular and random fiber distributions.*

BIBLIOGRAPHY

BIBLIOGRAPHY

Armero, F., and K. Garikipati (1996), An analysis of strong discontinuities in multiplicative finite strain plasticity and their relation with the numerical simulation of strain localization in solids, *International Journal of Solids and Structures*, *33*(20-22), 2863 – 2885, doi:DOI: 10.1016/0020-7683(95)00257-X.

Aveston, J., and A. Kelly (1973), Theory of multiple fracture of fibrous composites, *Journal of Materials Science*, *8*, 352–362.

Aveston, J., G. A. Cooper, and A. Kelly (1971), The properties of fibre composites, *Conference Proceedings, National Physical Laboratory (IPC Science and Technology Press Ltd)*.

Barber, J. R. (2010), *Elasticity*, Springer.

Barenblatt, G. (1962), The mathematical theory of equilibrium cracks in brittle fracture, *Advances in Applied Mechanics*, *7*, 55–129.

Bazant, Z. (1986), Mechanics of distributed cracking, *Applied Mechanics Reviews*, *39*, 675–705.

Bazant, Z., and L. Cedolin (2003), *Stability of Structures: Elastic, Inelastic, Fracture and Damage Theories*, Dover Publications.

Bazant, Z., and B. Oh (1983), Crack band theory for fracture of concrete, *Materials and Structures*, *16*, 155–177, 10.1007/BF02486267.

Camacho, G. T., and M. Ortiz (1996), Computational modeling of impact damage in brittle materials, *International Journal of Solids and Structures*, *33*, 2899–2938.

Cherepanov, G. P. (1967), The propagation of cracks in a continuous medium, *Journal of Applied Mathematics and Mechanics*, *31*, 503–512.

Cooper, G. A. (1970), The fracture toughness of composites reinforced with weakened fibres, *Journal of Materials Science*, *5*, 645–654.

Cox, B. N. (1991), Extrinsic factors in the mechanics of bridged cracks, *Acta metallurgica et materialia*, *39*, 1189–1201.

Crisfield, M. A., and J. Wills (1988), Solution strategies and softening materials, *Computer Methods in Applied Mechanics and Engineering*, *66*(3), 267 – 289, doi:DOI: 10.1016/0045-7825(88)90002-3.

Demmel, J. W., S. C. Eisenstat, J. R. Gilbert, X. S. Li, and J. W. H. Liu (1999), A supernodal approach to sparse partial pivoting, *SIAM J. Matrix Analysis and Applications*, *20*(3), 720–755.

Dolbow, J., N. Mos, and T. Belytschko (2001), An extended finite element method for modeling crack growth with frictional contact, *Computer Methods in Applied Mechanics and Engineering*, *190*(51-52), 6825 – 6846, doi:DOI: 10.1016/S0045-7825(01)00260-2.

Dugdale, D. S. (1960), Yielding of steel sheets containing slits, *Journal of the Mechanics and Physics of Solids*, *8*(2), 100 – 104, doi:DOI: 10.1016/0022-5096(60)90013-2.

Espinosa, H. D., P. D. Zavattieri, and S. K. Dwivedi (1998), A finite deformation continuum discrete model for the description of fragmentation and damage in brittle materials, *Journal of the Mechanics and Physics of Solids*, *46*(10), 1909 – 1942, doi:DOI: 10.1016/S0022-5096(98)00027-1.

Gao, Y.-C., Y.-W. Mai, and B. Cotterell (1988), Fracture of fiber-reinforced materials, *Zeitschrift fr Angewandte Mathematik und Physik (ZAMP)*, *39*, 550–572, 10.1007/BF00948962.

Garikipati, K. (1996), On strong discontinuities in inelastic solids and their numerical simulation, *Ph.D. Thesis, Stanford University.*

Garikipati, K. (2002), A variational multiscale method to embed micromechanical surface laws in the macromechanical continuum formulation, *Computer Modeling in Engineering and Sciences*, *3*(2), 175 – 184.

Garikipati, K., and T. J. R. Hughes (1998), A study of strain localization in a multiple scale framework–the one-dimensional problem, *Computer Methods in Applied Mechanics and Engineering*, *159*(3-4), 193 – 222, doi:DOI: 10.1016/S0045-7825(97)00271-5.

Garikipati, K., and T. J. R. Hughes (2000), A variational multiscale approach to strain localization - formulation for multidimensional problems, *Computer Methods in Applied Mechanics and Engineering*, *188*(1-3), 39 – 60, doi:DOI: 10.1016/S0045-7825(99)00156-5.

Griffith, A. A. (1921), The phenomena of rupture and flow in solids, *Philosophical Transactions of the Royal Society of London. Sereis A.*, *221*, 163–198.

Gustafson, P. A., and A. M. Waas (2009), The influence of adhesive constitutive parameters in cohesive zone finite element models of adhesively bonded joints, *International Journal of Solids and Structures*, *46*(10), 2201 – 2215, doi:DOI: 10.1016/j.ijsolstr.2008.11.016, special Issue in Honor of Professor Liviu Librescu.

Hertzberg, R. W. (1983), Deformation and fracture mechanics of engineering materials, *Wiley.*

Hill, R. (1950), *The Mathematical Theory of Plasticity*, Oxford University Press.

Hillerborg, A., M. Modeer, and P. E. Petersson (1976), Analysis of crack formation and crack growth in concrete by means of fracture mechanics and finite elements, *Cement and Concrete Research*, *6*, 773–782.

Hughes, T. J. R. (1995), Multiscale phenomena: Green's functions, the dirichlet-to-neumann formulation, subgrid scale models, bubbles and the origins of stabilized methods, *Computer Methods in Applied Mechanics and Engineering*, *127*(1-4), 387 – 401, doi:DOI: 10.1016/0045-7825(95)00844-9.

Hughes, T. J. R., G. R. Feijo, L. Mazzei, and J.-B. Quincy (1998), The variational multiscale method–a paradigm for computational mechanics, *Computer Methods in Applied Mechanics and Engineering*, *166*(1-2), 3 – 24, doi:DOI: 10.1016/S0045-7825(98)00079-6, advances in Stabilized Methods in Computational Mechanics.

Inglis, C. E. (1913), Stresses in a plate due to the presence of cracks and sharp comers., *Trans. Inst. Nav. Arch.*, *55*, 219–241.

Irwin, G. (1957), Analysis of stresses and strains near the end of a crack traversing a plate, *Journal of Applied Mechanics*, *24*, 361–364.

Jin, Z.-H., and C. Sun (2005), Cohesive zone modeling of interface fracture in elastic bi-materials, *Engineering Fracture Mechanics*, *72*(12), 1805 – 1817, doi:DOI: 10.1016/j.engfracmech.2004.09.011, international Conference of Heterogeous Material Mechanics, Chongqing University and Yangtze River/Three Gorges, China, June 21-26, 2004.

Kachanov, L. M. (1971), *Foundations of the Theory of Plasticity*, North Holland Publishing Co.

Kachanov, L. M. (1986), *Introduction to Continuum Damage Mechanics*, Springer.

Knowles, J. K., and E. Sternberg (1972), On a class of conservation laws in linearized and finite elastostatics, *Archive for Rational Mechanics and Analysis*, *44*, 187–211, 10.1007/BF00250778.

Kolosov, G. (1909), An application of the theory of functions of a complex variable to a planar problem in the mathematical theory of elasticity.

Krajcinovic, D. (1989), Damage mechanics, *Mechanics of Materials*, *8*(2-3), 117 – 197, doi:DOI: 10.1016/0167-6636(89)90011-2.

Larsson, R., K. Runesson, and N. S. Ottosen (1993), Discontinuous displacement approximation for capturing plastic localization, *International Journal for Numerical Methods in Engineering*, *36*, 20872105.

Li, S., M. Thouless, A. Waas, J. Schroeder, and P. Zavattieri (2005), Use of a cohesive-zone model to analyze the fracture of a fiber-reinforced polymer-matrix composite, *Composites Science and Technology*, *65*(3-4), 537 – 549, doi:DOI: 10.1016/j.compscitech.2004.08.004, jNC13-AMAC-Strasbourg.

Lubliner, J. (1990), *Plasticity Theory*, Macmillan Publishing Co.

Marsden, J. E., and T. J. R. Hughes (1994), *Mathematical Foundations of Elasticity*, Dover Publications.

Moes, N., and T. Belytschko (2002), Extended finite element method for cohesive crack growth, *Engineering Fracture Mechanics*, *69*(7), 813 – 833, doi:DOI: 10.1016/S0013-7944(01)00128-X.

Moes, N., J. Dolbow, and T. Belytschko (1999), A finite element method for crack growth without remeshing, *International Journal for Numerical Methods in Engineering*, *46*, 131 – 150.

Muskhelishvili, N. I. (1919), Sur l íntegration de l équation biharmonique, *Izv. Ross. Akad. Nauk.*, *13*, 663–686.

Needleman, A., and V. Tvergaard (1984), Finite element analysis of localization in plasticity, *Finite elements: Special problems in solid mechanics*, pp. 94–157.

Oliver, J., A. Huespe, and P. Snchez (2006), A comparative study on finite elements for capturing strong discontinuities: E-fem vs x-fem, *Computer Methods in Applied Mechanics and Engineering*, *195*(37-40), 4732 – 4752, doi:DOI: 10.1016/j.cma.2005.09.020, john H. Argyris Memorial Issue. Part I.

Pandolfi, A., P. Krysl, and M. Ortiz (1999), Finite element simulation of ring expansion and fragmentation: The capturing of length and time scales through cohesive models of fracture, *International Journal of Fracture*, *95*, 279–297, 10.1023/A:1018672922734.

Pietruszczak, S. T., and Z. Mroz (1981), Finite element analysis of deformation of strain softening materials, *International Journal for Numerical Methods in Engineering*, *17*, 327–334.

Raizer, Y. (1970), Physical principles of the theory of brittle fracture cracks, *Soviet Physics Uspekhi*, *13*.

Ramakrishnan, N., H. Okada, and S. N. Atluri (1994), On shear band formation: Ii. simulation using finite element method, *International Journal of Plasticity*, *10*(5), 521 – 534, doi:DOI: 10.1016/0749-6419(94)90012-4.

Rice, J. R. (1968), A path independent integral and the approximate analysis of strain concentration by notches and cracks, *Journal of Applied Mechanics*, *35*, 379–386.

Rudraraju, S. S., A. Salvi, K. Garikipati, and A. M. Waas (2010), In-plane fracture of laminated fiber reinforced composites with varying fracture resistance: Experimental observations and numerical crack propagation simulations, *International Journal of Solids and Structures*, *47*(7-8), 901 – 911, doi:DOI: 10.1016/j.ijsolstr.2009.12.006.

Salvi, A., A. M. Waas, and A. Caliskan (2008), Energy absorption and damage propagation in 2d triaxially braided carbon fiber composites: Effects of in situ matrix properties, *Journal of Materials Science*, *43*, 5168–5184.

Schellekens, J. C. J., and R. DeBorst (1993), On the numerical integration of interface elements, *International Journal for Numerical Methods in Engineering*, *36*, 43–66.

Simo, J. C., and T. J. R. Hughes (1998), *Computational Inelasticity*, Springer Verlag.

Simo, J. C., and J. Oliver (1994), A new approach to the analysis and simulation of strain softening in solids., *Fracture and Damage in Quasibrittle Structures.*

Simo, J. C., J. Oliver, and F. Armero (1993), An analysis of strong discontinuities induced by strain-softening in rate-independent inelastic solids, *Computational Mechanics*, *12*, 277–296, 10.1007/BF00372173.

Song, S., and A. Waas (1993), A nonlinear elastic foundation model for crack growth in laminates, *J. Composites Engineering*, *3*, 945–959.

Sun, C., and Z.-H. Jin (2006), Modeling of composite fracture using cohesive zone and bridging models, *Composites Science and Technology*, *66*(10), 1297 – 1302, doi:DOI: 10.1016/j.compscitech.2005.10.013.

Suquet, P. (1981), Sur les équations de la plasticité; existence et régularité des solutions, *Journal de Mecanique*, *20*, 3 – 39.

Temam, R., and G. Strang (1980), Functions of bounded deformation, *Archive for Rational Mechanics and Analysis*, *75*, 7–21, 10.1007/BF00284617.

Timoshenko, S. P. (1934), *Theory of Elasticity*, McGraw-Hill Book Company.

Truesdell, C. A., and W. Noll (1965), *The Non-Linear Field Theories of Mechanics*, vol. 3, Springer-Verlag.

Ungsuwarungsri, T., and W. G. Knauss (1987), The role of damage-softened material behavior in the fracture of composites and adhesives, *International Journal of Fracture*, *35*, 221–241.

Wells, G. N., and L. J. Sluys (2001), A new method for modelling cohesive cracks using finite elements, *International Journal for Numerical Methods in Engineering*, *50*, 2667 – 2682.

Williams, M. (1952), Stress singularities resulting from various boundary conditions in angular corners of plates under bending, *Journal of Applied Mechanics*, *19*, 526528.

Willis, J. R. (1967), A comparison of the fracture criteria of griffith and barenblatt, *Journal of the Mechanics and Physics of Solids*, *15*(3), 151 – 162, doi:DOI: 10.1016/0022-5096(67)90029-4.

Xie, D., and S. B. Biggers (2006a), Strain energy release rate calculation for a moving delamination front of arbitrary shape based on virtual crack closure technique, part ii: Sensitivity study on modeling details, *Engineering Fracture Mechanics*, *73*, 786–801.

Xie, D., and S. B. Biggers (2006b), Strain energy release rate calculation for a moving delamination front of arbitrary shape based on virtual crack closure technique, part i: Formulation and validation, *Engineering Fracture Mechanics*, *73*, 771–785.

Xie, D., and A. M. Waas (2006), Discrete cohesive zone model for mixed-mode fracture using finite element analysis, *Engineering Fracture Mechanics*, *73*, 1783–1796.

Xie, D., A. M. Waas, K. W. Shahwan, J. A. Schroeder, and R. G. Boeman (2004), Computation of energy release rates for kinking cracks based on virtual crack closure technique, *CMES-Computer Modeling in Engineering and Sciences*.

Xie, D., J. Chung, A. M. Waas, K. W. Shahwan, J. A.Schroeder, R. G. Boeman, V. Kunc, and L. B. Klett (2005), Failure analysis of adhesively bonded structures: from coupon level data to structure level predictions and verification, *International Journal of Fracture*, *134*, 231–250.

Xie, D., A. Salvi, C. Sun, A. M. Waas, and A. Caliskan (2006), Discrete cohesive zone model to simulate static fracture in 2-d triaxially braided carbon fiber composites, *Journal Composite Materials*, *40*, 1–22.

Xu, X. P., and A. Needleman (1994), Numerical simulation of fast crack growth in brittle solids, *Journal of the Mechanics and Physics of Solids*, *42*, 1397–1434.